CHAPTER 4

SATURATED HYDRAULIC CONDUCTIVITY BY MEANS OF PULSE TEST

4.1 INTRODUCTION

In the context of nuclear waste storage, saturated hydraulic conductivity becomes a fundamental parameter when analysing the long-term behaviour of a deep repository. Despite that, measurement of hydraulic conductivity is still far from being a routine for very low permeability materials and its measurement is not straightforward in such soils. Standard techniques become sometimes not suitable because of the long time required for the experiment or the difficulties when assessing the accuracy of the measurements. In addition, the validity of Darcy's law has been a controversial issue for these materials (Mitchell, 1993).

There are two approaches to estimate the hydraulic conductivity of clays: on one hand the direct approach, based on the analysis of a flow test, and on the other hand, the indirect estimation obtained from the interpretation of an oedometer test. A direct measurement is obviously preferred, but flow tests are difficult to handle for very low permeability soils. Additionally, flow tests may be performed under transient or steady state conditions. Typically they refer to falling head tests (transient) and constant head tests (steady). In both cases the amount of water involved is so small that very accurate devices are needed to measure the corresponding low flow rates. However, an alternative procedure based on the pulse test concept may be used. In this case, the decay of a pulse of water pressure applied to a boundary of the soil sample is measured. That decay is related to soil permeability and soil compressibility and that relation has been extensively used for the "in situ" characterisation of geological media.

A new mini-piezometer has been developed by UPC and built by AITEMIN (AITEMIN, 1999) to perform pulse tests in highly compacted clayey soils. Fourteen mini-piezometers were built; one of them was used to perform pulse tests and constant head tests in laboratory in a non-standard cell because of the maximum grain size of the mixture (up to 20 mm) where radial flow conditions applied. The other thirteen devices were placed at section A4 in the ZEDEX gallery as detailed in chapter 2. The use of pulse tests in geotechnical laboratories or practice is not common, and therefore the experimental procedure had to be defined. Some of the published cases regarding pulse tests refer to the measurement of permeability of rock samples (Brace et al. 1968; Hsieh et al. 1981; Neuzil et al. 1981; Zhang et al. 2000; Selvadurai et al. 2001; Hart & Wang, 2001). However, most of them refer to the 'in situ' application of water pressure pulses in the context of groundwater analysis of geological formations. In those cases, a section of a borehole between packers is pressurised during a short time interval, and the decay in water pressure may be related to the permeability and compressibility (or transmissivity and storage coefficient) of the surrounding formation. However, the original versions of these tests were performed directly in open boreholes or in open wells, applying a falling head boundary condition. In that case, the test was referred to as the 'slug test' in the groundwater literature, and consequently, pulse tests are considered as "pressurised slug tests". Both, slug and pulse test, may be performed as withdrawal tests, removing water from the soil or rock formation.

Mathematical solution of the pulse test problem in a borehole follows that of slug tests (Cooper et al. 1967). When hydraulic conductivity is very low, the response of a typical 'slug test' can be extremely long. To overcome this problem, Bredehoeft & Papadopoulos (1980) introduced in the previous formulation the "shut-in" effect considering a fast injection of water in the well and thus, they established the current version of the pulse test in closed wells or boreholes. Additional theoretical and practical studies of the application of pulse tests in the field and laboratory are given by Neuzil et al. (1981), Neuzil (1986), Carrera et al. (1989) and Chapuis (1998), among others. It must be pointed out that in the geotechnical literature the slug test / pulse test concept is frequently used in the context of piezometer data interpretation. Gibson (1963) presented a mathematical formulation, very similar to that of Cooper et al. (1967), but considering a spherical piezometer and focusing on time lag in pore water pressure measurements. Other related works, referring to the analysis of piezometer records, are due to Hvorslev (1951), de Jong (1953), Verruijt (1965), Premchitt & Brand (1981) and Brand & Premchitt (1982).

Despite the relatively large amount of applications, the use of pulse tests in the field exhibits many difficulties that remain to be solved, both on their execution and on their interpretation. This is because of the volume of water involved is usually low, and pressure variations are large and rapid. Therefore, the water injection and the measurements are sensitive to minor disturbances (Grisak et al. 1985 and Carrera et al. 1989), i.e.:

1. The borehole drilling process or piezometer introduction, surrounding formation may be significantly affected and altered, changing dramatically its properties (skin effect on hydrogeological literature or remoulded zone in geotechnical literature).
2. The borehole pressure evolution or the conditions prior to the tests.
3. Equipment compliance and correct determination of system flexibility. This parameter is very important to assess correctly hydraulic conductivity and storage capacity of a tight formation. Leakages in tubes, valves, etc., can strongly affect the correct determination of system flexibility.
4. Temperature effects during the test. Large variations of temperature can distort the observed results in a pulse test due to temperature gradients between soil water and injected water.

Nevertheless, the test may be more controlled under laboratory conditions, and because of that, it is used here as an additional procedure to estimate soil permeability. Therefore, an important part of this chapter is devoted to the analysis of the tests performed in a laboratory specimen. A previous calibration of the new device was performed in the laboratory in order to characterise this new equipment and develop techniques to study the pulse tests in laboratory. In this work, four pulse tests performed in laboratory were mathematically studied with an analytical model provided by Gibson (1963), with a semi analytical method provided by Brand & Premchitt (1982) and simulated by means of a finite element code with a Biot's extended theory. Differences attributed to geometry and assumptions of the three different approaches were investigated.

However, owing to its simplicity, pulse test was chosen to assess local backfill hydraulic conductivity in situ in the ZEDEX gallery at ÄHRL and some pulse tests were performed in the ZEDEX gallery by means of the layout AITEMIN designed and developed for this purpose (AITEMIN, 1999). The techniques and procedures were applied in the preliminary analysis of the first pulse tests performed in section A4 at the ZEDEX gallery at the beginning of 2003. After four years from the beginning of the saturation process, it was assumed that backfill is fully saturated, which is a reasonable hypothesis after the calculations carried out to predict the necessary time to saturate the backfill (chapter 5) and the measurements monitored in water pressure devices and psychrometers placed in the gallery (chapter 5).

4.2 LABORATORY TEST SCHEME AND GENERAL LAYOUT

The equipment used to perform the test in laboratory was:

- A mini-piezometer or "dynamic pore pressure sensor (DPPS).
- Two GDS pressure systems to measure water pressure and volume change.
- A high-speed valve to get the shut-in effect in the system when it closes suddenly.
- A PC controls the test and acquires the data.
- A cylindrical cell made of stainless steel, where soil is compacted and the DPPS placed.

A side view of the mini-piezometer is shown in figure 4.1. It consists of a small cylinder containing two tubes and a pore pressure transducer within the body. The metallic parts inside the mini-piezometer and the input and output tubes are made of stainless steel to avoid corrosion in saline watery environment. The range of water pressure measured by the piezorresisitive transducer (KULITE Semiconductor) varies from 0 to 5.88 MPa, the pore diameter of the ceramic filter is 60 μm and its hydraulic conductivity is $3 \cdot 10^{-4}$ m/s. The total length of DPPS is 180 mm, the porous stone is 100 mm in length and the DPPS diameter is 50 mm. The DPPS was built by AITEMIN (AITEMIN, 1999). Figure 4.2 shows the calibration of the pressure transducer within the DPPS used in laboratory performed with a GDS pressure system and the cell filled with de-aired water.

Figure 4.3 shows the scheme of the test used in the laboratory, and figure 4.4 shows a side view of the designed cell. Figure 4.5 shows a picture with all the components of this flow test. Equipment and components used in the test were placed into a controlled-temperature room (22±1ºC). Daily variation of temperature affected significantly the cell, tubes and water pressure systems, introducing volume changes in the system and cell. Cell thermal deformations disturbed the results of constant head tests due to their long duration (chapter 4, section 4.4). In order to check this effect out, a specimen of sand was compacted in the cell and water pressure was increased up to 900 kPa after saturation. All the valves in the cell were closed and the evolution of water pressure evolution in the DPPS was monitored. Figure 4.6 shows the daily variation of water pressure monitored in the cell. The period of the water pressure variation was one day and the maximum amplitude registered was of 35 kPa. A small leakage was also observed during this period as water pressure within the cell decreased. It was assumed this leakage did not affect the pulse tests or the constant head tests. Regarding pulse tests, thermal influences have been disregarded due to its short length (less than hour). Nevertheless, while performing constant head tests, though the cell was thermally isolated, influence of daily temperature variations on measured outgoing water volume was significant due to the cell change of volume. To minimise the observed thermal deformations, the cell and pressure systems were thermally isolated after the results of six constant head flow tests as detailed in section 4.4.

Backfill was compacted dynamically with the DPPS within. Figure 4.7 shows the soil specimen compacted into the cell. Once the soil was compacted and the cell closed, backfill saturation phase started. Pulse test are performed when backfill is fully saturated (initial backfill water pressure is p_0). After saturation, water pressure in the injecting pressure system is increased up to $p_1 = p_0 + \Delta p$ (the high-speed valve is closed). At that moment, the high-speed valve opens, controlled by the PC, until measured water pressure within the piezometer is equal to p_1. When water pressure in the piezometer is equal to p_1, the high-speed valve closes again and it remains closed during the dissipation process. The sudden close of the high-speed valve introduces the influence of water compressibility on the system flexibility. The evolution of water pressure is monitored and recorded.

At the piezometer-backfill contact the flow boundary condition is controlled by a balance of mass of water. In the outer part of the cell two different flow boundary conditions can be imposed:

1. Water pressure fixed at the external boundary and equal to initial backfill water pressure (p_0). A permeable geotextile is present in the outer boundary of the cell between the soil and the cell.
2. A no-flow boundary condition can be prescribed in the outer part of the cell by closing all the drainage valves.

Important differences in water pressure dissipation were observed when different boundary conditions were applied during the pulse tests. The dissipation process of a pulse test when water pressure is prescribed in the outer boundary is slower than the dissipation process of a no-flow prescribed boundary condition at the outer part of the cell. The reason is the different amount of water involved in both tests as water compressibility mainly controls the flow of water in the no-flow prescribed boundary condition pulse test. All pulse tests performed in this thesis were injection pulse tests. As injection of water is as an unloading-reloading process in terms of effective stresses, elastic backfill behaviour is expected. The three theoretic approaches explained below are valid for withdrawal tests when elastic soil response is assumed.

Cell compressibility was assessed by filling the cell and system with de-aired water and increasing water pressure within the cell. Volume of water required to increase the water pressure within the cell was measured and corrected subtracting water compressibility, tubes and pressure system deformability. Variation of measured volumetric deformation of the cell vs water pressure within the cell is shown in figure 4.8. The measured relationship is highly non-linear below 600 kPa due mainly to screws deformation, O-ring deformation, etc. From figure 4.8, cell volume change (ΔV_{cell}) was known when water pressure varied from 700 kPa to 800 kPa (Δp). ΔV_{cell} was 2.6 cm^3 after correcting water compressibility ($C_w = 4.5\cdot 10^{-4}$ MPa^{-1}). Cell total volume, V_{cell}, was 15404 cm^3. Then, cell compressibility, C_{cell}, can be estimated assuming linear elastic behaviour as

$$C_{cell} = \frac{\frac{\Delta V_{cell}}{V_{cell}}}{\Delta p} = \frac{\frac{2.6}{15404}}{0.1\,MPa} = 1.69{\cdot}10^{-3}\ MPa^{-1} \rightarrow K_{cell} = 592\,MPa \qquad (1)$$

This value mainly depends on cell geometry and mechanical properties of stainless steel, screws and O-rings. By assuming linear behaviour of steel, a relationship (2) between the cell compressibility and the equivalent stainless steel bulk modulus was calculated by means of a finite element code, solving the mechanical problem when the cell is pressurised. For these calculations, CODE_BRIGHT (Olivella et al. 1996) was used. This code was developed to solve thermo-hydro-mechanical problems in geological media in a fully coupled way, but only the mechanical equations were solved to study the cell deformation. Figure 4.9 shows the linear relationship obtained between the steel bulk modulus and the computed bulk modulus of the cell from the calculations. With the so-computed correlation, the equivalent value of stainless steel bulk modulus, K_{steel}^{eq}, was obtained for the simulation of the pulse tests. The Poisson coefficient of stainless steel, ν, was always 0.3.

$$K_{steel}^{eq} = \frac{K_{cell}}{\dfrac{K_{cell}^{computed}}{K_{steel}}} = \frac{K_{cell}}{0.0779} = 7596\ MPa \tag{2}$$

From equation (2) and a Poisson's coefficient of 0.3, an equivalent bulk modulus and equivalent shear modulus of steel were calculated: K_{steel}^{eq} = 7596 MPa and G_{steel}^{eq} = 3506 MPa. These values were set as steel elastic parameters in the simulation of the pulse tests in order to correctly account for the observed deformation of the cell.

4.3 SPECIMEN PREPARATION

Backfill was dynamically compacted into the stainless steel cell. The height of the test specimen was 304 mm and 127 mm in radius. A geotextile membrane was placed in the outer contour of the cell. Backfill was compacted in twelve layers and the energy applied was 357 kJ/m^3 (≈ 63% normal Proctor). The estimated volume of the cell filled with backfill was 14846 cm^3 and the mass of backfill was 27220 grams at average initial water content of 12%. During the compaction process of the layers, the backfill was sealed by means of a plastic bag to prevent water evaporation. The average initial backfill water content was 12.0% and after the compaction process, dry specific weight was 16.0 kN/m^3 and void ratio 0.643. When backfill compaction process was performed, a metallic cast with the same shape and size as the DPPS was used. The cast allowed compacting the backfill within the cell without ramming the DPPS. After ten layers of soil had been compacted, the cast was retired and the DPPS was placed into the hole very carefully in order to avoid disturbing it. The extraction process of the metallic cast and the introduction of the DPPS did not apparently create a remoulding zone in the surroundings.

After the DPPS had been placed within the cell, the compaction process continued and two more backfill layers were compacted. The soil specimen was saturated with de-ionised water (< 20 μS/cm). Water pressure in the soil specimen at the ending of the saturation process was 700 kPa for two main reasons: cell compressibility, valves and tubes became nearly linear beyond 600 kPa (figure 4.8), and water pressure was high enough to dissolve air bubbles that might be present in the soil pores.

4.4 CONSTANT HEAD TESTS RESULTS

Before performing the pulse tests, some constant head tests were carried out in the cell to obtain an independent measurement of backfill hydraulic conductivity. Constant head test followed a similar procedure as the pulse test: backfill water pressure was prescribed at the outer part of the cell, p_0, and water pressure was prescribed with another pressure system at the mini-piezometer, p_1. The applied average gradient was calculated as $\frac{p_1 - p_0}{\gamma_w \Delta r}$, where Δr is the distance between the porous filter of the mini-piezometer and the geotextile (10.2 cm). Figure 4.10 shows a scheme of the constant head test performed in the cell.

In order to compute the hydraulic conductivity the intake factor of the cell should be calculated. Due to radial symmetry of the problem, small size of the cell and applied boundary conditions, the intake factor experiments important changes if compared with obtained ones with usual expressions in infinite medium (Brand & Premchitt, 1980 or Ratnam et al. 2001). Therefore, the intake factor was calculated using CODE_BRIGHT. For this geometry and boundary conditions, the calculated intake factor was F = 0.667 m. The hydraulic conductivity was calculated as

$$Q_{st} = F \cdot k \cdot \Delta H \tag{3}$$

where Q_{st} is the steady state flow rate [L^3/T], calculated from steady conditions of incoming volume-time curves, F is the intake factor of the mini-piezometer, cell and boundary conditions [L], k is the hydraulic conductivity [L/T], and ΔH is the change of piezometric head that produces the water movement [L].

Six constant flow tests were performed to estimate the hydraulic conductivity and to check out the validity of Darcy's law. Table 4.1 shows the calculated hydraulic conductivities by using equation (3) from the six flow tests. In all constant head tests, water pressure p_0 (outer part of the cell) was 700 kPa and water pressure in the mini-piezometer p_1 was increased depending on the applied gradient. Figure 4.11 shows the variation of hydraulic conductivity with the applied gradient in each test. The average value of backfill permeability is $6.5 \cdot 10^{-12}$ m/s ($\pm\ 0.624 \cdot 10^{-12}$ m/s). The results clearly showed the validity of Darcy's law for water flow in this range of hydraulic gradient (4-100).

Dixon et al. (1999) validated the Darcy's law in low permeability media as well. They varied the gradient from 1 to 100 on illitic clay and bentonite-sand mixtures with two different kinds of permeant (fresh water and saline water). Range of investigated hydraulic conductivity was from $1 \cdot 10^{-13}$ to $1 \cdot 10^{-9}$ m/s. Another work concluding the validity of Darcy's law was made by Tavenas et al. (1983) for a soft and undisturbed clay in a "leak-free" triaxial cell with constant head test varying the gradient from 0.1 to 50.

Gradient	p_0 *(kPa)*	p_1 *(kPa)*	Q_{st} *(cm³/h)*	r^2	k *(m/s)*
4	700	704	0.0061	0.9920	$\mathbf{6.2 \cdot 10^{-12}}$
8	“	708	0.0125	0.9976	$\mathbf{6.4 \cdot 10^{-12}}$
16	“	716	0.0253	0.9965	$\mathbf{6.4 \cdot 10^{-12}}$
25	“	725	0.0349	0.9990	$\mathbf{5.6 \cdot 10^{-12}}$
50	“	750	0.0892	0.9986	$\mathbf{6.7 \cdot 10^{-12}}$
100	“	800	0.1800	0.9987	$\mathbf{7.5 \cdot 10^{-12}}$

Table 4.1: Results from six constant head tests performed in the cell at different hydraulic gradients.

Figures 4.12 to 4.17 show the incoming and outgoing measured water volumes for gradients 4, 8, 16, 25, 50 and 100 respectively. The outgoing water volume is strongly affected by external effects such as cell deformations related to temperature variations within the controlled-temperature room. This temperature influence on the results was more important when hydraulic gradient was small. However, even for higher gradients, both curves (ingoing and outgoing volume of water) were not parallel. At steady state conditions, both curves should have similar slopes, which means similar flow rates of water. This is an unexpected result, mainly attributed to local effects on the external part of the cell due to the daily variations of temperature and therefore, as cell deformed, backfill specimen also deformed. After these results, the cell and the water reservoirs were isolated with low thermal conductivity foam in order to decrease the influence of thermal variations on the flow tests.

After isolating the cell and the water pressure systems, a long constant flow test was performed in the cell to check the thermal effects on the outgoing volume of water. Initial applied hydraulic gradient was 50 and after a few days it was increased up to 100. The results are shown in figure 4.18. Evolution of injected water pressure, temperature, difference of water pressure between both water pressure systems and incoming and collected water were monitored for more than 200 days. From the test, it could be firstly concluded that backfill was fully saturated. Table 4.2 summarises the most important parameters involved in this flow test. From the evolution of incoming volume of water, the flow rate of water at steady state conditions was calculated and used to compute the hydraulic conductivity. From 0 to 18 days, the incoming water pressure was 750 kPa and the water pressure prescribed at the outer boundary condition was 700 kPa. After 18 days, the incoming water pressure was increased up to 800 kPa, which doubled the hydraulic gradient and the flow of rate. No changes of hydraulic conductivity were calculated as it is shown in figure 4.19.

Time (days)	p_0 *(kPa)*	p_1 *(kPa)*	*Gradient*	ΔH (m)	Q_{st} *(cm^3/h)*	*F (m)*	*k (m/s)*
0 - 18	700	750	50	5.02	0.075	0.667	$\mathbf{6.3 \cdot 10^{-12}}$
18 - 133	"	800	100	10.04	0.149	"	$\mathbf{6.2 \cdot 10^{-12}}$

Table 4.2: Results from the constant head test performed when the cell had been thermally isolated.

A zoom of the first 30 days is shown in figure 4.20. It is clear that after isolating the cell the outgoing volume of water improved its evolution and both curves (incoming and outgoing volume) were parallel. Therefore, it was checked in this way that the six flow tests were reliable since backfill specimen was saturated and the change of volume of the cell, produced by the variation of temperature, was responsible of the unexpected behaviour of the outgoing volume of water. The applicability of Darcy's law for backfill was assessed again with this new constant head test.

4.5 PULSE TESTS RESULTS

A comparison of the four pulse tests is depicted in figure 4.21. Ordinate axis in this figure represents a dimensionless normalisation of the pressure evolution by using

$$\varepsilon = \frac{p_t - p_{final}}{p_m - p_{final}} \tag{4}$$

where p_t is the water pressure at time t, p_{final} is the final water pressure registered in the test (for a prescribed pressure pulse test $p_{final} = p_0$, and for a no-flow boundary condition pulse test p_{final} depends on the injected water volume, water compressibility, soil storage capacity an soil volume. p_m is the maximum water pressure after the injection. Defined in that way ε varies from 0 to 1. This normalisation allows comparing the effect of changing the flow boundary condition on the observed response. Table 4.3 summarises the general data of the four pulses. In all the tests carried out in laboratory, the increase of water pressure within the DPPS was nearly 100 kPa. One of the most relevant aspects is the different amount of water involved in every test. Injected water in pulse 1 or 2 (no-flow boundary condition) was around 30 mm^3. However, injected water in pulse 3 or 4 (prescribed pressure boundary condition) was closed to three times more. System flexibility, f_{obs}, was calculated with the modification introduced by Neuzil (1982) as volume of water injected to reach a desired water pressure increase.

$$f_{obs} = \frac{\Delta V}{\Delta p} \tag{5}$$

The different amount of water and time to reach the desired water pressure in the pulse tests, depending on which boundary condition was applied at the extern part of the cell, were due to the relative small volume of the soil specimen. From a theoretical point of view, there is a soil volume, big enough, at which changing the hydraulic boundary condition (impervious or prescribed water pressure) does not significantly affect the observed dissipation in a pulse test. In our case, the volume of the cell is not big enough and the response in those tests is sensitive to changes of the boundary condition at the outer part of the cell. When water pressure at the outer part of the cell is prescribed, water flows because some water drains from the cell to the pressure system during the injection time and then, influence of water compressibility is not very significant on the dissipation process. When a no-flow boundary condition is prescribed, the necessary amount of water and time to increase the pressure inside the mini-piezometer are smaller, because of closed volume of the cell. In this case, the response is mainly controlled by the volume of stored water within the soil skeleton and its compressibility.

Pulse	p_0 (kPa)	p_m (kPa)	Δp (kPa)	ΔV (cm^3)	f_{obs} (m^3/MPa)	t_0 (s)	Boundary condition
1	761	852.4	91.4	0.031	$0.363 \cdot 10^{-6}$	2.25	No flow
2	713	829.9	116.9	0.035	$0.299 \cdot 10^{-6}$	2.01	No flow
3	703	803.9	100.9	0.102	$1.010 \cdot 10^{-6}$	4.57	p_0 = 703 kPa
4	709	802.4	93.4	0.090	$0.963 \cdot 10^{-6}$	3.25	p_0 = 709 kPa

Table 4.3: General data of the pulse tests carried out. t_0 is the time the pressure system required to increase the water pressure inside the DPPS (or the injection time).

4.6 SIMULATION OF PULSE TESTS

Pulse tests were simulated using three different procedures in order to compare them, and to find out which one was the best to analyse a pulse test in laboratory and in situ. The first one was the analytical solutions provided by Gibson (1963). His solutions were implemented in an optimisation procedure to back-analyse the measured dissipation processes. The second one was a semi-analytical method provided by Brand & Premchitt (1982). This semi-analytical model was compared with the Gibson's model. The main difference of this model compared to Gibson's model is the symmetry. Gibson solved the Terzaghi's equation in spherical symmetry and Brand & Premchitt numerically solved the Terzaghi's equation but in axisymmetric cylindrical coordinates (both in infinite medium conditions). The third one was to simulate the measured pulse tests by means of a finite element code to solve the coupled hydro-mechanical problem in a more general manner.

4.6.1 Gibson's model

Gibson (1963) provided an analytical solution for the consolidation problem in spherical symmetry, infinite medium and assuming an isotropic, homogeneous and linear elastic soil. Figure 4.22 shows the geometry solved by Gibson. The model has two parameters: *C* (the soil consolidation coefficient) and μ (a dimensionless stiffness) and the equations of this problem are

$$C\left\{\frac{\partial^2 p}{\partial r^2}+\frac{2}{r}\frac{\partial p}{\partial r}\right\}=\frac{\partial p}{\partial t} \tag{6.1}$$

$$p(r,0)=p_0 \quad (r>a,\forall t) \tag{6.2}$$

$$p(\infty,t)=p_0 \quad (\forall t) \tag{6.3}$$

$$p(a,t)=\gamma_w h(t) \quad (\forall t>0) \tag{6.4}$$

$$4\pi a^2\frac{k}{\gamma_w}\left(\frac{\partial p}{\partial r}\right)_{r=a}=A\frac{dh}{dt} \tag{6.5}$$

Where *p(r,t)* is the pore water pressure (and not the excess of water pressure), *a* the equivalent radius of the end of the standpipe, *A* is the cross sectional area of the standpipe, *h(t)* the height of water column inside of the piezometer, γ_w is the water specific weight, *C* is the soil consolidation coefficient, p_0 the initial formation pore pressure, and *k* the soil permeability. A dimensionless stiffness, μ, of the measuring system was defined as

$$\mu=\frac{4\pi a^3\gamma_w m}{A}=\frac{F^3\gamma_w m}{16\pi^2 A} \tag{7}$$

where *m* is the soil compressibility and *F* is the intake factor of a spherical tip (F = 4πa). The theory developed by Gibson was modified to take correctly into account the effect of water compressibility. The consolidation coefficient and the dimensionless stiffness were changed by introducing this factor (Verruijt, 1984).

$$C^*=\frac{k}{m^*\gamma_w}=\frac{k}{\gamma_w}\left(\frac{3K_{soil}+4G_{soil}}{3+nC_w\left(3K_{soil}+4G_{soil}\right)}\right) \tag{8}$$

Where m^* is the modified soil compressibility, which takes into account water compressibility, C_w. K_{soil} and G_{soil} are the bulk and shear modulus, and *n* is the soil porosity. The boundary condition in the piezometer is controlled by the continuity of mass of water between the standpipe or system and the soil. In the same way as Bredehoeft & Papadopulos (1980) modified the slug test, the boundary condition in the standpipe was slightly adapted by introducing the amount of water, ΔV, flowing into the soil in a time increment, Δt.

$$4\pi a^2\frac{k}{\gamma_w}\left(\frac{\partial p}{\partial r}\right)_{r=a}=A\frac{dh}{dt}=\lim_{\Delta t\to 0}\frac{\Delta V}{\Delta t}=f_{obs}\lim_{\Delta t\to 0}\frac{\Delta p}{\Delta t}=f_{obs}\gamma_w\frac{dh}{dt} \tag{9}$$

Then, by replacing *A* by $f_{obs}\gamma_w$ in equation (7), the dimensionless stiffness was modified and expressed as

$$\mu^* = \frac{F^3 m^*}{16\pi^2 f_{obs}} \tag{10}$$

It is important to point out the strong influence of the intake factor on the dimensionless stiffness due to its cubic exponent. Therefore, variations of the intake factor can produce important variations in the dimensionless stiffness. Correct determination of this factor becomes a key issue when analysing the pulse tests.

The factors influencing the dissipation process in a variable flow test are the system flexibility, the hydraulic conductivity and the soil compressibility. Gibson's model depends on two parameters, C^* and μ^*, which depend on the three previously indicated parameters. Figures 4.23 and 4.24 show the solutions provided by Gibson depending on the dimensionless time $T = \frac{C^* t}{a^2}$. Looking carefully at figure 4.24 it is clear that the curves are so close among them that large error can be made when analysing flow tests if the system flexibility is small or the soil compressibility is high (high values of the dimensionless stiffness).

Pulse tests performed with prescribed water pressure at the outer part of the cell were simulated with the Gibson's model. The results of these very first calculations demonstrated the usefulness of the procedure to estimate the hydraulic conductivity (Mata & Ledesma, 2001). After that, the no-flow boundary condition pulse tests were also simulated. Nevertheless, as expected, the results provided by Gibson's model were not reliable when analysing the no-flow boundary condition pulse tests. This is because of the boundary conditions of the model were too different from the boundary conditions in the test performed in laboratory.

4.6.1.1 Maximum likelihood estimation technique

Interest in solving the parameter estimation problem in an automatic manner has notably grown in all science branches in last years. Some interesting works dealing with geotechnical or hydrogeology application of this procedure are Carrera & Neuman (1986) or Ledesma et al. (1996) among others. The majority of them use statistics to estimate parameters of a mathematical model from laboratory or field test information. One of the most known techniques is the maximum likelihood approach. The measurements, $\mathbf{x}^*$, are considered as random variables. Moreover, a mathematical model, **M**, is necessary to relate the calculated values, **x**, to the parameters, **p**. The model can be linear or non-linear depending on the problem. The best estimation of parameters is given by the maximum of the likelihood function, defined as the combined probability of the errors of the measurement of the state variables, which control the problem, and the previous information of the parameters available. It is generally assumed that error of the measurements of the state variables and error of the parameters are independent. Under these hypothesis the maximum likelihood can be calculated as

$$L = \xi \, P(\Delta\mathbf{x}, \Delta\mathbf{p}) = \xi \, P(\Delta\mathbf{x})P(\Delta\mathbf{p}) \tag{11}$$

where ξ is a constant and $P(\Delta\mathbf{x}, \Delta\mathbf{p})$ is the joint probability function of the error of the measurements. The approach considers the model is correct, and no errors coming from the model are taken into account with this technique. When previous information is not available, as in our case, equation (11) can be expressed as

$$\mathrm{L} = \xi\ \mathrm{P}(\Delta\mathbf{x}) \tag{12}$$

Generally, a Gaussian distribution is assumed for the measurement errors. Maximising equation (11) is equivalent to minimise another function, *J*, defined as

$$\mathrm{J} = -2\ln(\mathrm{L}) = -2\xi\ln(\mathrm{P}(\Delta\mathbf{x})) = -2\xi\ln\left\{\left(\sqrt{(2\pi)^m\left|\boldsymbol{C}_{\mathrm{x}}\right|}\right)^{-1}\exp\left\{-\frac{1}{2}\left(\boldsymbol{x}^*-\boldsymbol{x}\right)^t\boldsymbol{C}_{\mathrm{x}}^{-1}\left(\boldsymbol{x}^*-\boldsymbol{x}\right)\right\}\right\} \tag{13}$$

where *m* is the number of measurements, $\boldsymbol{C}_x^{-1}$ is the covariance matrix of the measurements and $\left|\boldsymbol{C}_x\right|$ is its determinant. After some algebra and introducing the relationship between the calculated values and the parameters, **M(p)**, a simpler expression of function J can be obtained as

$$\mathrm{J} = (\mathbf{x}^* - \mathbf{M}(\mathbf{p}))^{\mathrm{t}}C_x^{-1}(\mathbf{x}^* - \mathbf{M}(\mathbf{p})) + \ln\left|\boldsymbol{C}_{\mathrm{x}}\right| + \mathrm{m}\ln(2\pi) - 2\ln(\xi) \tag{14}$$

J is generally called the objective function. The three last terms of expression (14) can be neglected because they are constant. In order to minimise (14), it is necessary to know the covariance matrix of the measurements. It is complicated to estimate this matrix because it depends on the error structure of the problem: the test, the equipment, the operator who obtained the data, etc. In this case, operator, procedure and equipment were the same for all the measurements, in that case, this matrix is an identity matrix divided by an unknown standard deviation error, σ_x^2.

$$J(\boldsymbol{p}) = \frac{1}{\sigma_x^2}\left(\boldsymbol{x}^* - \boldsymbol{M}(\boldsymbol{p})\right)^t\left(\boldsymbol{x}^* - \boldsymbol{M}(\boldsymbol{p})\right) \tag{15}$$

Analysing expression (15) it arises that it is the same expression obtained when the least squares method is applied. Therefore, maximum likelihood approach is equivalent to this method when there is not previous information, a normal distribution of the error of the measurements is assumed and all the measurements are independent and have the same error. In that way, the minimum of J provides an estimation of the parameters assuming the model **M** is correct.

4.6.1.2 Optimisation procedure

There is a large number of minimisation algorithms available. One of these methods is the gradient method, in which information on the derivative of the function to be minimised is required. Its main advantage is the efficiency, and its main disadvantage is the computational effort and its sensitivity to the initial approximation used. A modification implemented by Levenberg-Marquardt (Marquardt, 1963) of the Gauss-Newton method has been used in this thesis. Starting from an initial set of parameters, the increment vector of them to approach the minimum of J is

$$\boldsymbol{\Delta p} = \left\{\boldsymbol{A}^{\mathrm{t}}\boldsymbol{C}_{\mathrm{x}}^{-1}\boldsymbol{A} + \lambda\boldsymbol{I}\right\}^{-1}\boldsymbol{A}\boldsymbol{C}_{\mathrm{x}}^{-1}\left(\boldsymbol{x}^* - \boldsymbol{x}\right) \tag{16}$$

where λ is the Marquardt parameter and $\boldsymbol{A} = \left.\frac{\partial\boldsymbol{M}(\boldsymbol{p})}{\partial\boldsymbol{p}}\right|_{\boldsymbol{p}_0}$ is the sensitivity matrix. This matrix has been calculated by a central finite differences scheme, which has a second order error.

The Gibson's model has an analytical solution therefore, the sensitivity matrix could be calculated in an exact form. Nevertheless, the numerical approximation offered good results. As the algorithm reaches the objective function minimum, Marquardt's parameter goes to zero.

4.6.1.3 Reliability of identified parameters

The *a posteriori* covariance matrix of the parameters, $\mathbf{C}_\mathrm{p}$, can be calculated to find out, in a qualitative way, if the estimated parameters are a good approach to the real solution. To calculate this matrix, it is assumed that the problem becomes linear close to the minimum.

$$\boldsymbol{C}_p = \left\{\boldsymbol{A}^t \boldsymbol{C}_x^{-1} \boldsymbol{A}\right\}^{-1} = \sigma_x^2 \left\{\boldsymbol{A}^t \boldsymbol{A}\right\}^{-1} \tag{17}$$

This expression provides a lower limit of the variances of the estimated parameters (Ledesma et al. 1996). To estimate the variances of the measurements it is used the value of the objective function at the minimum $J_{\min}$ (Wiggins, 1972).

$$\sigma_x = \sqrt{\frac{J_{\min}}{m-n}} \tag{18}$$

Where *m* is the number of measurements and *n* is the number of parameters (two in this case, C^* and μ^*). For numerical reasons, the logarithm of the consolidation coefficient was estimated, which notably improved the convergence of the optimisation method.

Figure 4.25 shows an objective function and the trajectory followed by the parameters during the optimisation procedure for a synthetic pulse test generated with the Gibson model ($C^* = 1.10^{-8}$ m^2/s and $\mu^* = 50$). Figure 4.26 shows a zoom of the area close to the minimum. It can be observed that a narrow valley appears, which really makes difficult the estimation of parameters with such an objective function because a big number of families of parameters that fit the real solution and provide similar errors. A problem arises when soil is highly compressible or system is very rigid ($\mu^* > 4$) because the dissipation process depends mainly on the product km^*.

4.6.1.4 Analysis of the results

Table 4.4 shows the results of the simulations of the four pulse tests performed in laboratory. C^* and μ^* were back calculated for each test by means of the maximum likelihood approach previously described.

Figures 4.27 and 4.28 show the contour maps of the objective functions of pulse tests number 3 and 4 calculated by means of Gibson's model. One of the most interesting aspects was the low value of m^* obtained simulating the pulse tests with a no-flow boundary condition (pulse tests 1 and 2). The model predicts a stiffer soil due to the smaller amount of water used and the fast dissipation process. The results provided for these boundary conditions are not very good, since the model should not be used in this case as it was previously commented. However, simulation of the pulse tests with the water pressure prescribed (pulses 3 and 4) by means of Gibson's model provided good results of permeability. The Gibson's model is able to explain the dissipation process in this kind of test. Looking at expression (10) the importance of the intake factor can be noted. The results can change in a spectacular way if this parameter slightly changes. This is, probably, the weakest point of this formulation when it is used for non-spherical piezometers.

Pulse	p_0 (kPa)	p_1 (kPa)	ΔV (cm^3)	f_{obs} (m^3/MPa)	C^*_{min} (m^2/s)	μ^*_{min}	k (m/s)	m^* (MPa^{-1})
1	761	852.4	0.031	$0.363 \cdot 10^{-6}$	$1.4 \cdot 10^{-05}$	3.60	$\mathbf{3.3 \cdot 10^{-10}}$	0.002
2	713	829.9	0.035	$0.299 \cdot 10^{-6}$	$2.0 \cdot 10^{-05}$	3.20	$\mathbf{3.4 \cdot 10^{-10}}$	0.002
3	703	803.9	0.102	$1.010 \cdot 10^{-6}$	$2.1 \cdot 10^{-08}$	75.8	$\mathbf{8.3 \cdot 10^{-12}}$	0.041
4	709	802.4	0.090	$0.963 \cdot 10^{-6}$	$1.0 \cdot 10^{-08}$	109.6	$\mathbf{5.5 \cdot 10^{-12}}$	0.056

Table 4.4: Results obtained after back-analysing the pulse tests by means of Gibson's model.

4.6.2 Brand & Premchitt model

Brand & Premchitt (1982) solved the problem suggested by Gibson in axisymmetric cylindrical coordinates via the finite difference method. With the numerical approximation of the problem, they built an equalisation chart depending on the main parameters of the problem (piezometer geometry, soil compressibility, system flexibility and hydraulic conductivity) and the t_{50} and t_{90} times of the equalisation process. With the equalisation chart, the assumption of an equivalent radius of a cylindrical piezometer used when applying the Gibson's theory was finally avoided. Varying the length/diameter ratio of the piezometer, they found a unique relationship between t_{90}/t_{50} and the dimensionless stiffness λ or the control parameter:

$$\lambda = \frac{4\pi bka^2}{Cf_{obs}\gamma_w} = \frac{4\pi bma^2}{f_{obs}} \tag{19}$$

where *b* is half of the porous length of the piezometer and *a* is the radius of the cylindrical piezometer. By knowing t_{50} and t_{90}, the coordinates at the chart for each test can be estimated $\left(\frac{C}{a^2}, \frac{4\pi bk}{f_{obs}\gamma_w}\right)$. From these two values, hydraulic conductivity and soil compressibility are determined. With this work, it was verified the important errors that could be committed when equalisation processes in cylindrical piezometers were studied as spherical. Forty-five variable head flow tests on clay samples with different piezometers and manometers were analysed in that work. Hydraulic conductivities estimated with the cylindrical equalization chart were 2 or 2.5 times bigger than those calculated with the spherical chart (Premchitt & Brand, 1981). Consolidation coefficients calculated for both methods were also very different (calculated ones by using the spherical chart were 5 times bigger than calculated ones using the cylindrical chart).

The four pulses were also simulated with this semi analytical model. Hydraulic conductivity and soil compressibility assessed with the cylindrical chart are in good agreement with data coming from the constant head tests. Differences between spherical model and cylindrical equalisation chart are not outstanding in these cases. Table 4.5 shows backfill hydraulic conductivity and compressibility for the four pulses performed. Similar trends were observed in the results obtained by using the semi-analytical model when compared with the results obtained with the Gibson's model. However, it can be observed that backfill compressibility estimated by means of cylindrical equalization chart are bigger than estimated ones by means of spherical model. The main consequence that can be drawn after this analysis is that the finite size of the soil sample is very important in the estimation of hydraulic conductivity and soil compressibility, and additionally, the effect of the piezometer geometry may become important.

Pulse	t_{50} (s)	t_{90} (s)	C/a^2 (s^{-1})	$\frac{4\pi bk}{f_{obs}\gamma_w}$ (s^{-1})	λ	k (m/s)	m^* (MPa^{-1})
1	3	120	$1 \cdot 10^{-3}$	$1 \cdot 10^{-2}$	10	$5.7 \cdot 10^{-11}$	0.009
2	3	56	$2 \cdot 10^{-3}$	$2 \cdot 10^{-2}$	10	$9.3 \cdot 10^{-11}$	0.007
3	13	800	$4 \cdot 10^{-5}$	$1 \cdot 10^{-3}$	25	$1.6 \cdot 10^{-11}$	0.065
4	12	800	$2 \cdot 10^{-5}$	$1 \cdot 10^{-3}$	50	$1.5 \cdot 10^{-11}$	0.122

Table 4.5: Results obtained when pulse tests were analysed by means of the cylindrical equalisation chart.

4.6.3 Numerical simulation by using CODE_BRIGHT

The four pulse tests performed in laboratory were also simulated via the finite element method with CODE_BRIGHT (Olivella et al. 1996) in a coupled hydro-mechanical analysis. Previously to the simulation of the four pulse tests, the code was verified by solving a consolidation problem in saturated media with analytical solution. In our case, stresses follow the continuum mechanics criteria (compression is negative). In the finite element formulation, a selective integration was used by means of the modification of the matrix **B** (relating strains to displacements) to avoid locking when the medium is highly incompressible (Hughes, 1980).

4.6.3.1 Validation of CODE_BRIGHT

Consolidation of a finite sphere loaded with a constant load $\Delta\sigma$ with a free draining surface was simulated. Cryer (1963) solved this problem by using the Biot's theory and compared the solution with the Terzaghi-Rendulic solution. When Biot's theory is applied, the so-called Mandel-Cryer effect appears in this problem. This effect produces an unexpected increase of the excess of water pressure, Δp, at the centre of the sphere before it decreases. Cryer did not provide with any explanation for this behaviour because his aim was to compare the results from different formulations (Terzaghi versus Biot). Depending on Poisson's coefficient, the increase of the water pressure excess can be very important (the highest occurs when $\nu = 0$). If $\nu = 0.5$ the solution obtained by the Terzaghi-Rendulic theory is recovered.

Gibson et al. (1963) provided an explanation based on the variation of Poisson's ratio during the consolidation process. Schiffman et al. (1969) studied the consolidation of a strip load of uniform load intensity acting on the surface of a frictionless semi-infinite solid with a free draining surface by means of Biot's theory and they observed the Mandel-Cryer effect in their solution. They said that water increase was due to a partial transfer of total stress to the soil. At a short time after loading, changes on effective stress will have been produced at the free draining surface, but no significant changes on effective stress will have been produced "far" from the draining surface, so water pressure increases to keep the effective stress law. Mandel-Cryer has been experimentally observed in similar tests by (Gibson et al. 1963; Verruijt, 1965; Hart & Wang, 2001).

A numerical solution of that consolidation problem was performed in a finite sphere of one meter in radius. Soil hydraulic conductivity was $6.5\cdot10^{-12}$ m/s, Poisson's coefficient was ν = 0.0 and 0.33 and Young's modulus was 3000 MPa. Load increment at the surface of the sphere was -0.5 MPa, initial water pressure was 0.5 MPa and initial stresses were $\sigma_r = \sigma_\theta = \sigma_\phi$ = -1 MPa. The evolution of the ratio between water pressure excess at the centre of the sphere and load increment applied to the sphere, $\left(\frac{\Delta p(0,t)}{\Delta\sigma}\right)$, calculated by the finite element code and its comparison with the analytical solution is shown in figure 4.29. Dissipation depends on the dimensionless time, $T = \frac{C^*t}{a^2}$, where a is the radius of the sphere and C^* is the consolidation coefficient (calculated by using equation 8). The agreement between the analytical solution and the numerical one is good.

Gibson's problem was also simulated by means of CODE_BRIGHT, but results were not satisfactory at initial times. This was due to variation of total stress during the water injection. When total stress reached its maximum variation, results between Gibson's analytical solution and the predicted numerical result became comparable, however, while total stress changed differences appeared between both predicted water pressure dissipation curves. Note that Gibson's theory is based on Terzaghi's theory, which assumes constant total stresses. The comparison between the calculated dissipation process by means of CODE_BRIGHT and Gibson's model is shown in figure 4.30. The geometry used to solve this second consolidation problem was a sphere of 10 metres in radius including a small spherical piezometer of 0.15 meters in radius.

The hydro-mechanical properties of the material used to simulate the spherical piezometer were very permeable and very stiff (rigid contact). Water compressibility was reduced up to $1\cdot10^{-4}$ MPa^{-1} to diminish its effect on the numerical solution and soil properties were Young's modulus of 3000 MPa, Poisson's ratio of 0.3 and hydraulic conductivity of $6.5\cdot10^{-12}$ m/s. The water injection period lasted 2 seconds and $1\cdot10^{-6}$ m^3 of water were injected. During the injection, water pressure in the spherical piezometer increased 206 kPa. With these conditions the Gibson's analytical solution can be determined as a function of parameters computed using equations (8) and (10). The consolidation coefficient of the problem was $2.278\cdot10^{-6}$ m^2/s and the system dimensionless stiffness was 2.508.

It can be seen how both dissipation processes at the centre of the medium were different between them until the moment that the variation of total mean stress reached a maximum value of 8 kPa. After this maximum was reached, both dissipation processes predicted the same behaviour. Mechanical boundary condition was changed at the outer surface of the soil sphere to check out its influence: at first, no-displacement was set in the boundary condition and the results were compared when constant stress was set in the boundary. No differences in the dissipation of the excess of water pressure were observed after changing the mechanical boundary condition and consequently, it was concluded that 10 meters was big enough to simulate an infinite medium in these conditions.

4.6.3.2 Coupled hydro-mechanical analysis of the pulse tests

Initial and boundary conditions

Brand & Premchitt (1982) wrote a standard flow boundary condition between soil and piezometer in two dimensions (r, z) as

$$2\pi a\frac{k}{\gamma_w}\int_{-b}^{b}\frac{\partial p}{\partial r}dz = f_{obs}\left.\frac{\partial p}{\partial t}\right|_{r=a} \tag{20}$$

where *2b* is the total length of the ceramic filter of the piezometer. A fictitious rigid material was set to simulate this flow boundary condition. Properties of this material were always the same: hydraulic conductivity and Young's modulus very high if compared with backfill properties. The aim of this material is to store water during the injection as the water cavity of the piezometer does. Figure 4.31 summarises initial, flow and mechanical boundary conditions for both kind of pulse tests performed depending on flow boundary condition at the outer part of the cell. Initial conditions were similar in all four pulse tests. Gravity was also considered in the simulation of the pulse tests.

Material properties

An isotropic, homogeneous and linear elastic model was used to simulate the behaviour of all materials. To assume isotropic and homogeneous behaviour was supported by different results found in the literature. Even strongly compacted MX-80 bentonites (up to 50 or 100 MPa of compacting pressure) did not show any marked tendency of particles to be oriented after the compacting pressure was applied (Push, 1982).

The tests carried out were injection tests so the expected behaviour should be elastic because injecting water is an unloading-reloading process. Initial backfill void ratio was in all cases 0.643. The fictitious material void ratio was variable depending on the water volume injected, backfill properties and flow boundary condition prescribed in the outer part of the cell. Poisson's ratio of the fictitious material and backfill was 0.3.

Table 4.6 summarises the backfill hydro-mechanical properties for each pulse test simulated. These results were obtained by means of a trial and error procedure. The equivalent steel bulk and shear modulus were $K_{steel}^{eq} = 7596\,MPa$ and $G_{steel}^{eq} = 3506\,MPa$ as indicated previously. The fictitious material is even more rigid than the steel so the displacements in the contact between the backfill and the fictitious material are negligible (rigid piezometer). Water compressibility was $4.5\cdot10^{-4}$ MPa^{-1} in all four pulse tests.

Pulse	*k* (m/s)	K (MPa)	G (MPa)	m* (MPa^{-1})	C* (m^2/s)	μ*
1	8.10^{-12}	2.29	2.50	0.178	$4.57\cdot10^{-09}$	921.45
2	8.10^{-12}	2.50	2.72	0.163	$4.99\cdot10^{-09}$	1024.41
3	9.10^{-12}	2.08	2.27	0.196	$4.67\cdot10^{-09}$	364.66
4	8.10^{-12}	1.67	1.82	0.245	$3.32\cdot10^{-09}$	478.07

Table 4.6: Constitutive parameters used in the pulse test simulations by means of CODE_BRIGHT.

Results

Finite element simulations of the four pulse tests are depicted in figures 4.32 to 4.35. These simulations show the tests were properly reproduced with this formulation assuming backfill linear elastic behaviour. Hydraulic conductivities calculated with the finite element code are slightly higher than those measured in the constant head tests. This can be explained due to different amount of water involved at both tests. While constant head tests involved several cubic centimetres of water (depending on the hydraulic gradient), pulse tests involved less than 0.1 cm^3. This means that pulse test is more sensitive to small leakages than constant head test because they are difficult to calibrate. Moreover, some amount of water is used to pressurise a part of the system, which is not involved in the test because the water stored after the increase of water pressure remains pressurised (i.e. the system before the electric or high-speed valve). This means that, for example, if the real amount of water involved in a pulse test is 90% of the measured amount of water, the “real” hydraulic conductivity will be lower than the estimated one by using the measured amount of water. This can be qualitatively explained by using Gibson’s model. Figure 4.36 shows the dissipation curves for two different values of the dimensionless stiffness (μ_1 and μ_2) when μ_2 is bigger than μ_1. In this situation, the measured amount of water, ΔV_m, and the soil compressibility (assumed constant and known) provides a value of the dimensionless stiffness μ_1. However, the real amount of water, ΔV_r, used to pressurise the system from the high-speed valve to the DPPS is smaller, the real dimensionless stiffness is μ_2, higher than μ_1.

$$\Delta V_m > \Delta V_r \rightarrow f_1 > f_2\big|_{m^*=\text{constant}} \rightarrow \left\{ \begin{array}{l} f_1 = \dfrac{\Delta V_m}{\Delta p} \rightarrow \mu_1 = \dfrac{F^3 m^*}{16\pi^2 f_1} \\ f_2 = \dfrac{\Delta V_r}{\Delta p} \rightarrow \mu_2 = \dfrac{F^3 m^*}{16\pi^2 f_2} \end{array} \right\} \rightarrow \mu_1 < \mu_2 \tag{21}$$

Therefore, it is possible to prove that the dimensionless time T_2 is lower than T_1 if, for instance, the value of the 50% of the dissipation process is analysed:

$$\mu_2 T_2 < \mu_1 T_1 \rightarrow \frac{\mu_2 T_2}{\mu_2} < \frac{\mu_1 T_1}{\mu_2} \rightarrow T_2 < \frac{\mu_1 T_1}{\mu_2} < T_1\big|_{\mu_2 > \mu_1} \tag{22}$$

Finally, it can be checked that the “real” hydraulic conductivity is lower than the estimated one when using the measured amount of water.

$$\left. \begin{array}{l} T_1 = \dfrac{C_1^* t_{50}}{a^2} \rightarrow k_1 = \dfrac{T_1 a^2 m^* \gamma_w}{t_{50}} = \alpha T_1 \\ T_2 = \dfrac{C_2^* t_{50}}{a^2} \rightarrow k_2 = \dfrac{T_2 a^2 m^* \gamma_w}{t_{50}} = \alpha T_2 \end{array} \right\} \rightarrow k_2 < k_1\big|_{T_1 > T_2} \tag{23}$$

Back-analysed compressibility from the two pulse tests where a no-flow boundary condition was prescribed, was slightly slower than the values obtained with the prescribed water pressure at the outer part of the cell. The estimated compressibility is in good agreement with measured Young’s modulus in Black Hills bentonite – crushed granite mixture by Radhakrishna & Chan (1982) after saturation at similar dry specific weights but with slightly higher bentonite content (50/50 by weight). From the one dimensional consolidation theory, backfill oedometric compressibility can be estimated as

$$m = \frac{0.434 \cdot C_s}{\sigma' \left(1 + e_0\right)} \tag{24}$$

where C_s is the swelling index, estimated from the oedometer tests as 0.03 at a dry specific weight of 15.9 kN/m^3. The effective stress within the cell is equal to the backfill swelling pressure corresponding at a void ratio of 0.643 (global backfill void ratio within the cell). Backfill swelling pressure at this dry specific weight has not been measured but it can range from 50 to 120 kPa. By doing so, the backfill compressibility ranges from 0.07 to 0.19 MPa^{-1}, which is in good agreement with estimated backfill compressibility from the pulse tests.

Observed differences between the shape of the measured pulse test and those calculated by means of the Gibson's model are due to the different geometry of the problem (spherical versus radial). The biggest difference observed in the previous comparisons is the estimation of backfill compressibility. Calculated ones with the finite element method (an extended Biot's formulation) are around four times higher than the back-calculated ones by means of Gibson's model (Terzaghi's consolidation theory). Some reasons can explain the differences observed comparing the results from the Gibson's model and the numerical simulation with an extended Biot's formulation. Gibson solved the instantaneous injection at $t = 0^+$ but with the FE code the injection can be easily studied and simulated. Gibson's model was formulated for infinite medium and we have checked that is not true in the case of the cell. Moreover, the use of an equivalent radius for the cylindrical mini-piezometer can introduce important errors in the estimation of compressibility (Brand and Premchitt, 1982). Finally, the equalisation process in the cell is three-dimensional (two-dimensional with a symmetry axis assuming isotropy of the medium) and the Gibson's model is one-dimensional.

Figures 4.37 and 4.38 show soil porosity evolution and total mean stress evolution for pulse test number 3. This means that correct determination of backfill compressibility is more difficult as small changes in the compressibility do not affect the results of the simulations. Total stresses change slightly, which means that the Terzaghi's approach for this problem is reasonable especially if long time dissipation is considered.

In order to compare all the hydraulic information available in specimens hydrated with distilled water, it is convenient to present hydraulic conductivity values as a function of specific dry weight, as in figure 4.39. Some additional data provided by Clay Technology (Börgesson et al. 1996; Johannesson et al. 1999) are also depicted in this figure. The results confirmed that the logarithmic relationship between permeability and dry specific weight corresponding to the fitting of backfill permeability evolution at the oedometer test performed at dry specific weight of 16.6 kN/m^3 and distilled water (expression 18, chapter 3) can be used to estimate hydraulic conductivity for specific weights between 15.9 kN/m^3 and 19 kN/m^3. In this way, it can be concluded that backfill hydraulic conductivity was measured by three different methods and the results were in good agreement among them.

4.7 LABORATORY TEST DISMANTLING

Two specimens have been prepared in this cell. The first one was prepared in mid 1998 and dismantled in mid 1999. The second one was prepared in early 2000 and it has not been dismantled yet. Figure 4.40 shows the mini-piezometer within the first soil specimen during the cell dismantling process. Backfill was extruded by means of a hydraulic press and small samples of backfill were carefully retired and their water content measured. Water content was higher in the surroundings of the piezometer. All the information presented here came from the second specimen prepared in early 2000. Data coming from the first backfill specimen compacted in the cell has not been shown because there was a preferential flow path which distorted the hydraulic tests. Estimated hydraulic conductivity and measured flow rate of the first specimen were much higher than the second one. No preferential flow paths were observed in the second specimen prepared.

4.8 PULSE TESTS IN THE ZEDEX GALLERY

Thirteen mini-piezometers were placed at section A4 by AITEMIN in 1999 (AITEMIN, 1999). Location and orientation of the mini-piezometers are shown in figure 2.20 (chapter 2). Saturation process of the gallery started in mid 1999. As it was commented before, water used to saturate the backfill in situ contains 16 g/L in order to increase backfill hydraulic conductivity and therefore, to speed up the saturation process. Water used in the pulse tests comes from the surrounding aquifer and it contains 12 g/L in average. As the amount of water involved in the test is small, it is not assumed any variation of hydraulic conductivity due to different salt concentration.

Since the installation of the sensors, six devices seem to be broken down (late March 2003). Devices DPP1, DPP2, DPP4, DPP6, DPP12 are not working and neither response nor output were obtained. DPP13 is not working properly as it presented unpredictable behaviour. Sensors placed at inner parts of the layers of section A4 were subjected to higher compaction efforts as, for instance, DPP2, DPP4 or DPP12. The higher compacting effort appears to be the most likely reason to justify why they broke down.

It was decided to perform some pulse tests even before full backfill saturation might have been reached in order to set a procedure and to check the usefulness of the layout. Nevertheless, it is believed that full backfill saturation has been reached as positive water pressure was measured in all the devices. Eighteen injecting pulse tests were performed and one constant flow test as well. A preliminary study of some of the pulse tests was carried out in order to determine the local backfill hydraulic conductivity in different areas of the layers at section A4. A complete in situ pulse test campaign will be completed throughout 2003 and 2004. After the future campaign of pulse tests, a map of local backfill hydraulic conductivity will be obtained and compared with global backfill hydraulic conductivity estimated from global flow tests to be carried out throughout 2003 and 2004 as well.

4.8.1 *Brief description of the system layout*

The acquisition and control system is divided into two parts: one of them was placed at a control room built and managed by Clay Technology AB where it is protected from accidents, weathering and water from fractures. Figure 4.41 shows a simplified scheme of the whole layout built and placed by AITEMIN for the Backfill and Plug Test Project. Figure 4.42 shows the acquisition and control system, which is made up by a N_2 tank, a PC and a complex valve panel where pressure transducers and a flow meter are placed. Outside the control room, due to its size, it is placed the other part of the layout. This second part of the system is made up by the interphase between water and N_2, the vacuum pump and some deposits, which allow changing the system flexibility depending on the expected hydraulic conductivity. This second part of the control system is shown in figure 4.43. There are three tanks to modify the flexibility of the system (auxiliary tanks) and a big one to refill the interphase. Stainless steel AISI 316L was used for building the metallic parts of the control and acquisition system.

However, after almost four years, corrosion appeared at the part placed outside the control room.

From the interphase a metallic tube goes to the switching panel placed at the DEMO tunnel, and from the switching panel, thirteen inflow tubes go to each one of the mini-piezometers, and thirteen outflow tubes from the mini-piezometers reach a glass tank within the control room through the switching panel. The system is closed, and, in this way, it is possible to circulate water and remove trapped air from the mini-piezometers (AITEMIN, 1999). Pulse tests have to be performed in series because of the acquisition software and hardware. There are around 100 meters of metallic tube from the acquisition and control system to the mini-piezometers. Nevertheless, the first 50 meters are not directly involved in the system flexibility. System flexibility is made up of the tube from the switching panel to the DPPS and the DPPS itself.

4.8.2 *Positioning of the mini-piezometers*

Three mini-piezometers were placed at layer 2, seven at layer 3 and three more at layer 4. Three different orientations were conceived to install the mini-piezometers: perpendicular to the layer, parallel to the layer and horizontal (parallel to the axis of the tunnel). Figure 2.20 (chapter 2) shows the final arrangement of the thirteen DPPS and their orientation. Piezometers were differently oriented in order to study local hydraulic conductivity in different directions. During the installation of the DPPS, AITEMIN used a dummy to avoid damaging the DPPS. Figure 4.44 shows the process of installation of DPPS in parallel and perpendicular direction to the layer. Figures 4.45 and 4.46 show two DPPS after the installation process in one of the layers. Table 2.1 (chapter 2) shows the final coordinates of the sensors installed by AITEMIN.

Disturbing effects as skin effects, preferential flow paths, etc., around sensors and tubes, could appear, but backfill swelling capacity should be enough to erase these effects in those areas where backfill was well compacted. Areas close to the roof and ground of the tunnel were less compacted as it was shown in chapter 2 and as a result, backfill swelling capacity could become almost negligible. Thus, it is expected higher backfill hydraulic conductivity and higher backfill compressibility in the areas where smaller backfill dry specific weight was obtained after the backfill compaction.

4.8.3 *In situ pulse test*

Prior to the tests, some water was flowed into all the piezometers and air might have been trapped was removed. Moreover, an independent measurement of relative water pressure within the mini-piezometers was done in all of them. The results showed that, apparently, backfill saturation has been already reached. Full backfill saturation was expected by late 2002 or beginning of 2003. Measured water pressure within the mini-piezometers is shown in figures 4.47, 4.48 and 4.49. The maps of relative water pressure show clearly that areas close to the wall of the gallery are fully saturated and measured water pressure is similar to water pressure applied in the mats. Only water pressure measured in DPP11 (190 kPa, layer 4) is far away from the values registered in DPP1 (380 kPa, layer 2) or DPP5 (450 kPa, layer 3). DPPS placed at the inner parts of the layers show smaller values of the monitored water pressure (DPP2, DPP4, DPP7, DPP9 or DPP12) but these values, as direct measurement by the DPPS was not available, were measured in an external pressure transducer. These low values are mainly attributed to non-steady state condition when the measurement was taken. As water had to flow from the backfill, the process was slow and equilibrium was not reached in those sensors where backfill hydraulic conductivity was smaller. It is also possible that while the saturation process continued, water pressure was increasing in the backfill as water was injected in the mats and steady conditions might have not been reached yet. It was also observed that a recalibration of the pressure transducers within the DPPS was necessary after measuring the water pressure in an external pressure transducer placed in the acquisition and control system. A difference (up to 40 kPa) was observed in some piezometers close to the roof and ground when comparing the external water pressure measurement and the measurement provided by the pressure transducer within the DPPS.

Pulse tests were performed in devices DPP3, DPP5, DPP7, DPP8, DPP9, DPP10, DPP11 and DPP13. The two constant head tests were performed in DPP8 and DPP11. An increase of water pressure (750 kPa) was applied in the interphase and transmitted to the switching panel in the pulse tests performed. Then, when the mini-piezometer has been selected, the valve connecting the pressurised system to the DPPS opens during some seconds (t_0) and then closes. Depending on the permeability of the surrounding backfill, longer time is necessary to increase water pressure within the DPPS. An important difference arises between the pulse tests performed in laboratory and the pulse tests performed in situ: in the laboratory, the increase of water pressure was prescribed, therefore, water was injected until water pressure within the DPPS was p_m (= $p_0 + \Delta p$). However, p_m cannot be prescribed in situ. Some water is injected during t_0 and thus, water pressure within the DPPS increases. The increase of water pressure is measured a posteriori, and depends on system flexibility (tube and DPPS deformation), water head losses within the system, and backfill compressibility and hydraulic conductivity.

The flow meter measures the mass of water and the maximum flow rate it can measure is 65 kg/h (18 g/s). The total amount of water used in each test was measured with a maximum precision of 1 ml. Water pressure evolution of devices where pulse tests were performed is shown in figures 4.50 to 4.57 (from 03 – 25 – 2003 to 04 – 02 –2003). As response of DPP13 was lost after two hours from the beginning of the pulse test a zoom it is depicted in figure 4.58. The injection time, t_0, was 20 seconds, and it is clear that during this injection time, water pressure was more or less constant, decreasing when valve was closed. It is important to note that dissipation of excess of water pressure after the tests in areas close to the roof or the ground are faster than those performed in inner parts of the section. The minimum variation of water pressure detected by the piezorresistive transducers is 5 kPa due to its accuracy and above all, to its high range of measurement (0 – 5.88 MPa). Therefore, in those devices where the increase of water pressure was small (DPP8 or DPP10), the dissipation process is “stairs” shaped, which makes it difficult to analyse.

As it was previously mentioned, it is important to find out the amount of water that does not flow into the backfill but it is included in the measurement. The amount of water would produce an overestimation of hydraulic conductivity. Thus, flexibility of 5 meters of tube made of stainless steel, which it has been used in the entire layout built by AITEMIN, and water contained within the tube, was experimentally determined. Figure 4.59 shows the variation of volume measured with water pressure. The tube selected for this purpose is very stiff, the thickness is 0.7 mm, the external diameter is 3.21 mm and the inner diameter is 1.81 mm. Flexibility of 50 metres of tube was estimated as $1.416 \cdot 10^{-3}$ ml/kPa if linear elastic behaviour of the tube is assumed. As it is shown in figure 4.41, the distance between the switching panel and the pressure system in the control office is around 50 meters. Therefore, it is possible to estimate the amount of water used to pressurise this part of the system, which is not directly involved in the test as (25). Table 4.7 summarises the data of the pulse tests.

$$\Delta V_r\,(ml) = \Delta V_m\,(ml) - \Delta p\,(kPa) \times 1.416 \cdot 10^{-3}\ {}^{ml}\!/_{kPa} \tag{25}$$

Sensor	p_0 (kPa)	p_m (kPa)	Δp (kPa)	ΔV_m (ml)	ΔV_r (ml)	f_{obs} (m^3/MPa)	t_0 (s)
DPP3	552.0	635.7	83.7	4	3.88	$4.633 \cdot 10^{-5}$	20.2
DPP5	500.0	557.9	57.9	5	4.90	$8.463 \cdot 10^{-5}$	20.0
DPP7	403.0	650.0	257.0	4	3.47	$1.355 \cdot 10^{-5}$	20.1
DPP8	538.8	563.1	24.3	5	4.96	$1.976 \cdot 10^{-4}$	20.1
DPP9	352.4	695.3	342.9	6	5.51	$1.606 \cdot 10^{-5}$	20.3
DPP10	541.4	577.9	36.4	3	2.94	$8.085 \cdot 10^{-5}$	20.0

Table 4.7: General data of the pulse tests carried out in section A4. t_0 is the time that the valve, which connects the system and the mini-piezometer, was open (the injection time). p_0 and p_m are the initial and maximum relative water pressure during the pulse tests.

4.8.4 *Numerical analysis of the pulse tests*

In order to analyse the pulse tests, the Gibson's model was used and the finite element code as well. At first, Gibson's model is used to obtain an initial estimation of backfill hydraulic conductivity and compressibility. Objective functions were calculated and the minimum of each one was determined. After the estimation of parameters by using Gibson's model, the finite element code was used with similar parameters. Parameters were modified in a trial error procedure to fit the dissipation processes. It is clear that if pulse tests carried out close to the rock are analysed by means of Gibson's model, important variations of parameters and large errors will be committed. However, Gibson's model should be valid for those pulse tests performed in sensors placed in the central part of section A4 (DPP7 and DPP9).

Two different geometries were considered at this preliminary stage. Both geometries were two-dimensional with an axis of cylindrical symmetry. Gravity was not taken into account and consequently, a quasi three-dimensional analysis could be done. However, the real geometry of each sensor is three-dimensional as most of them are placed very close to the host rock. Figure 4.60 shows the geometry considered to analyse pulse tests were boundary effects of host rock are thought to be negligible. Figure 4.61 shows the geometry when it is considered that the host rock can affect the boundary conditions of the dissipation process. The boundary conditions are the same in both cases. Nevertheless, it is difficult to know the real boundary conditions in those sensors close to the host rock. Another important difficulty arises when estimating backfill porosity around each sensor. In the inner part of section A4 it is assumed that dry specific weight is 16.6 kN/m^3 (porosity, n = 0.368, or void ratio, e = 0.582). Nevertheless, close to the roof or ground, porosity is much lower. From figure 2.13 (chapter 2), it is observed the variation of dry specific weight after compaction in those areas. Backfill dry specific weight in this area was 13.7 kN/m^3 (n = 0.480, e = 0.921).

Specific weight of water was 0.0098 MPa/m. Mini-piezometer intake factor has been the same in all the situations. This hypothesis is not true for devices close to the host rock as real boundary conditions close to the rock and three-dimensional geometry strongly influence this geometric factor. The intake factor, *F*, of the minipiezometer was calculated by using the expression proposed in infinite media by Ratnam et al. (2001) where *b* is the length of the ceramic porous stone and *a* is the radius of the piezometer (b/a = 2). Further details of the selection of this intake factor are given in the appendix.

$$\frac{F}{a}=1.1872\frac{b}{a}+2.415\sqrt{\frac{b}{a}}+3.1146\rightarrow F=0.4451\,\mathrm{m} \tag{26}$$

- DPP3

Figure 4.62 shows the position of this sensor in layer 2 at section A4. It is close to the rock and measured initial water pressure is 552 kPa. Initial water pressure is a little bit higher than the expected one, probably due to the calibration factor relating the electric signal and water pressure. At first, the contour map of the objective function was calculated and the minimum of the function was obtained. The contour plot of the objective function is depicted in figure 4.63. The minimum of this function was $\mu^* = 5.1$ and $C^* = 1.58 \cdot 10^{-8}$ m^2/s. From these values and by using the system flexibility, $4.633 \cdot 10^{-5}$ m^3/MPa, estimated backfill hydraulic conductivity was $6.5 \cdot 10^{-11}$ m/s and backfill compressibility was 0.42 MPa^{-1}. These parameters were used in the finite element simulation, but higher hydraulic conductivity and lower backfill compressibility were necessary to properly fit the measured dissipation process: $k = 1 \cdot 10^{-10}$ m/s and $m^* = 0.150$ MPa^{-1}. Both curves are similar, but they are unable to reproduce the beginning of the dissipation process. Comparison among the measured values and both calculations is shown in figure 4.64. Backfill porosity was 0.48.

- DPP5

Figure 4.65 shows the position of this sensor at the third layer of section A4. It is close to the rock and measured initial water pressure is 501 kPa. The contour map of the objective function was calculated and the minimum of the function was obtained. The contour plot of the objective function is depicted in figure 4.66. The minimum of this function was $\mu^* = 16.1$ and $C^* = 1.58 \cdot 10^{-9}$ m^2/s. From these values and by using the system flexibility $8.583 \cdot 10^{-5}$ m^3/MPa, estimated backfill hydraulic conductivity was $3.8 \cdot 10^{-11}$ m/s and backfill compressibility was 2.47 MPa^{-1}. Estimated backfill compressibility is large and it is not expected such a big value. When analysing the pulse tests by means of the finite element simulator, the parameters obtained to fit the results were: $k = 1 \cdot 10^{-10}$ m/s and $m^* = 0.372$ MPa^{-1}. Both curves are similar, but they are unable to reproduce the beginning of the dissipation process. Comparison among the measured values and both calculations is shown in figure 4.67. Backfill porosity was 0.48, corresponding to a dry specific weight of 13.7 kN/m^3.

- DPP7

Figure 4.68 shows the position of this sensor in layer 3 at section A4. It is far away from the rock and measured initial water pressure is 405 kPa. The contour map of the objective function is depicted in figure 4.69 and the minimum of this function was $\mu^* = 2.1$ and $C^* = 3.02 \cdot 10^{-8}$ m^2/s. From these values and by using the system flexibility, $1.355 \cdot 10^{-5}$ m^3/MPa, estimated backfill hydraulic conductivity was $1.5 \cdot 10^{-11}$ m/s and backfill compressibility was 0.05 MPa^{-1}. When analysing the pulse tests by means of the finite element simulator, the parameters obtained were: $k = 1.5 \cdot 10^{-10}$ m/s and $m^* = 0.052$ MPa^{-1}. Both curves are very similar and they fit very well the dissipation process. Comparison among the measured values and both calculations is shown in figure 4.70. As the parameters are almost the same and both curves as well, it is concluded that in these conditions, both results are almost equivalent. Backfill porosity was 0.36, corresponding to a dry specific weight of 16.6 kN/m^3.

- DPP8

Figure 4.71 shows the location and arrangement of sensor DPP8. It is close to the lateral wall of the tunnel and measured initial water pressure is 538 kPa. Gibson model was not applied to this pulse test because of its proximity to the rock. Therefore, only the approach by means of the finite element code was used. The system flexibility is $2.04 \cdot 10^{-4}$ m^3/MPa (the highest estimated one). This high system flexibility is related to the higher backfill permeability and compressibility in this area. Figure 4.72 shows the comparison between the measurements and the calculated dissipation process by the finite element code. The parameters used in the simulation were $k = 3 \cdot 10^{-9}$ m/s and $m^* = 1.486$ MPa^{-1}. Backfill porosity was 0.48.

- DPP9

As backfill hydraulic conductivity around sensor DPP9 is expected to be low, influence of prior tests or the water pressure history is important when simulating pulse tests. Figure 4.68 shows the position of this sensor in layer 3 of section A4. It is also far away from the rock and measured initial water pressure is 315 kPa. In this case, the two pulse tests performed in this sensor will be simulated in order to account for the non-steady conditions when performing the second pulse test. The contour map of the objective function second pulse test is depicted in figure 4.73 and the minimum of this function was $\mu^* = 29.1$ and $C^* = 3.31 \cdot 10^{-10}$ m^2/s. From these values and by using the system flexibility ($1.420 \cdot 10^{-5}$ m^3/MPa), estimated backfill hydraulic conductivity was $2.41 \cdot 10^{-12}$ m/s and backfill compressibility was 0.744 MPa^{-1}. When analysing the pulse tests by means of the finite element simulator, the parameters obtained were: $k = 1.0 \cdot 10^{-11}$ m/s and $m^* = 0.074$ MPa^{-1}. The results in linear time scale are depicted in figure 4.74. A zoom of the second pulse test is performed and depicted in figure 4.75 in logarithmic scale. Backfill porosity was 0.36. Predicted evolution of water pressure at the sensor for both calculations substantially differs at the beginning of the test. Curve Gibson (1) corresponds to parameters obtained by minimising the objective function, and Gibson (2) corresponds to the predicted dissipation process by using the parameters obtained by means of the finite element code. Note that both set of parameters Gibson (1) and Gibson (2) presented in figure 4.73 provided with similar values of the objective function.

The pulse test performed in this sensor clearly shows a change of dissipation speed after 2000 seconds from the beginning of the test. The reasons of such behaviour are not clear. However, the most probable reason is that the flow of water is governed by a higher compressibility/permeability at the beginning of the test, and after some time, the flow of water is governed by the compacted backfill of lower compressibility/permeability. For instance, a withdrawal pulse test performed in granite rock at Grimsel presented linear behaviour with logarithm of time. The measurements are presented in figure 4.76 (Martínez-Landa et al. 2003). During nine seconds, 91 cm^3 were removed from the borehole and water pressure within the borehole was reduced in 189 kPa. The pulse test was firstly analysed with the model by Bredehoeft and Papadopulus (1980). However, from the comparison it is clear that the model was not suitable to reproduce the behaviour measured in this test. The test was simulated by introducing a fracture in the previous approach. Figure 4.77 shows the comparison between the measurements and the simulation by assuming flow in fractured media (Martínez-Landa et al. 2003).

Regarding the pulse test performed in sensor DPP9, it would be possible that a crack was open after the injection of water. The local hydraulic gradient was very high, since water pressure was increased almost 400 kPa. It is also possible that some backfill in contact with the sensor is more pervious due to its heterogeneous behaviour or the existence of a remoulded zone. At this moment, with the information available, it is not possible to conclude what produces the change of slope observed in pulse tests performed in sensor DPP9. As a result, when performing pulse tests in situ, the increase of water pressure has to be limited in those sensors where a high increase of water pressure is obtained (DPP7 and DPP9) in order to prevent cracks and fissures to occur.

● DPP10

Location and arrangement of sensor DPP10 are shown in figure 4.71. This sensor is also very close to the host rock in an area where compaction process was difficult and therefore, low backfill dry specific weight was obtained. The assumed backfill porosity around this sensor was 0.48 as well. Figure 4.78 shows the comparison between the measurements and the finite element simulation. Again, the computed dissipation process does not fit the beginning of the measured curve. The parameters used in these computations were $k = 3.0\cdot10^{-10}$ m/s and $m^* = 0.372$ MPa^{-1}.

4.8.5 *Compilation of the results*

Parameters obtained after the back-analyses and the numerical simulations by using the finite element code are briefly summarised in table 4.8. After this preliminary analysis of the pulse tests, it is possible to plot a map of backfill local permeability and compressibility. Figures 4.79 and 4.80 show those maps for layers 2 and 3 of section A4. Only the results obtained by the finite element code are depicted in those maps, since Gibson's results could be somehow unrealistic if compared with those obtained by the finite element simulations. Nevertheless, parameters obtained by means of Gibson's model present similar patterns than parameters obtained by means of the code.

	Gibson's model					**Finite element simulation**			
Pulse	μ^*	C^* (m^2/s)	m^* (MPa^{-1})	k (m/s)	J_{min} (kPa^2)	μ^*	C^* (m^2/s)	m^* (MPa^{-1})	k (m/s)
DPP3	5.1	$1.58\cdot10^{-8}$	0.420	$6.6\cdot10^{-11}$	916	1.8	$7.48\cdot10^{-8}$	0.150	$1.1\cdot10^{-10}$
DPP5	16.1	$1.58\cdot10^{-9}$	2.471	$3.8\cdot10^{-11}$	609	2.4	$2.70\cdot10^{-8}$	0.372	$1.0\cdot10^{-10}$
DPP7	2.1	$3.02\cdot10^{-8}$	0.050	$1.5\cdot10^{-11}$	791	2.1	$2.94\cdot10^{-8}$	0.052	$1.5\cdot10^{-11}$
DPP8	-	-	-	-	-	4.2	$2.07\cdot10^{-7}$	1.486	$3.0\cdot10^{-09}$
DPP9	29.1	$3.31\cdot10^{-10}$	0.744	$2.4\cdot10^{-12}$	25354	2.6	$1.37\cdot10^{-8}$	0.074	$1.0\cdot10^{-11}$
DPP10	-	-	-	-	-	2.6	$8.23\cdot10^{-8}$	0.372	$3.0\cdot10^{-10}$

Table 4.8: Brief summary of backfill parameters obtained from the simulations by using Gibson's model and the finite element code. Pulse tests performed in sensors DPP8 and DPP10 were not analysed by means of the Gibson's model.

Results at sensors DPP7 and DPP9 are in good agreement with estimated value of backfill hydraulic conductivity from the oedometer test performed in specimen hydrated with 16 g/L of salt and compacted at a dry specific weight of 16.6 kN/m^3 (figure 3.60, chapter 3). Backfill hydraulic conductivity estimated from sensor DPP8 is also in good agreement with estimated hydraulic conductivity from oedometer test performed in a specimen hydrated with 16 g/L and compacted at a dry specific weight of 13.7 kN/m^3 (figure 3.61, chapter 3).

4.9 CONCLUSIONS

A new mini-piezometer with a pressure transducer inside has been designed and built to perform pulse tests and constant head tests in compacted clayey soils. With this new mini-piezometer, an experimental study of backfill hydraulic conductivity was carried out in laboratory and in the ZEDEX gallery by means of constant head tests and pulse tests. Those tests have been numerically analysed with different techniques.

Some constant head tests were performed in laboratory conditions and provided the saturated hydraulic conductivity of the backfill ($6.5 \cdot 10^{-12}$ m/s at a dry specific weight of 15.9 kN/m^3). Darcy's law was validated from these constant head tests varying the hydraulic gradient from 4 to 100. The pulse tests performed in laboratory showed that the new device and its layout can be properly used to study the hydraulic conductivity of low permeability media as this bentonite-crushed granite rock mixture. Four pulse tests were studied and simulated by means of three different models: the Gibson's model (spherical and isotropic, homogeneous and linear elastic medium), the semi-analytical model by Brand & Premchitt (axisymmetric cylindrical coordinates in an isotropic, homogenous and linear elastic medium), and an extended Biot's formulation via FEM (assuming an isotropic, homogeneous and linear elastic behaviour).

The finite element code allowed considering the influence of different flow boundary conditions on the pulse test results. The small amount of water necessary to perform the pulse test, when the no-flow boundary condition was prescribed, notably decreased the time of the dissipation process if compared with the longer dissipation when water pressure was prescribed at the outer part of the cell. The Gibson’s analytical model and the semi-analytical model by Brand & Premchitt did not reproduce correctly the results for the impervious boundary condition as it was expected. The finite element formulation, however, described the no-flow boundary condition pulse tests correctly, and the parameters estimated were more realistic.

Hydraulic conductivity calculated with the three different models from pulse tests 3 and 4 (water pressure prescribed at the outer part of the cell) was in good agreement with the hydraulic conductivity assessed from the constant head test. However, variability of estimated backfill compressibility by means of Gibson’s model and cylindrical equalization chart was somehow wide. The analysis of the pulse tests with an extended Biot’s formulation via FEM provided with good results when estimating backfill compressibility. Soil compressibility obtained in such calculations was in good agreement with measured ones in bentonite – crushed granite mixtures by Radhakrishna & Chan (1982) at similar dry specific weights. The most important difference, when the three approaches were compared, was the geometry and the use of the intake factor for a cylindrical piezometer in a spherical geometry. The use of the equivalent radius concept for cylindrical piezometers can introduce important differences in the estimated parameters. Due to the small size of this cell compared with the mini-piezometer size, using the equivalent radius concept introduced errors in the compressibility estimation with the Gibson’s model.

Differences when studying the pore water pressure dissipation by means of Biot's approach and Terzaghi's approach were investigated. It is clear that total mean stress changed when water was suddenly injected in the porous medium. Nonetheless, estimated total mean stress changes were not significant. For instance, total mean stress increased up to 8 kPa in the contact of soil and piezometer when water pressure increased 206 kPa after a numerical analysis of a pulse test with the finite element code. To overcome this influence, the last part of the pulse test can be studied to estimate the hydraulic conductivity and the soil compressibility (beyond t_{50}).

The necessary tools to carry out and analyse the pulse tests will be perform in section A4 in the ZEDEX gallery have been finally debugged. If the medium is big enough (at the field case if the minipiezometer is far away from the rock), Gibson's model can be easily used to estimate the hydraulic conductivity. Constant head tests can be performed in section A4 and easily analysed with the analytical solution provided by Gibson (1963). If piezometers are close to the host rock (where boundary conditions can be more complex) then, CODE_BRIGHT can be used to analyse the pulse tests performed in such piezometers. If good results estimating hydraulic conductivity and soil compressibility from slug or pulse tests are required, a simulation with a hydro-mechanical code via finite element method is probably the best option to minimise the errors introduced by the analytical or semi-analytical models available in the literature. In addition, the measurement of the necessary volume of water to increase the water pressure within the mini-piezometer is very important to correctly estimate the hydraulic conductivity.

Eighteen pulse tests were performed in the ZEDEX gallery in late March 2003. Prior to the pulse tests, trapped air was removed from the mini-piezometers and water pressure was measured in an external pressure transducer. Measured water pressure within the mini-piezometers shows that the saturation process is, probably, finished. Six out of the thirteen mini-piezometers are actually out of order after almost 4 years since the installation. Six pulse tests out of eighteen were analysed by means of CODE_BRIGHT and Gibson's model. From the analyses, it was possible to plot a map of backfill compressibility and hydraulic conductivity at section A4.

The calculations confirmed that lower hydraulic conductivity is measured in areas where the compaction effort was higher than the estimated permeability in areas where the compaction effort was not so high (close to the host rock). Estimated backfill hydraulic conductivity in sensors DPP7 and DPP9 is in agreement with estimated backfill hydraulic conductivity at a dry specific weight of 16.6 kN/m^3 and salt concentration of 16 g/L. The range of estimated local backfill hydraulic conductivity is large (up to two orders of magnitude) and that will complicate the analysis of the global flow tests to be performed throughout 2003 and 2004. Influence of 3D effects on the problem is important and real boundary conditions (flow and mechanical ones) are not known in those sensors close to the host rock.

Moreover, the dissipation process performed in sensor DPP9 showed a non-expected linear behaviour with logarithm of time during the first 2000 seconds from the beginning of the test. None of the models, the finite element code and the analytical model, was able to reproduce the observed behaviour at initial times. The most likely explanation of the observed behaviour is the existence of a remoulded zone around the sensor, but it could be possible that cracks or fissures were produced due to the high increase of water pressure close to the sensor. Consequently, attention must be paid to backfill hydraulic fracture when performing flow tests in situ.

The most important consequences are the validity of the pulse test in the laboratory and in situ to estimate local hydraulic conductivity of low permeability media in such conditions and, finally, the reliability of the layout designed and developed by AITEMIN and the Department of Geotechnical Engineering and Geosciences of UPC.

4.10 REFERENCES

AITEMIN (1999). Äspö, Backfill and plug test. Sistema de medida local de permeabilidad mediante ensayos de pulso. Desarrollo, puesta a punto e instalación. Internal Report. Cod. Adj. 703267. (In Spanish). Madrid, Spain.

Börgesson, L., Johannesson, L.E. & Sandén, T. (1996). Backfill materials based on crushed rock. Geotechnical properties determined in laboratory. SKB Progress Report **HRL-96-15**, Sweden.

Brace, W.F., Walsh, J.B. & Frangos, W.T. (1968). Permeability of granite under high pressure. *Journal of Geophysical Research*, **73**, p. 2225-2236.

Brand, E.W. & Premchitt, J. (1980). Shape factors of cylindrical piezometers. *Géotechnique*, **30** (4), p. 369-384.

Brand, E.W. & Premchitt, J. (1982). Response characteristics of cylindrical piezometers. *Géotechnique*, **32** (3), p. 203-216.

Bredehoeft, J.D. & Papadopulos, I.S. (1980). A method for determining the hydraulic properties of tight formations. *Water Res. Res.,* **16** (1), p. 233-238.

Carrera, J. & Neuman, S.P. (1986). Estimation of aquifer parameters under transient and steady state conditions, 1, Maximum likelihood method incorporating prior information. *Water Res. Res.,* **22** (2), p. 199-210.

Carrera, J., Samper, J., Vives, L. & Kulhman, U. (1989). Automatic inverse methods for the analysis of pulse tests: Application to four pulse tests at the Leuggern Borehole. NAGRA. **TR 88-34**. Switzerland.

Chapuis, R.P. (1998). Overdamped slug tests in monitoring wells: review of interpretation methods with mathematical, physical and numerical analysis of storativity influence. *Canadian Geotechnical Journal*, **35**, 697-719.

Cryer, C.W. (1963). A comparison of the three-dimensional consolidation theories of Biot and Terzaghi. *Quarterly Journal of Mechanics and Applied Mathematics*, **16** (4), p. 401-412.

Cooper, H.H.(Jr), Bredehoeft, J.D. & Papadopulos, I.S. (1967). Response of a finite diameter well to an instantaneous charge of water. *Water Res. Res.,* **3** (1), p. 263-269.

de Jong, J. (1953). Consolidation around pore pressure meters. *J. Applied Physics,* **24** (7), p. 922-928.

Dixon, D.A., Graham J. & Gray, M.N. (1999). Hydraulic conductivity of clays in confined tests under low hydraulic gradients. *Can. Geotech. J.,* **36**, p. 815-825.

Gibson, R.E. (1963). An analysis of system flexibility and its effect on time lag in pore-water pressure measurements. *Géotechnique,* **13** (1), p. 1-9.

Gibson, R.E., Knight, K. & Taylor, P.W. (1963). A critical experiment to examine theories of three-dimensional consolidation". *Proc. European Conference on Soil Mechanics and Foundation Engineering*, Vol **1**, p. 69-76. Weisbaden, Germany.

Grisak, G.E., Pickens, J.F., Belanger, D.W. & Avis, J.D. (1985). Hydreogeologic testing of crystalline rocks during the NAGRA deep drilling program. **NTB 85-08**. Switzerland.

Hart, D.J. & Wang, H.F. (2001). A single test method for determination of poroelastic constants and flow parameters in rocks with low hydraulic conductivities. *Int. J. of Rock Mechanics & Min. Sci*, **38**, p. 577-583.

Hsieh, P.A., Tracy, J.V., Neuzil, C.E., Bredehoeft, J.D. & Silliman S.E. (1981). A transient laboratory method for determining the hydraulic properties of tight rocks – I. Theory. *Int. J. Rock Mech. Min. Sci. & Geomech. Abstr.,* **18**, p. 245-252.

Hughes, T.J.R. (1980). Generalisation of selective integration procedures to anisotropic and nonlinear media. *Int. J. Num. Meth. Eng.*, **15,** p. 1413-1418.

Hvorslev, M. J. (1951). Time-lag and soil permeability in ground-water observations. *US Army Corps of Engineers, Waterways Experiment Station Bulletin 36. Mississippi, USA.*

Johannesson, L.E., Börgesson, L. & Sandén, T. (1999). Backfill materials based on crushed rock (part 2). Geotechnical properties determined in laboratory. SKB ÄHRL **IPR-99-23**, Sweden.

Ledesma, A., Gens, A. & Alonso, E.E. (1996). Estimation of parameters in Geotechnical Backanalysis - I. Maximum likelihood approach. *Computers and Geotechnics*, **18**, p. 1-27.

Marquardt, D.W. (1963). An algorithm for least-squares estimation of non-linear parameters. *J. Soc. Indust. Appl. Math*., **11** (2), p. 431-441.

Martínez-Landa, L., Alcantud, A. & Carrera, J. (2003). Interpretation of hydraulic tests at the final heating test phase. Report for the FEBEX Project (ENRESA). 70-Hyd-L5-004. Spain, Barcelona.

Mata, C. & Ledesma, A. (2001). In situ measurement of local saturated permeability of compacted clayey soils by means of minipiezometers. *Proc. XVth International Conference on Soil Mechanics and Geotechnical Engineering*, (ICSMGE), Vol **1**, p. 451-454, Istanbul, Turkey.

Mitchell, J.K. (1993). *Fundamentals of Soil Behaviour*. 2nd edition, John Wiley, NY.

Neuzil, C.E. (1982). On conducting the modified 'Slug' test in tight formations. *Water Res. Res.*, **18** (2), p. 439-441.

Neuzil, C.E. (1986). Groundwater flow in Low-Permeability Environments. *Water Res. Res.*, **22** (8), p. 1163-1195.

Neuzil, C.E., Cooley, C., Silliman, S.E., Bredehoeft, J.D. & Hsieh, P.A. (1981). A transient laboratory method for determining the hydraulic properties of tight rocks – II. Application. *Int. J. Rock Mech. Min. Sci. & Geomech. Abstr.,* **18**, p. 253-258.

Olivella, S., Gens, A., Carrera, J. & Alonso, E. E. (1996). Numerical formulation for a simulator (CODE_BRIGHT) for the coupled analysis of saline media. *Engineering Computations*, **13**, p. 87-112.

Premchitt, J. & Brand, E. W. (1981). Pore pressure equalization of piezometers in compressible soils. *Géotechnique,* **31** (1), p. 105-123.

Radhakrishna, H. S., & Chan, H.T. (1982). Laboratory study of physical properties of clay buffers for a nuclear fuel waste vault. *Proc. Int. Conf. On Radioactive Waste Management*, Winnipeg, Manitoba, September 12-15. (1982). M.A. Feraday (Ed.). Toronto, Ontario: Canadian Nuclear Society, 84-90.

Push, R. (1982). Mineral-water interactions and their influence on the physical behaviour of highly compacted Na bentonite. *Can. Geotech. J.*, **19**, p. 381-387.

Ratnam S., Soga K. & Whittle R.W. (2001). Revisiting Hvorslev's intake factors using the finite element method. *Géotechnique*, **51**, No 7, 641-645.

Schiffman, R.L., Chen, A.T-F. & Jordan, J.C. (1969). An analysis of consolidation theories. *J. Soil Mechanics and Foundations Div.*, **95** SM1, p. 285-311.

Selvadurai, A.P.S., Boulon, M.J. & Nguyen, T.S. (2001). The permeability of an intact granite. *Proc. of the Int. Workshop on Key Issues in Waste Isolation Research*, Preprint, P. Delage, (Ed.), Ecole Nationale des Ponts et Chaussées, Paris.

Tavenas, F., Leblond, P., Jean, P. & Leroueil, S. (1983). The permeability of natural soft clays. Part I: Methods of laboratory measurement. *Can. Geotech. J.,* **20**, p. 629-644.

Verruijt, A. (1965). Consolidatie in drie dimensies: bolysimmetrische consolidatie in een oneindig massief. LGM *Meded.* **9**, No 3, 49-72. (In Dutch).

Verruijt, A. (1984). The theory of consolidation. In Fundamentals of Transport Phenomena in Porous Media. J. Bear & M.Y. Corapcioglu (Eds.). NATO ASI Series. Series E: Applied Sciences – No. 82.

Wiggins, R.A. (1972). The general linear inverse problem: implication of surface waves and free oscillation for earth structure. *Rev. Geophys. Space Phys.*, **10**, p. 251-285.

Zhang, M., Takahashi, M., Morin, R. H., & Esaki, T. (2000). Evaluation and Application of the Transient-Pulse Technique for Determining the Hydraulic Properties of Low-Permeability Rocks—Part 2: Experimental Application. *Geotechnical Testing Journal,* **23** (1), p. 091–099.

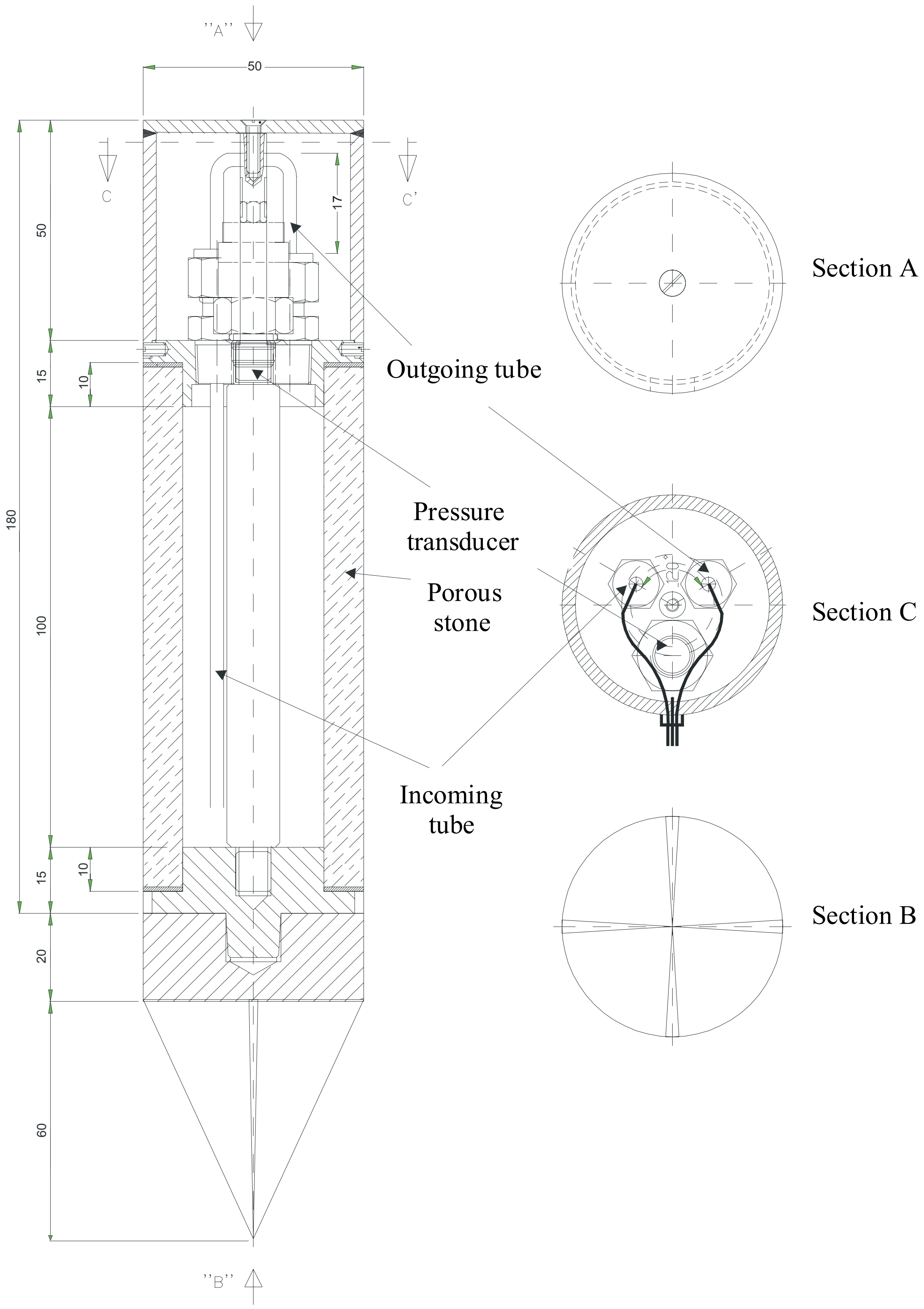

Figure 4.1: Side view of the designed mini-piezometer. Dimensions in millimetres (AITEMIN, 1999).

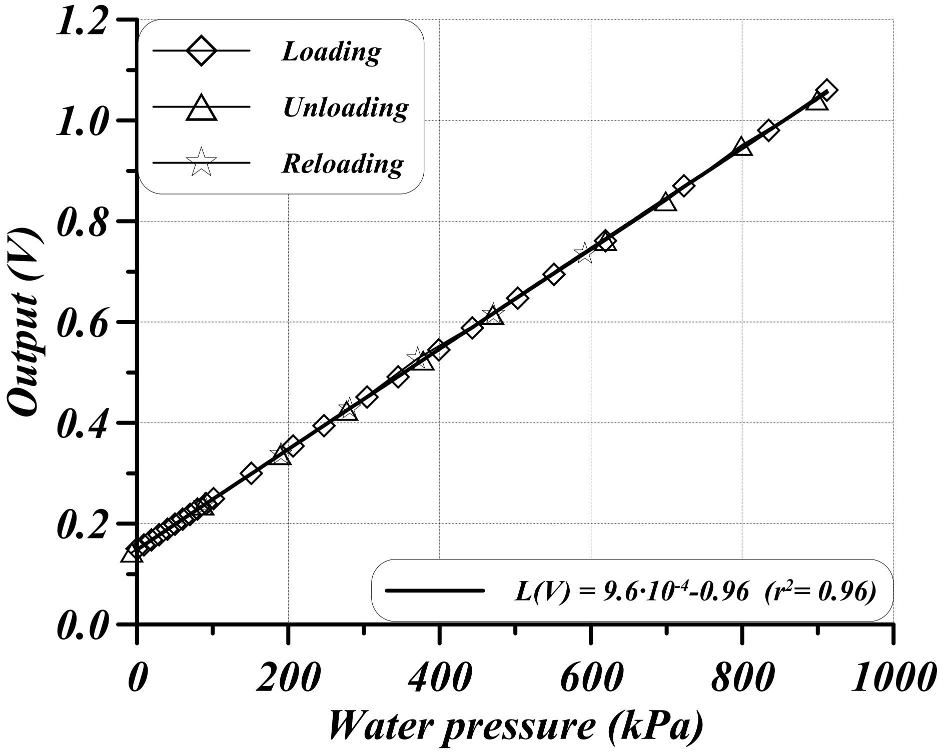

Figure 4.2: DPPS calibration performed in the laboratory. A GDS pressure system was used to perform this calibration.

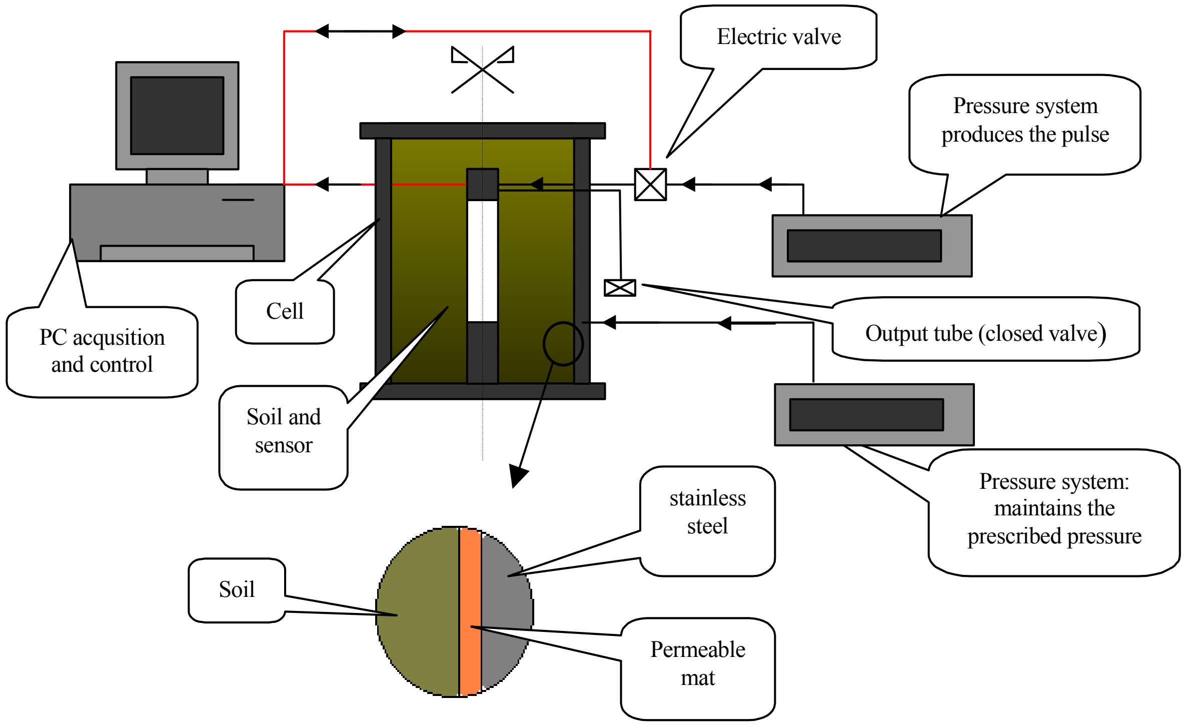

Figure 4.3: Scheme of the pulse test in laboratory.

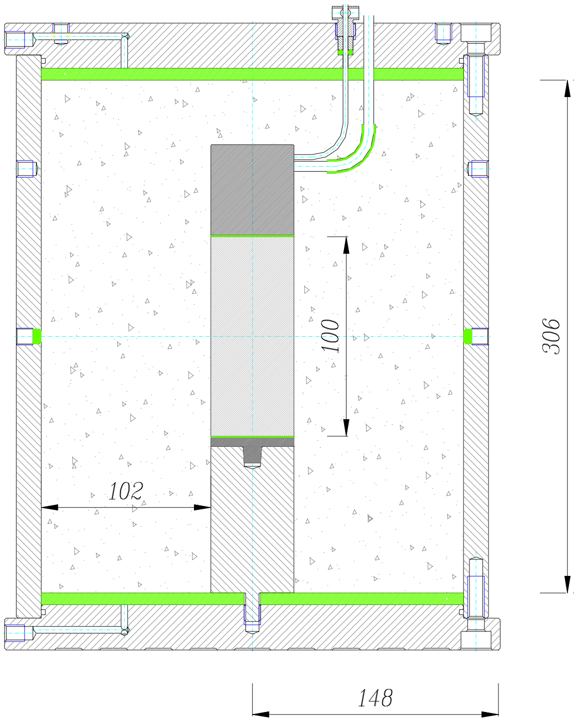

Figure 4.4: Side view of the cell used to carry out constant and variable head tests in laboratory. Dimensions in mm.

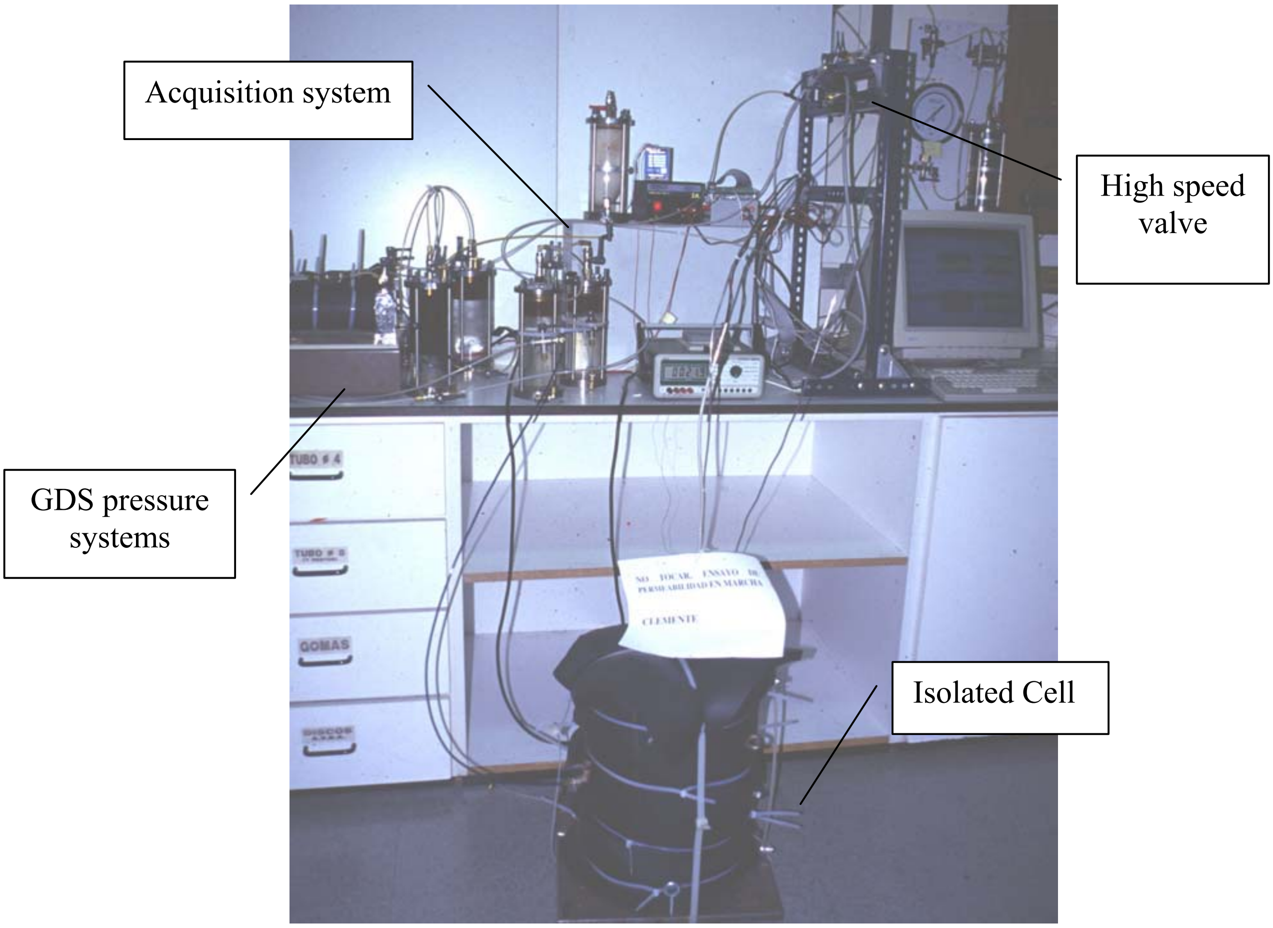

Figure 4.5: Layout used to perform constant head and pulse tests at the designed cell. Two GDS pressure systems, the high speed valve and the acquisition system are the main important components of this make up. The large reservoirs were isolated to decrease temperature effects.

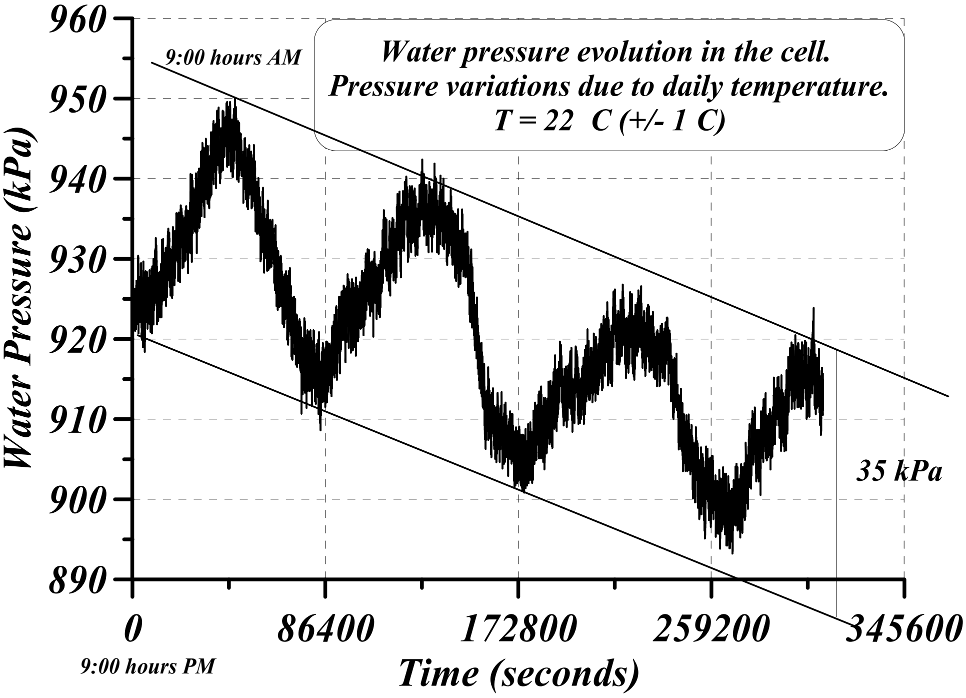

Figure 4.6: Monitored water pressure evolution in the cell due to daily temperature variations. The variations are produced by the thermal deformations of the cell.

Figure 4.7: Compacted backfill specimen into the cell. Two stainless steel tubes (incoming and outgoing water from the DPPS) and a cable with the electric connexions came out from the backfill. A porous filter was placed at the top of the specimen and then the cell was closed.

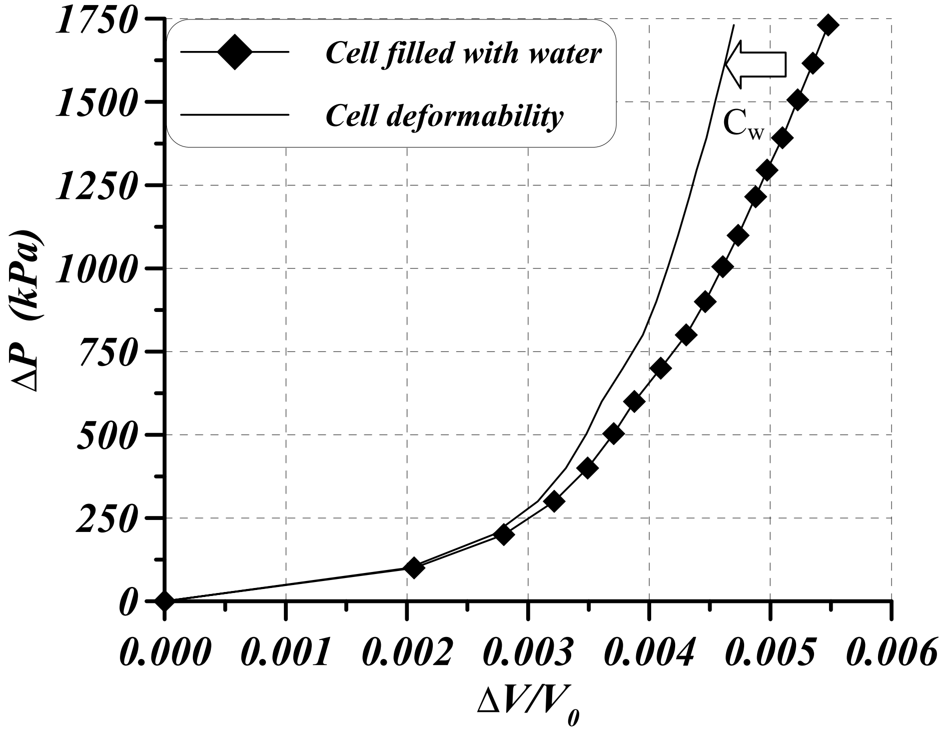

Figure 4.8: Cell deformability calibration performed with de-aired water. C_w represents the effect of water compressibility within the cell.

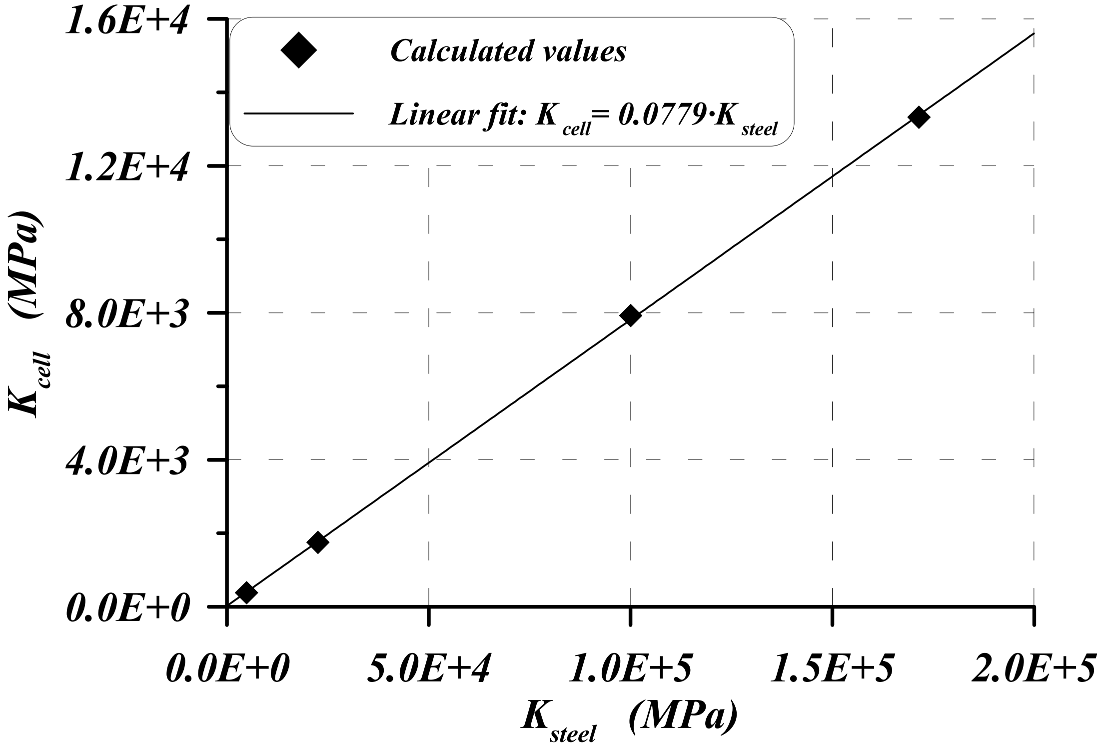

Figure 4.9: Computed values of the cell compressibility, $K_{cell}^{computed}$, with different values of steel bulk modulus. This relationship was used to estimate the necessary or equivalent steel bulk modulus after the cell compressibility had been determined. The value of the Poison's ratio was always 0.3.

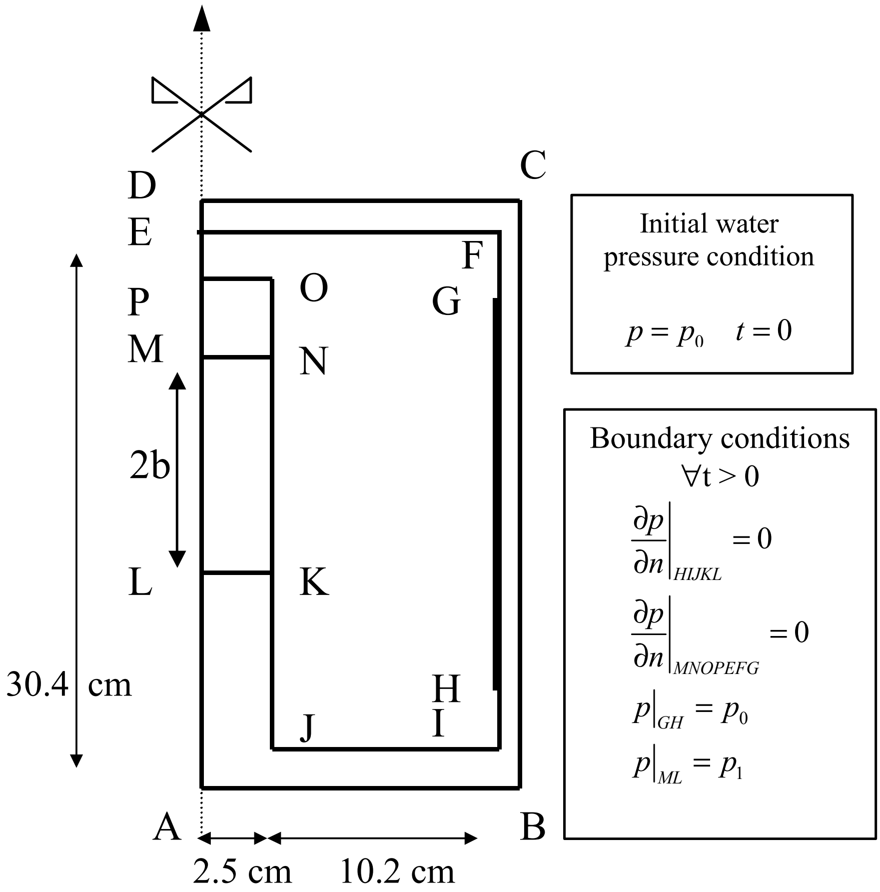

Figure 4.10: Boundary and initial conditions of the constant head test performed in the cell.

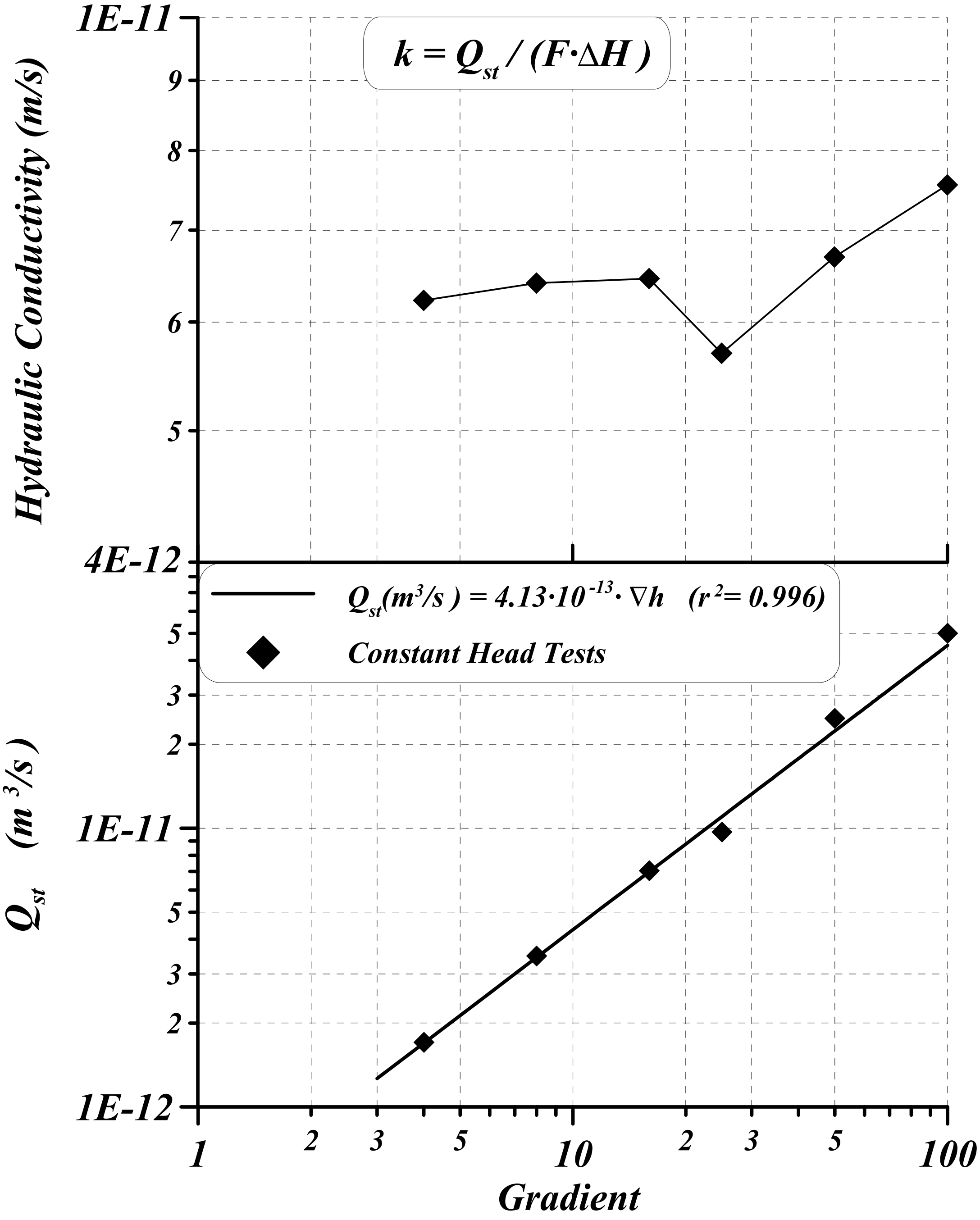

Figure 4.11: Hydraulic conductivity vs maximum hydraulic gradient: dry specific weight of the specimen was 15.9 kN/m^3 and de-ionised water was used to saturate it. Darcy's Law was validated for this material and at this range of gradients.

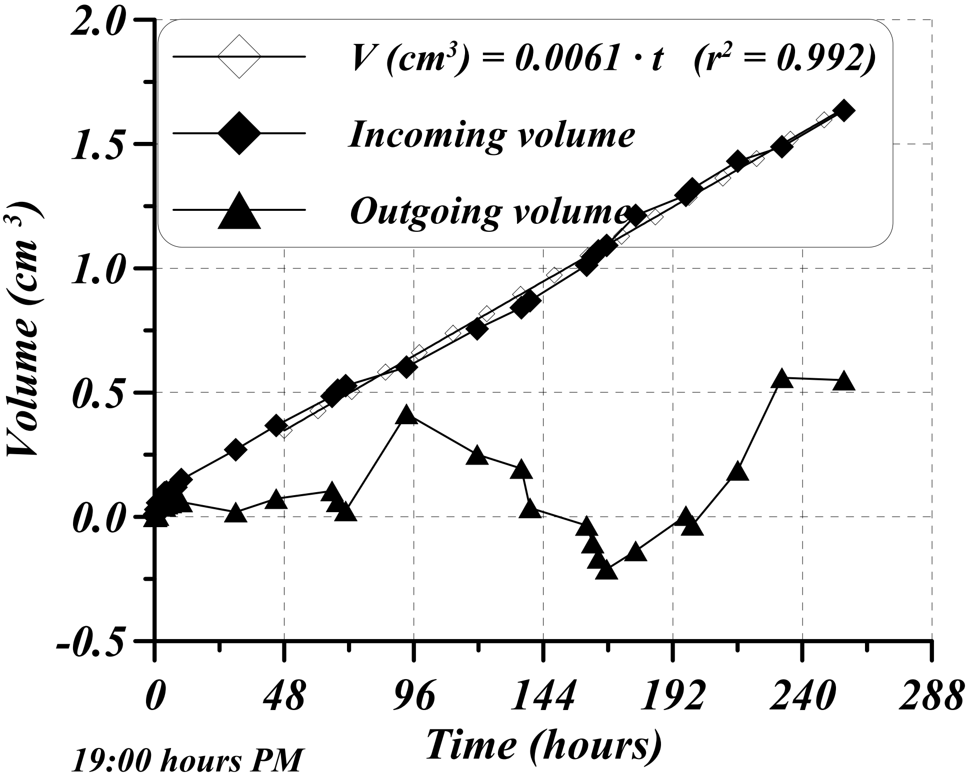

Figure 4.12: Measured incoming and outgoing water volume from the backfill specimen hydrated with deionised water. Average maximum gradient in the cell was 4. It is obvious how daily temperature variations can affect the outgoing volume of water due to cell thermal deformations.

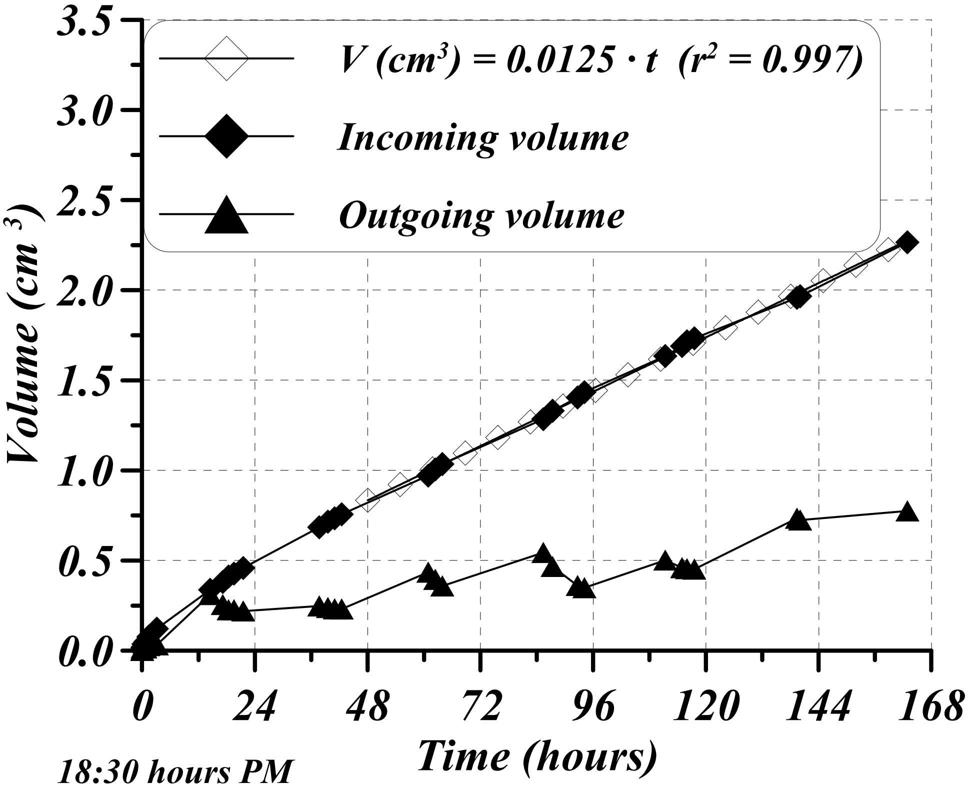

Figure 4.13: Measured incoming and outgoing water volume from the backfill specimen when maximum applied gradient in the cell was 8. It is clear that during the day the shape of the curve is flat, which means that the cell increased its volume and the specimen had larger water storing.

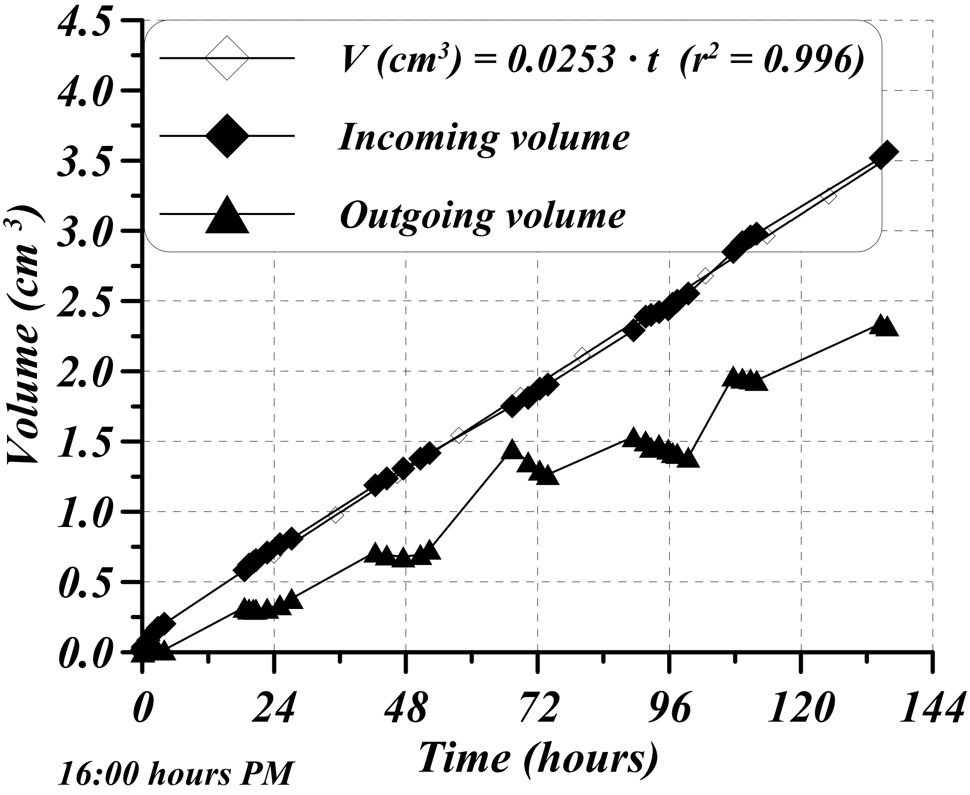

Figure 4.14: Measured incoming and outgoing water volume from the backfill specimen when maximum applied gradient in the cell was 16.

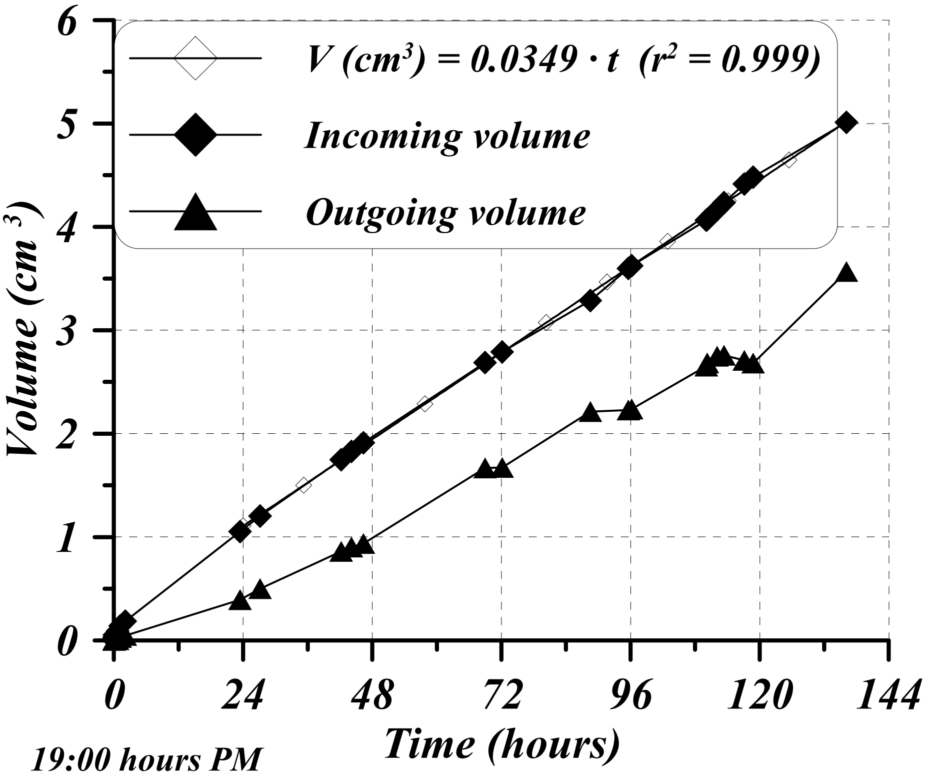

Figure 4.15: Measured incoming and outgoing water volume from the backfill specimen when maximum applied gradient in the cell was 25.

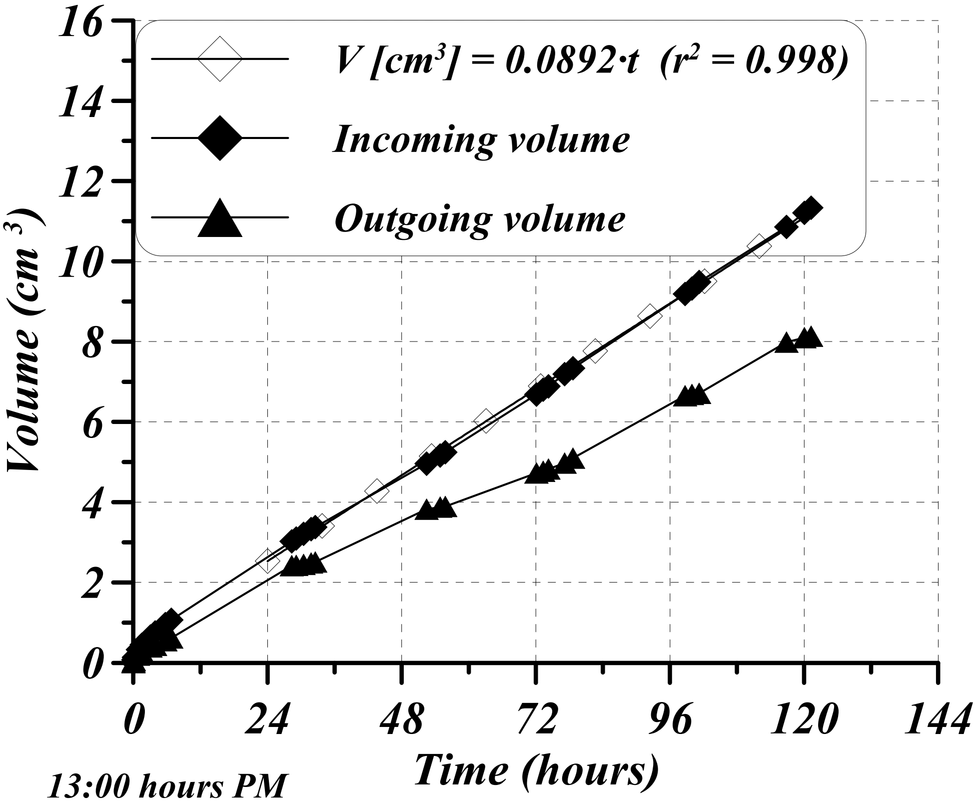

Figure 4.16: Measured incoming and outgoing water volume from the backfill specimen when maximum applied gradient in the cell was 50.

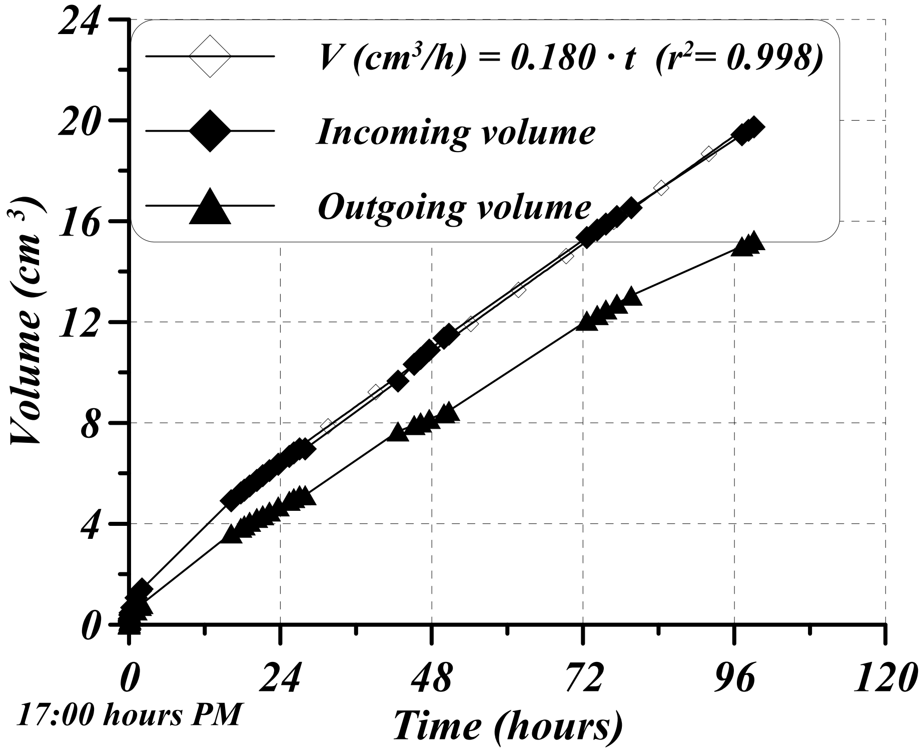

Figure 4.17: Measured incoming and outgoing water volume with de-ionised water and a maximum applied gradient in the cell of 100. This figure shows how the bigger the driving force, the smaller the effects of daily temperature variations on the flow tests.

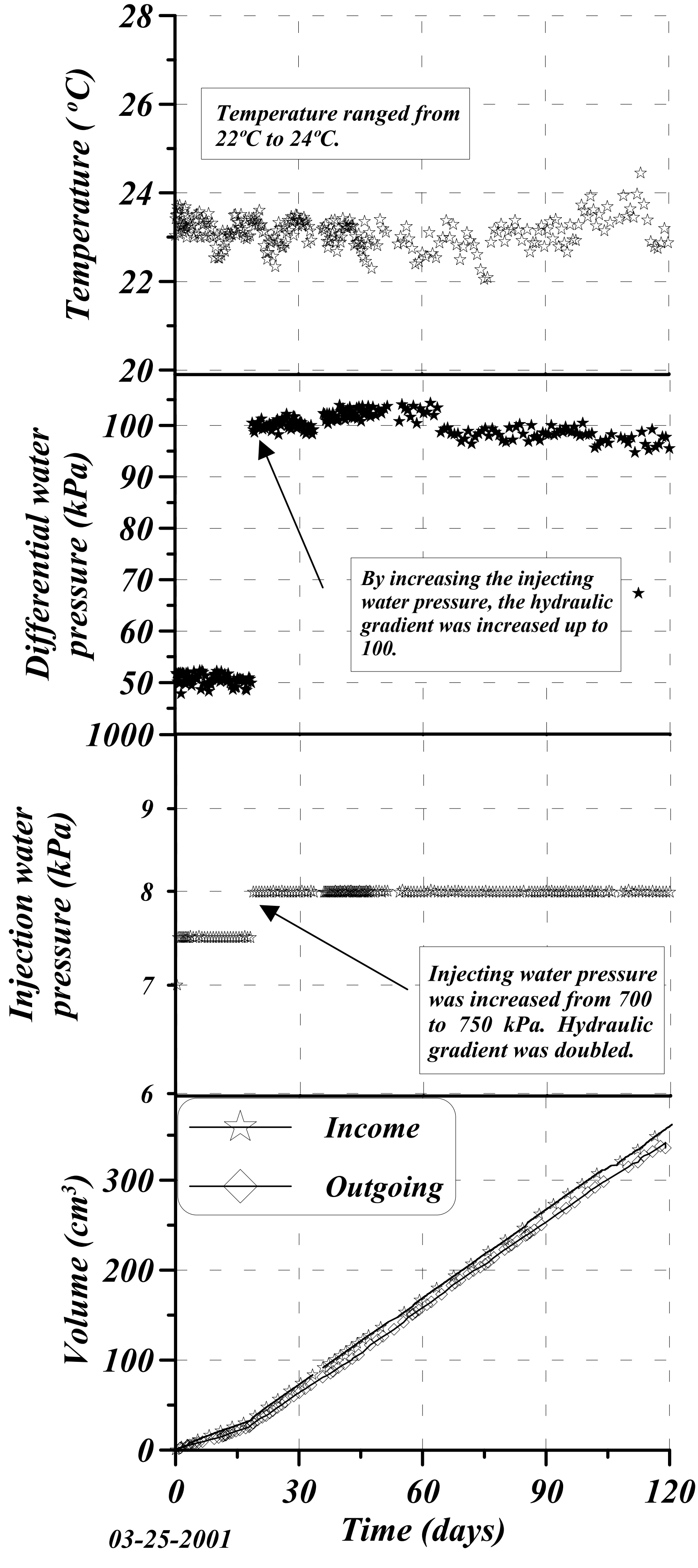

Figure 4.18: Evolution of different variables during a constant head flux performed in the radial cell. This test was performed in the cell after the six constant head tests previously carried out in order to check the saturation of the specimen and the effectiveness of the thermal isolation of the cell.

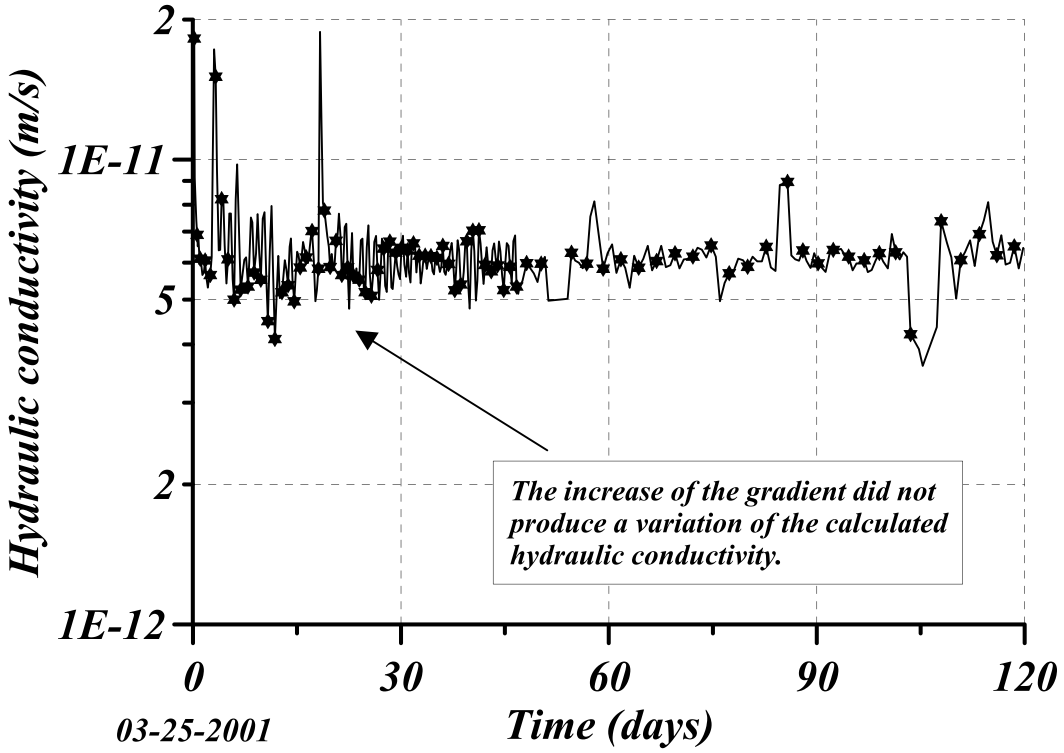

Figure 4.19: Evolution of the computed hydraulic conductivity. It is clearly observed that the increase of injecting water pressure from 750 kPa to 800 kPa in the DPPS did not change the calculated hydraulic conductivity.

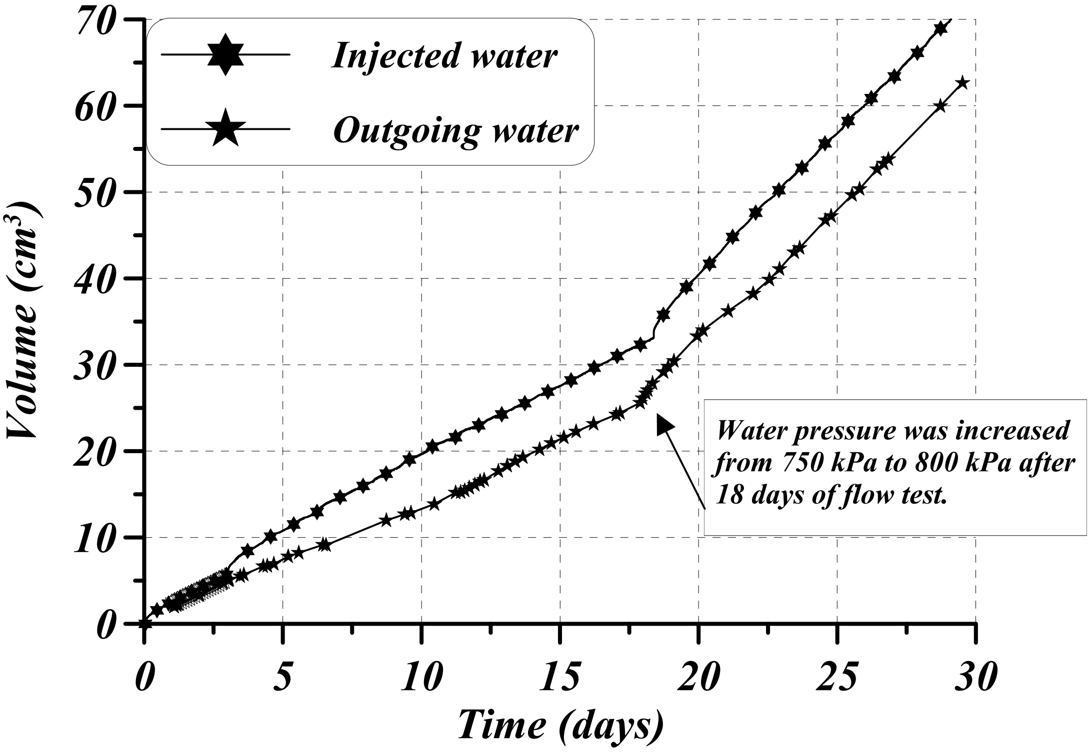

Figure 4.20: Zoom of the first 30 days of the evolution of incoming and collected water in the last constant head test performed in the cell. It confirmed that the backfill was fully saturated.

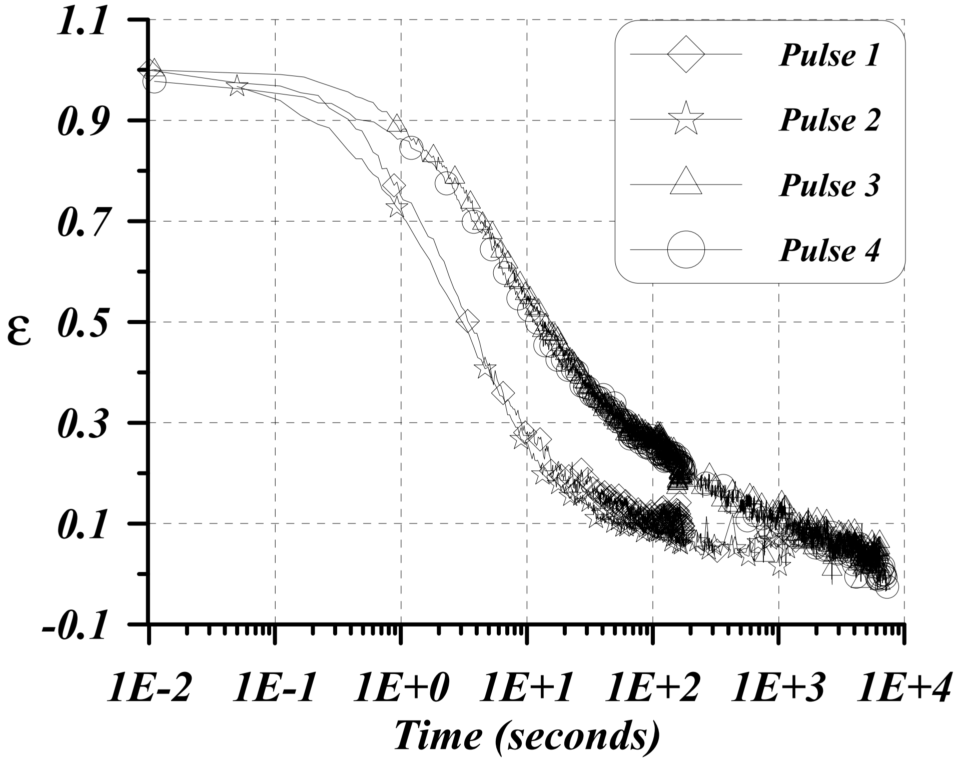

Figure 4.21: Dimensionless comparison among the no-flow pulse tests (number 1 and 2) and the prescribed water pressure pulse tests (3 and 4).

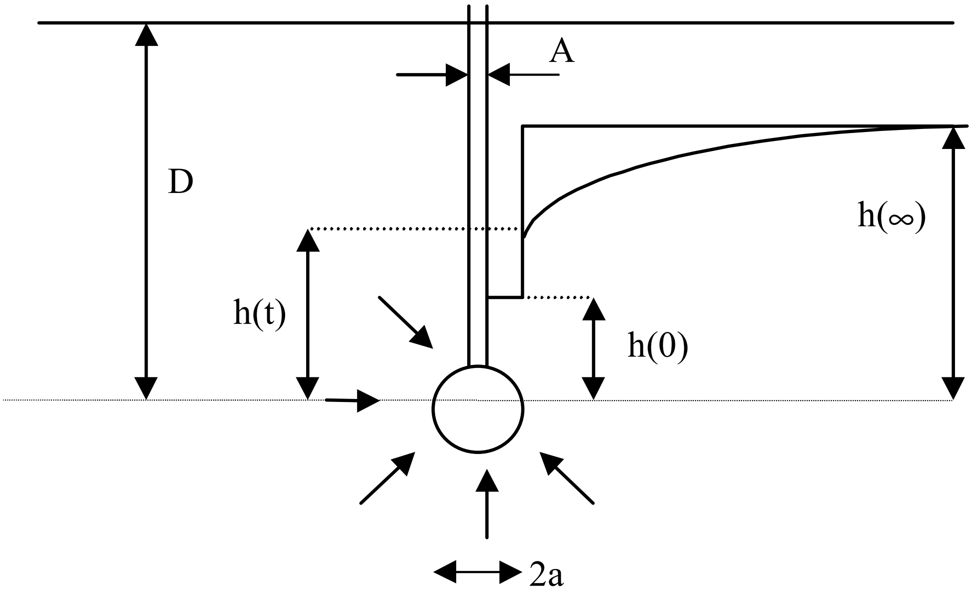

Figure 4.22: Geometry of the problem solved by Gibson (1963). Spherical tip in an isotropic, homogenous and elastic infinite medium.

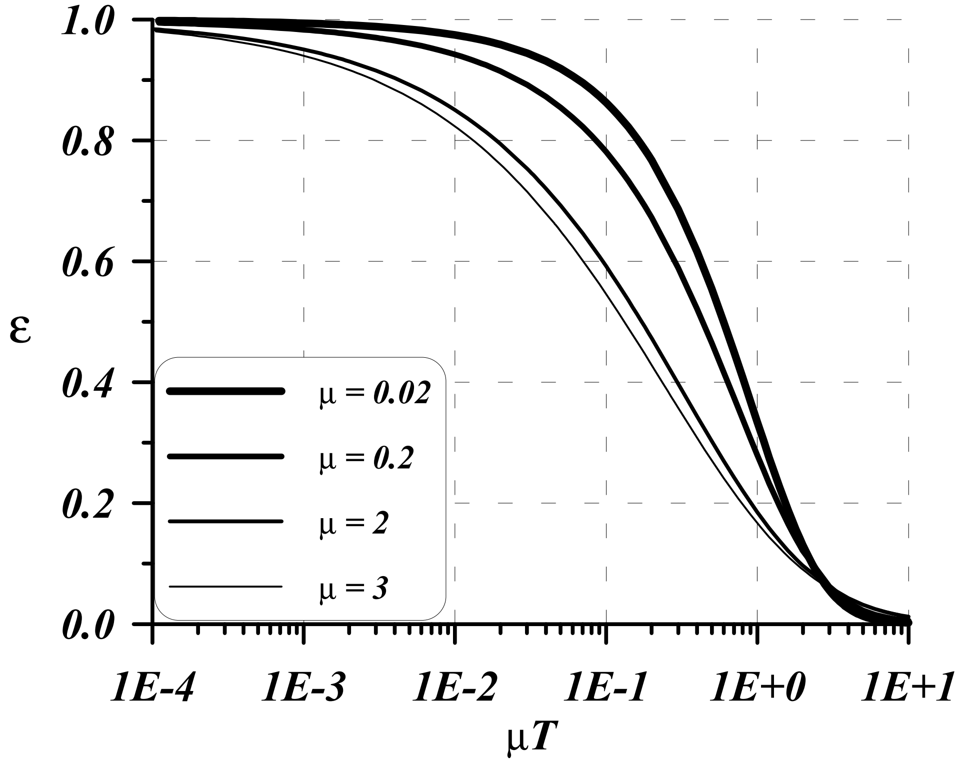

Figure 4.23: Some curves calculated after programming the solutions provided by Gibson (1963) when μ < 4.

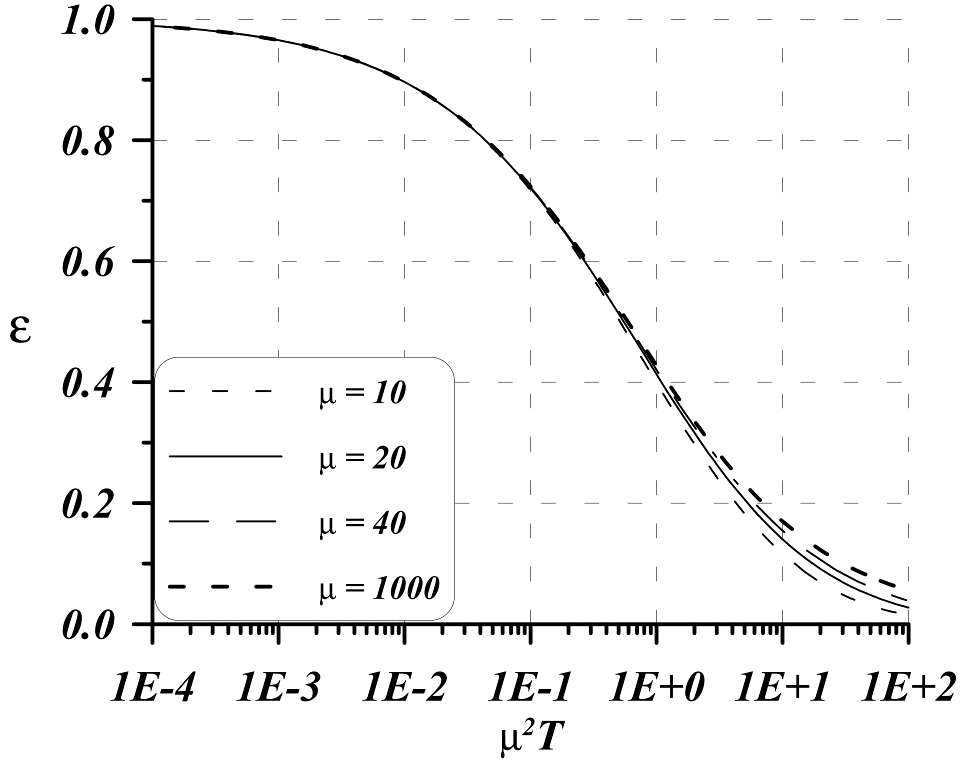

Figure 4.24: Some curves calculated after programming the solutions provided by Gibson (1963) when μ > 4.

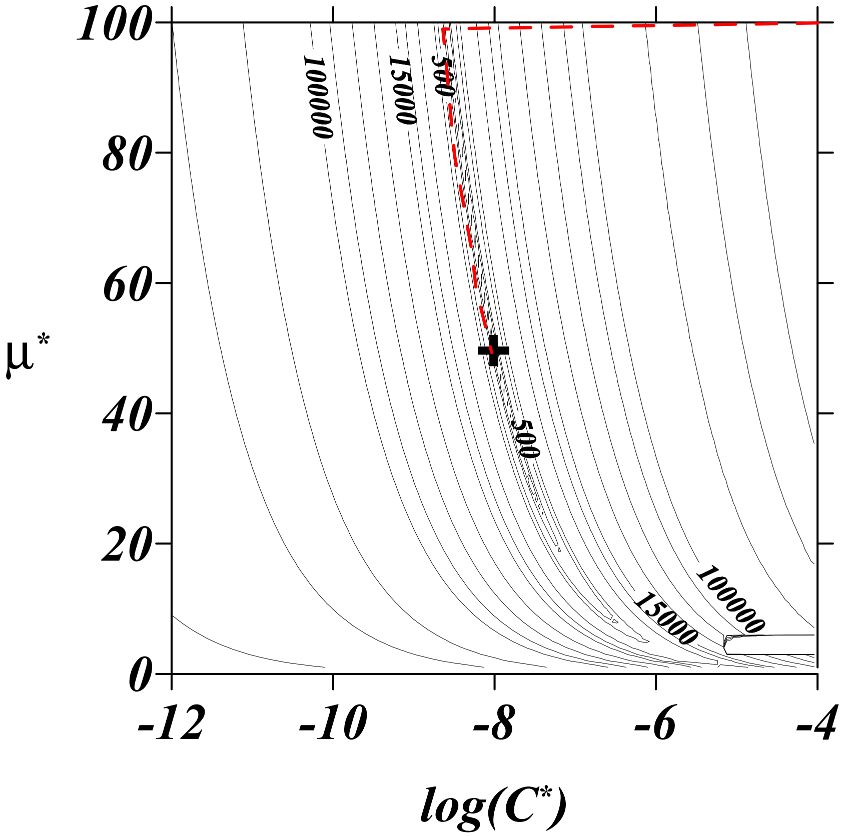

Figure 4.25: Contour plot of the objective function of the synthetic case generated with the Gibson model. It is also shown the trajectory followed by the optimisation procedure starting from $\mu^* = 100$ and $\log C^* = -4$.

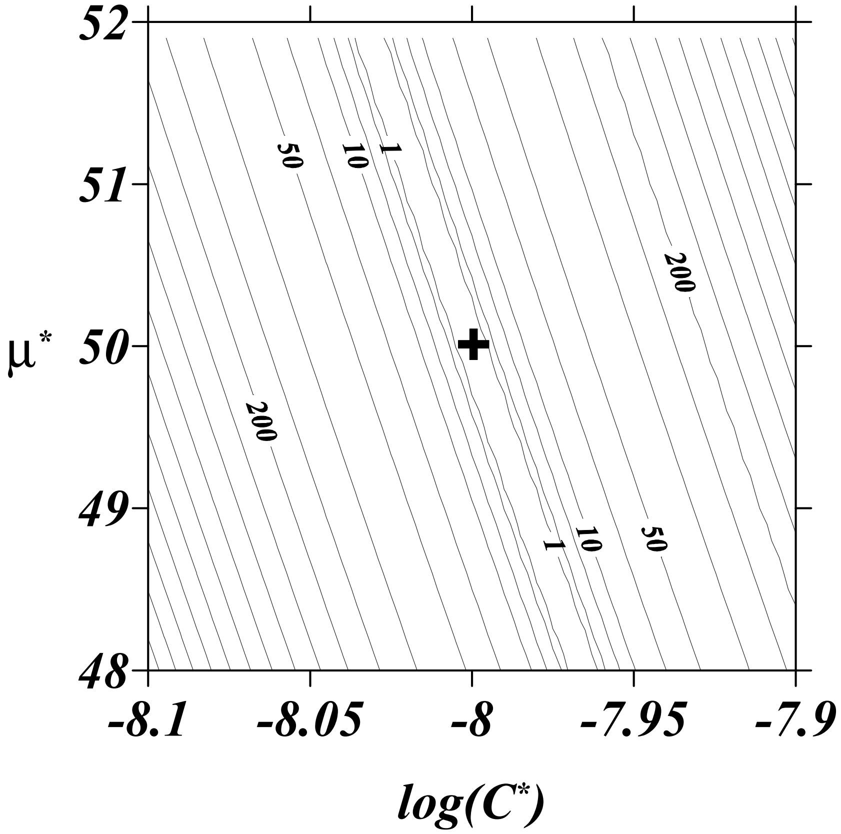

Figure 4.26: Zoom of the surrounding area to the minimum of the generated objective function for the synthetic case.

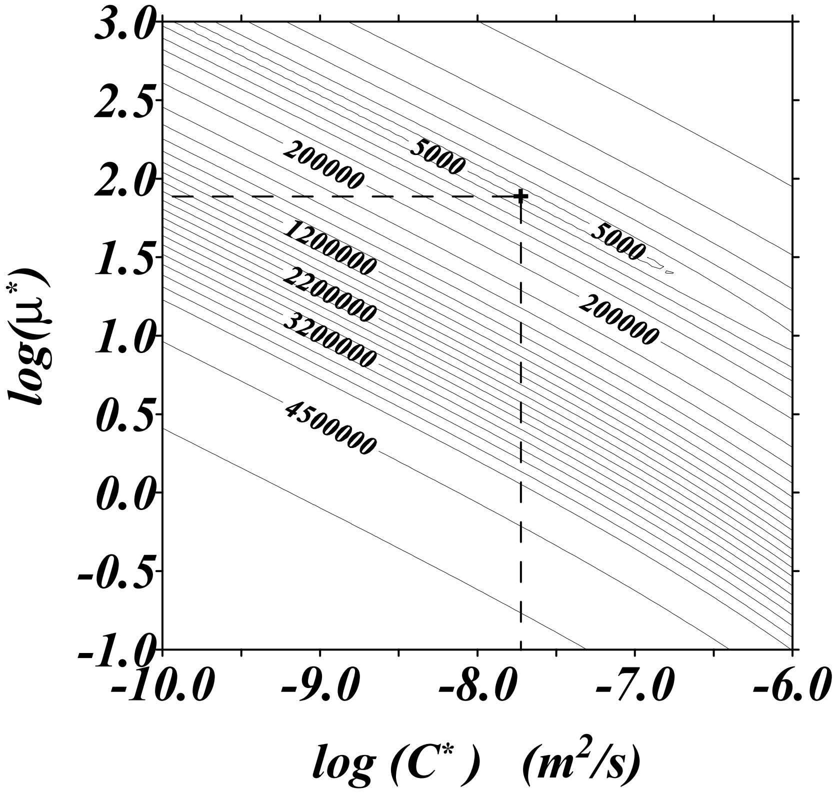

Figure 4.27: Contour map of the objective function of pulse test number 3 using Gibson's model. For real pulse tests double logarithmic axis were chosen.

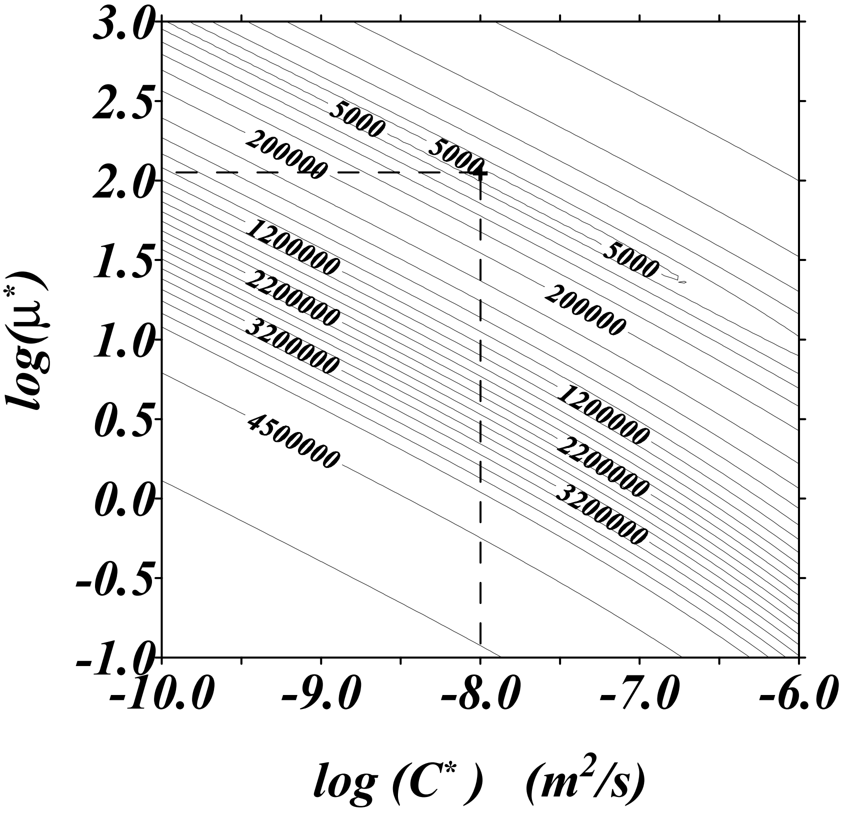

Figure 4.28: Contour map of the objective function of pulse test number 4 by means of Gibson model.

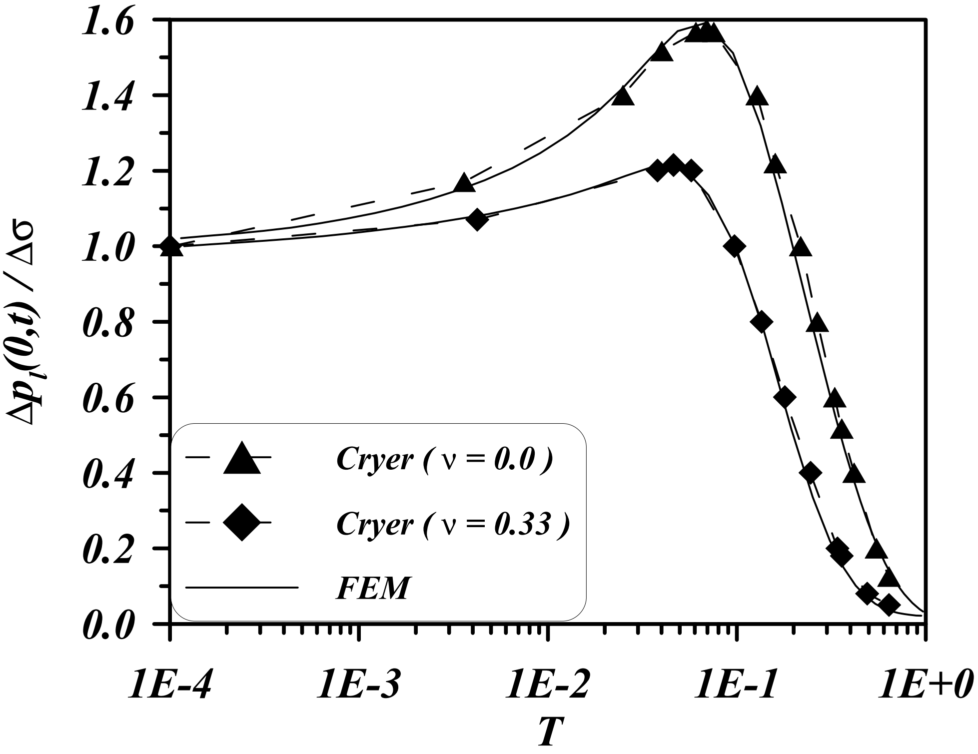

Figure 4.29: Validation of the numerical code. Solution of the Cryer problem for different Poisson's coefficients.

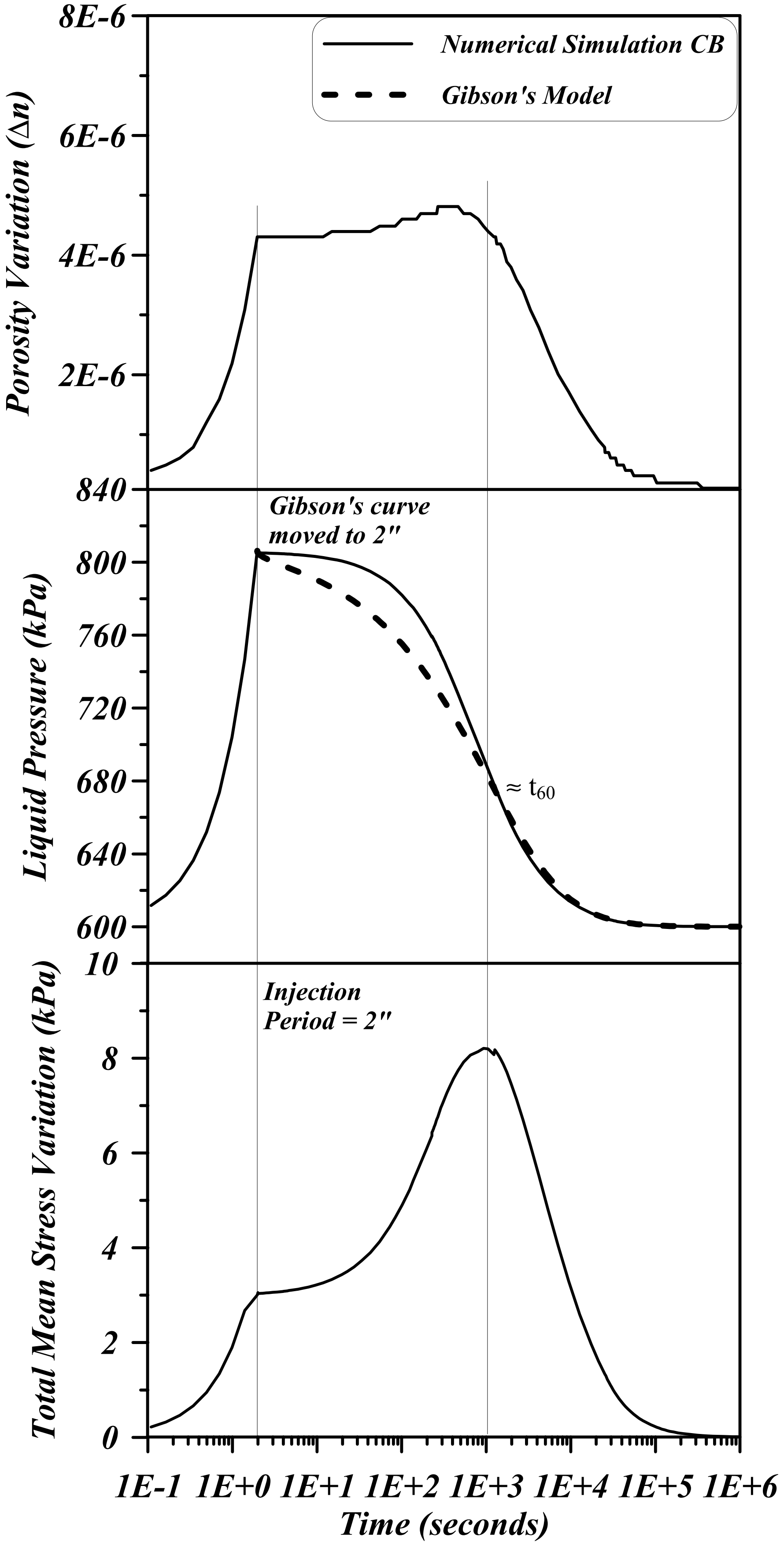

Figure 4.30: Comparison of the analytical solution by Gibson and the predicted numerical results for the same parameters in the soil in contact with the spherical piezometer. Gibson theory only provides with liquid pressure. Numerical results include also porosity and mean stress.

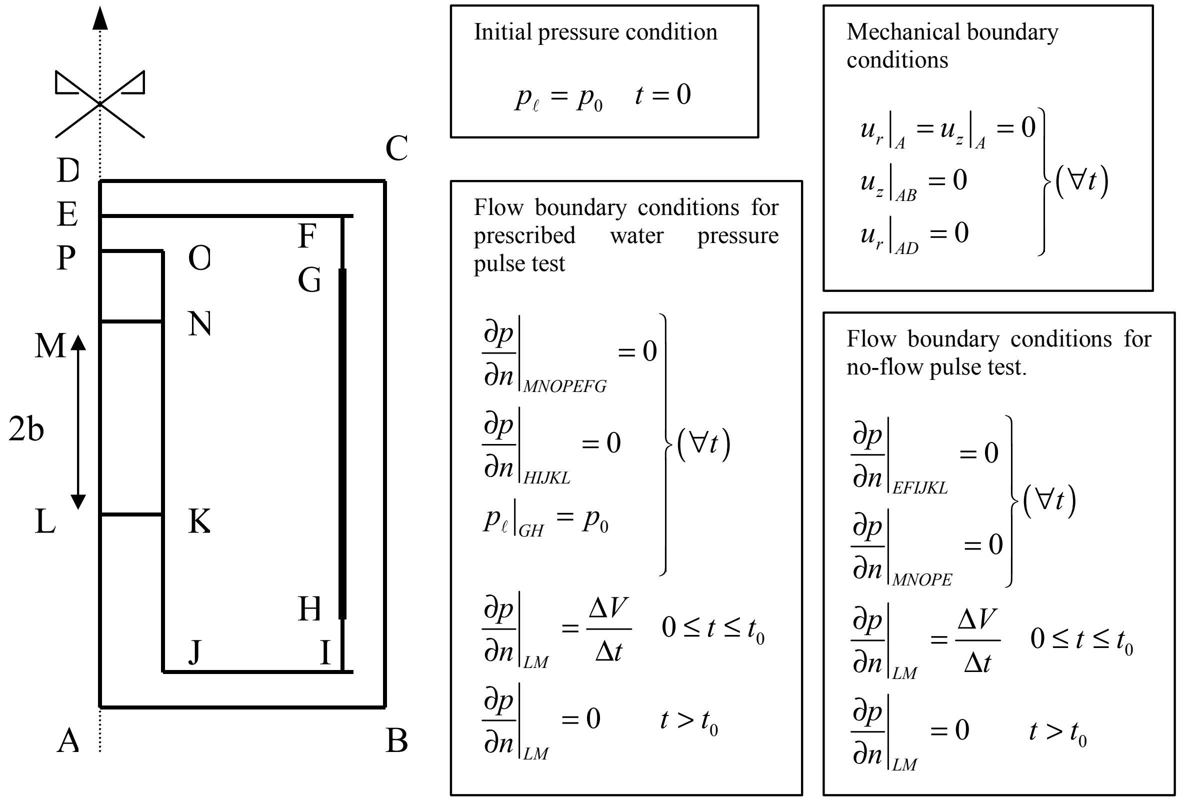

Initial pressure condition

$$p_\ell = p_0 \quad t = 0$$

Flow boundary conditions for prescribed water pressure pulse test

$$\left.\begin{aligned} &\left.\frac{\partial p}{\partial n}\right|_{MNOPEFG} = 0 \\ &\left.\frac{\partial p}{\partial n}\right|_{HIJKL} = 0 \\ &\left.p_\ell\right|_{GH} = p_0 \end{aligned}\right\}(\forall t)$$

$$\left.\frac{\partial p}{\partial n}\right|_{LM} = \frac{\Delta V}{\Delta t} \quad 0 \le t \le t_0$$

$$\left.\frac{\partial p}{\partial n}\right|_{LM} = 0 \quad t > t_0$$

Mechanical boundary conditions

$$\left.\begin{aligned} &u_r|_A = u_z|_A = 0 \\ &u_z|_{AB} = 0 \\ &u_r|_{AD} = 0 \end{aligned}\right\}(\forall t)$$

Flow boundary conditions for no-flow pulse test.

$$\left.\begin{aligned} &\left.\frac{\partial p}{\partial n}\right|_{EFIJKL} = 0 \\ &\left.\frac{\partial p}{\partial n}\right|_{MNOPE} = 0 \end{aligned}\right\}(\forall t)$$

$$\left.\frac{\partial p}{\partial n}\right|_{LM} = \frac{\Delta V}{\Delta t} \quad 0 \le t \le t_0$$

$$\left.\frac{\partial p}{\partial n}\right|_{LM} = 0 \quad t > t_0$$

Figure 4.31: Mechanical and flow boundary conditions in both kind of pulse tests.

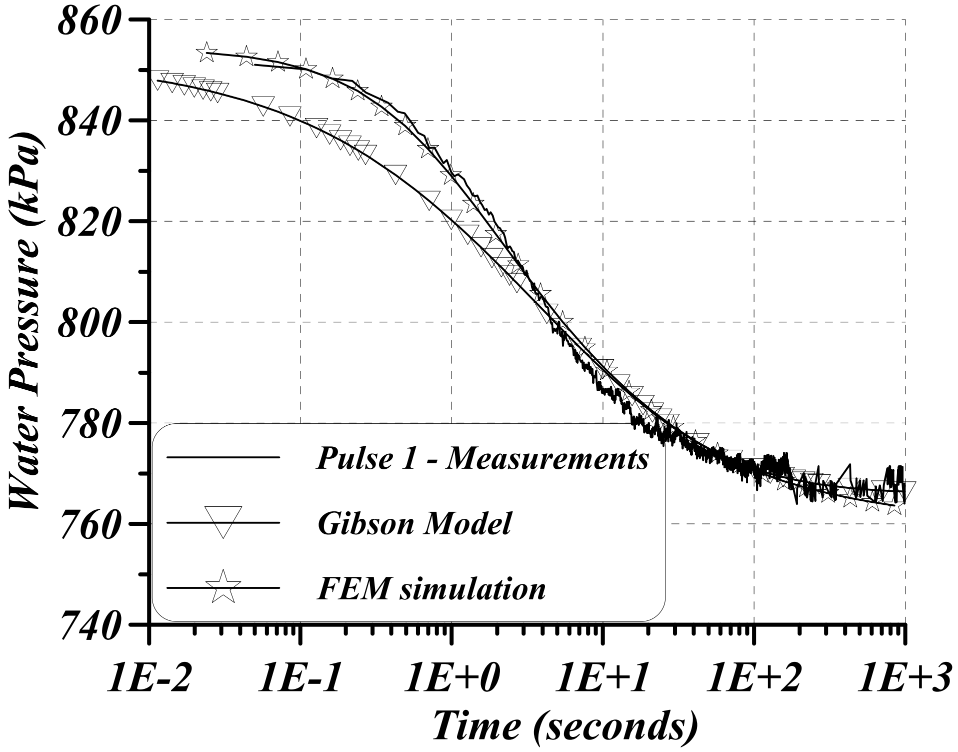

Figure 4.32: Comparison of the numerical simulation of the pulse number 1 and the pulse measured.

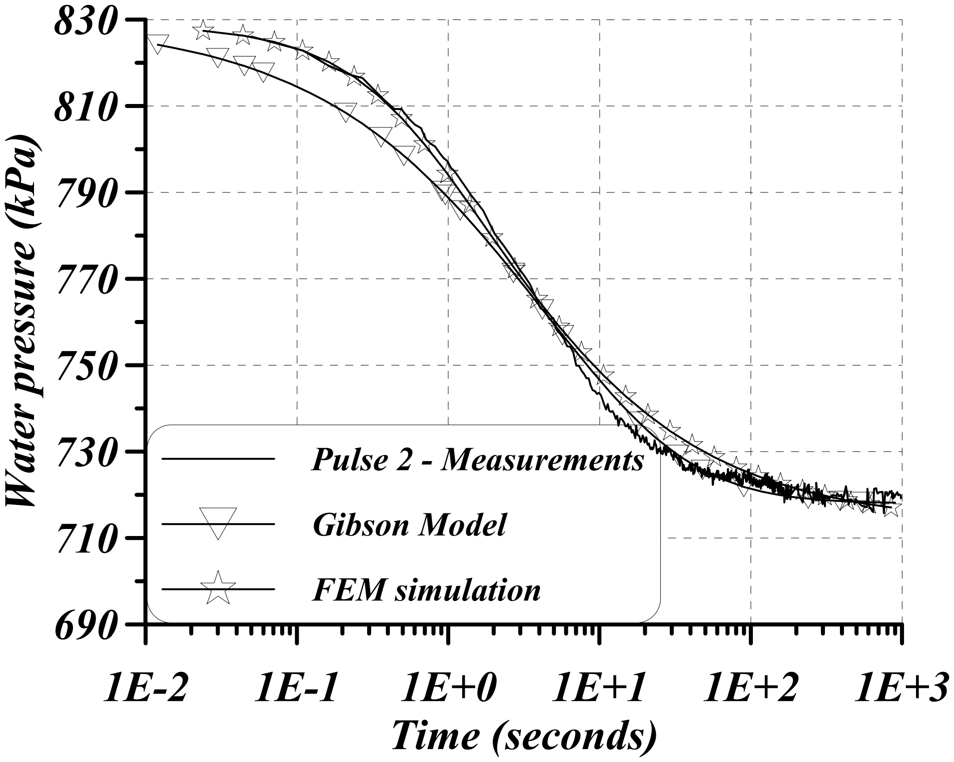

Figure 4.33: Comparison of the numerical simulation of the pulse number 2 and the pulse measured.

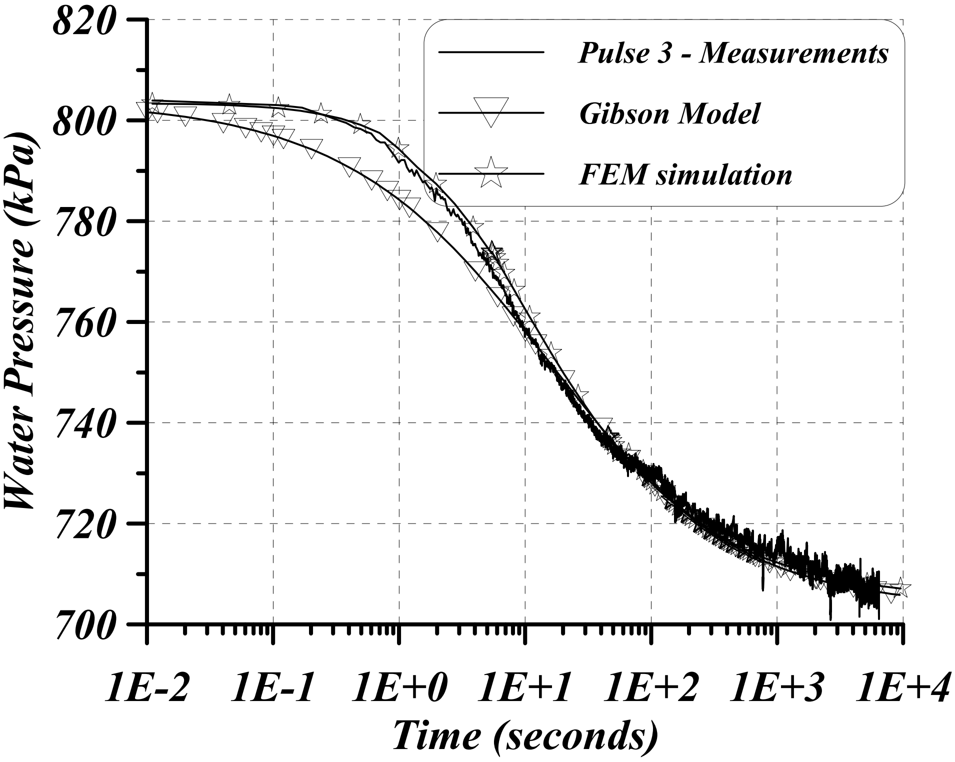

Figure 4.34: Comparison of the numerical simulation of the pulse number 3 and the pulse measured.

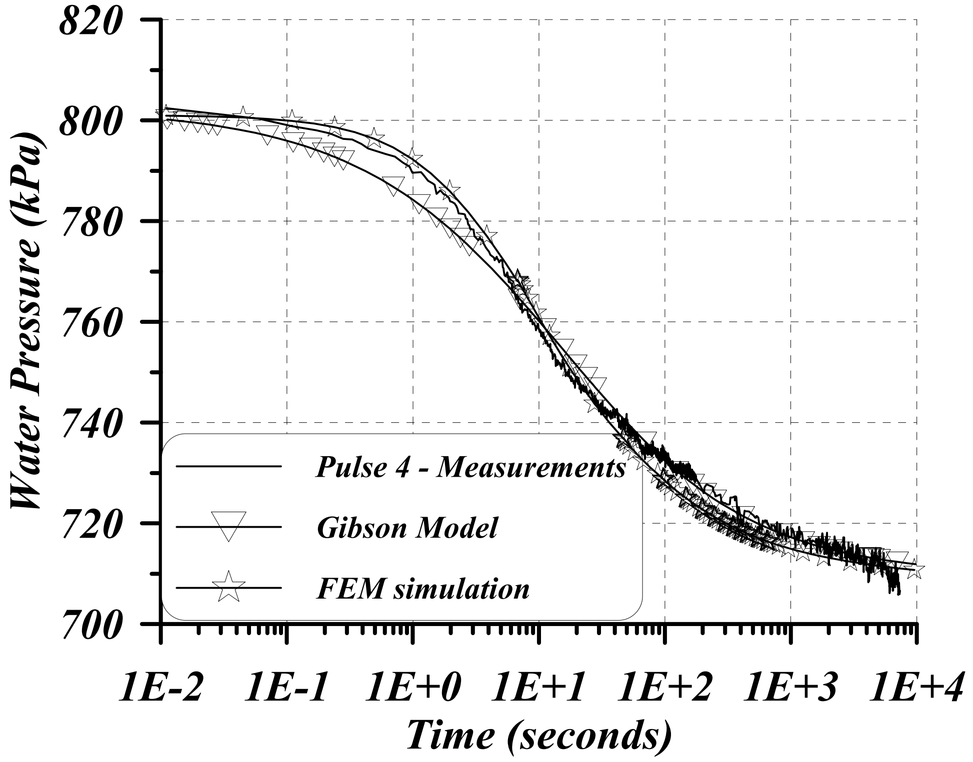

Figure 4.35: Comparison of the numerical simulation of the pulse number 4 and the pulse measured.

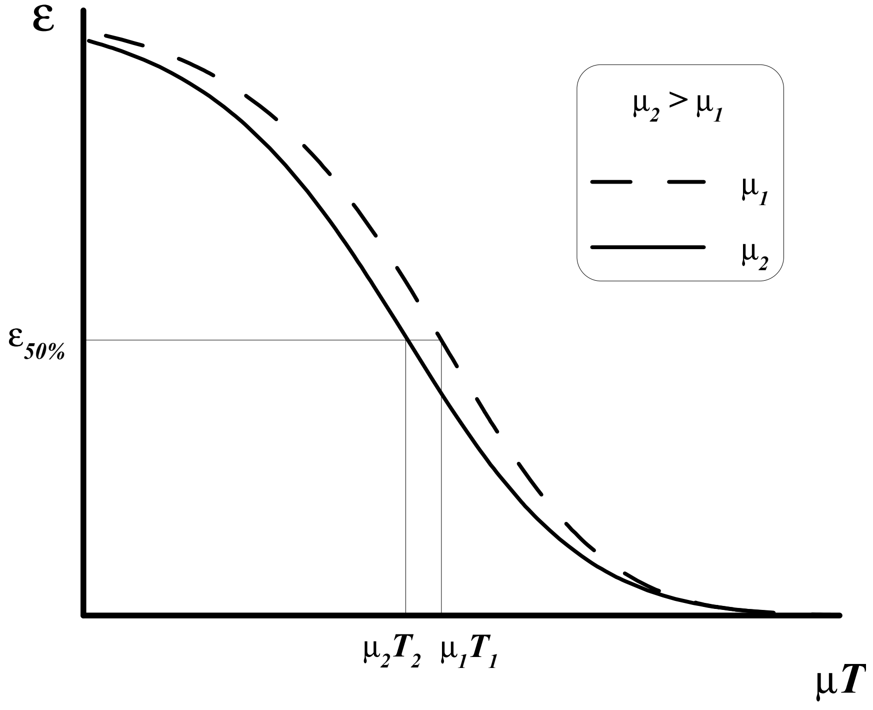

Figure 4.36: Analytical proof of the influence of the amount of water when back-analysing parameters. Gibson's solutions are used to qualitatively explain the influence of leakages or erroneous water volume measurements.

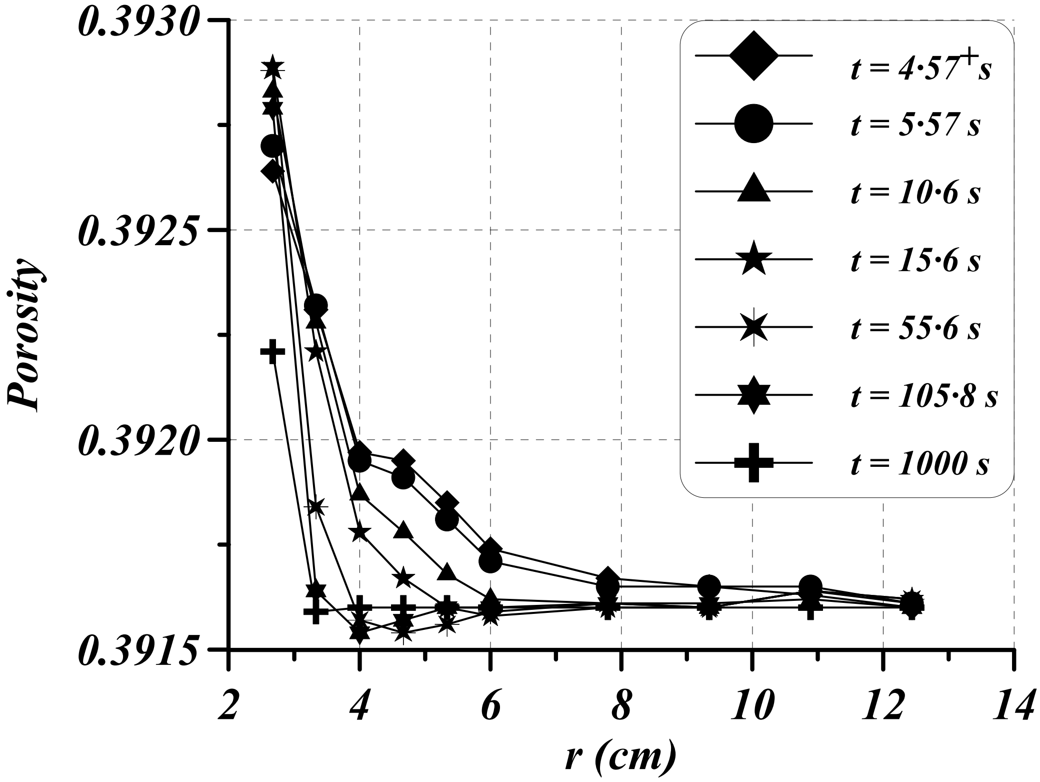

Figure 4.37: Porosity distribution at various times for pulse number 3 (prescribed water pressure boundary condition). The GDS pressure system required 4.57 seconds to increase the water pressure within the mini-piezometer.

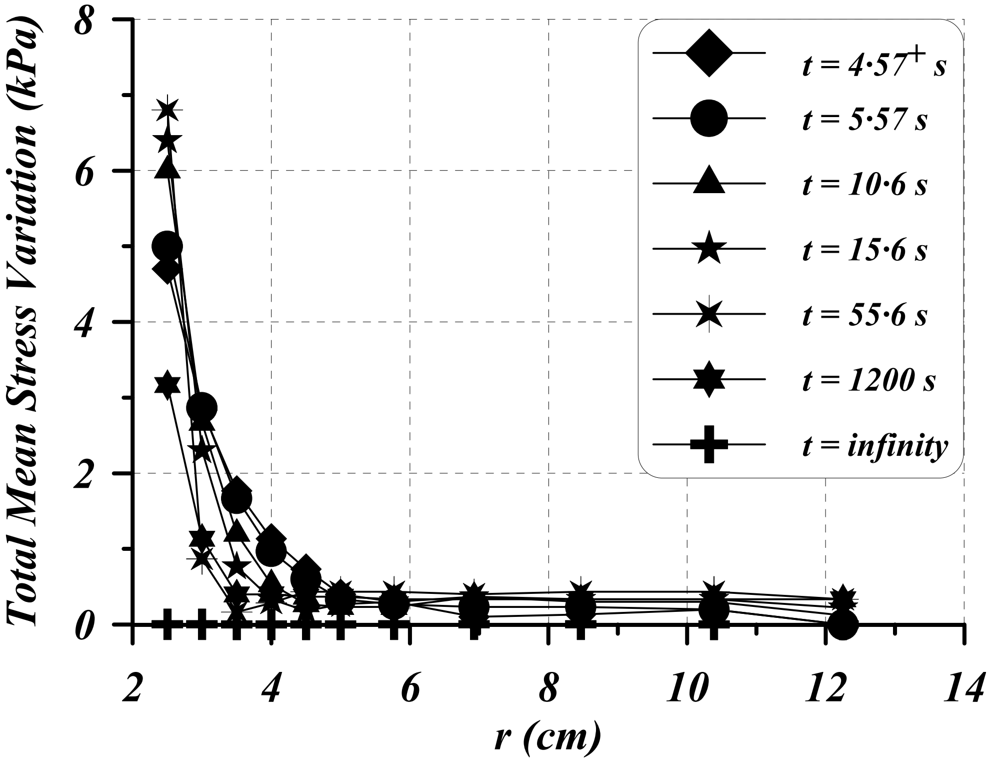

Figure 4.38: Total mean stress distribution at various times for pulse number 3 (prescribed water pressure boundary condition).

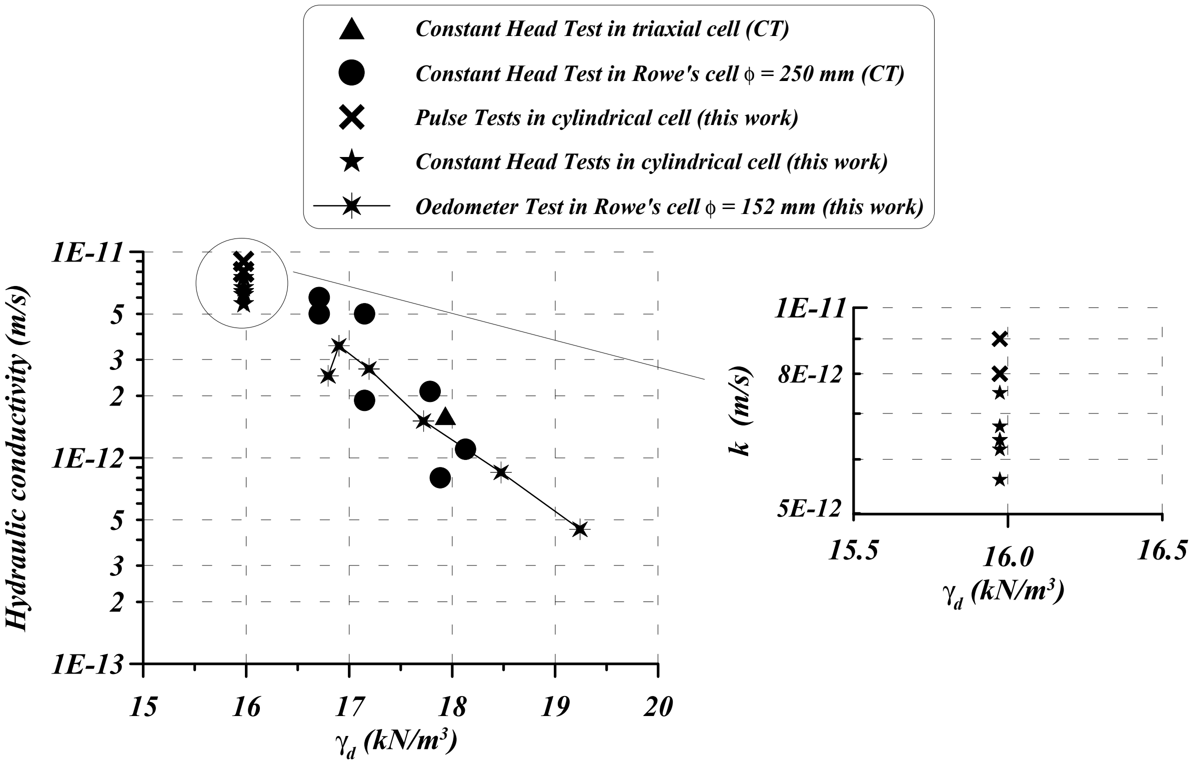

Figure 4.39: Summary of the obtained hydraulic conductivities by means of the three different experimental methods used in this work. Data provided by Clay Technology (CT) has been added to complete this figure (Börgesson et al, 1996; Johannesson et al, 1999).

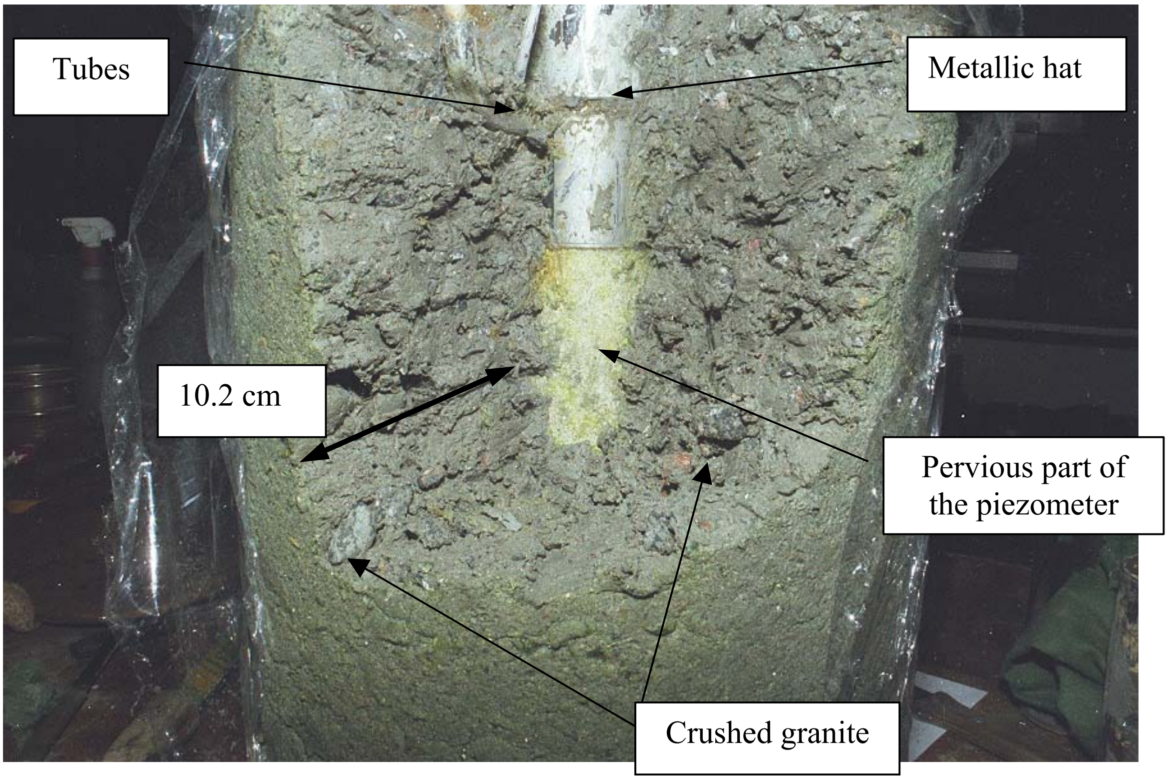

Figure 4.40: Picture of the mini-piezometer within the backfill specimen. It can be seen the large particles of granite. A metallic hat is placed on the mini-piezometer in order to protect it while compacting the backfill.

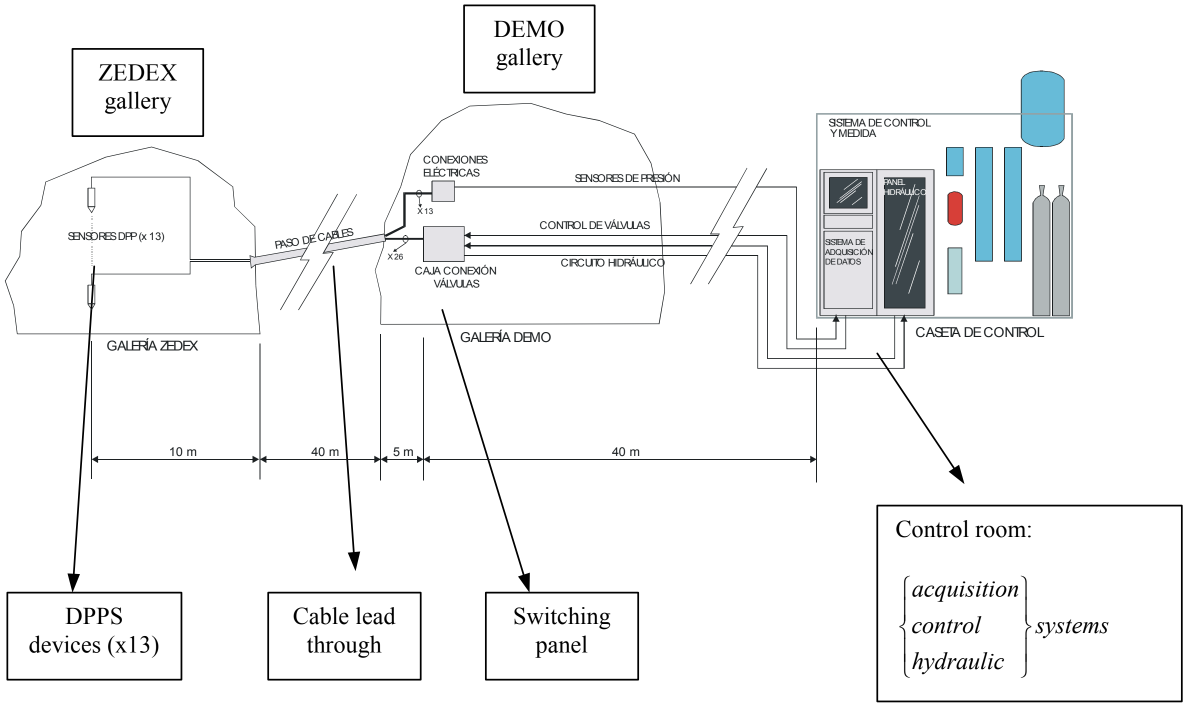

Figure 4.41: General layout installed by AITEMIN to perform pulse tests in the ZEDEX gallery (AITEMIN, 1999).

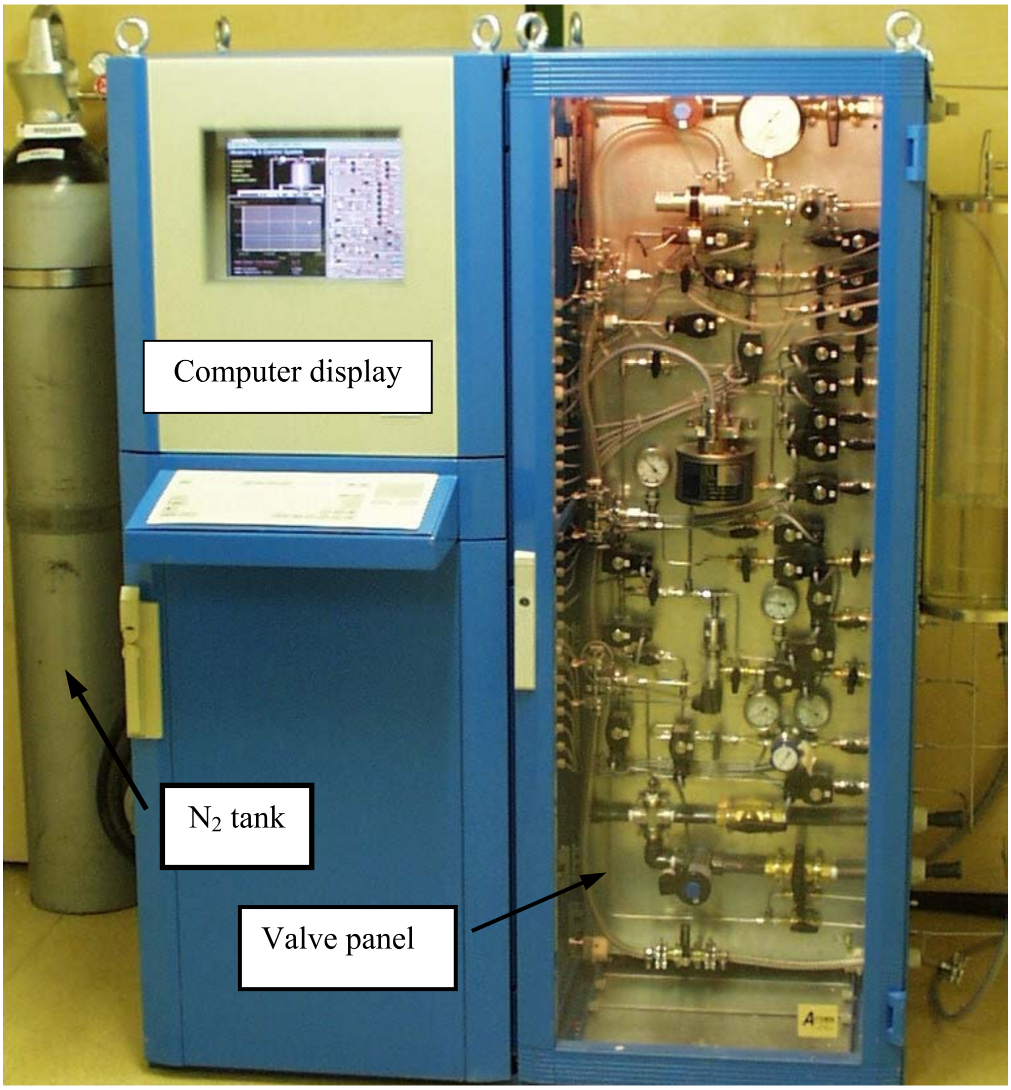

Figure 4.42: Acquisition and control system of the thirteen mini-piezometers and all the valves involved in the layout (AITEMIN, 1999). This system is placed within the control office managed by Clay Technology at the third level of the Äspö HRL.

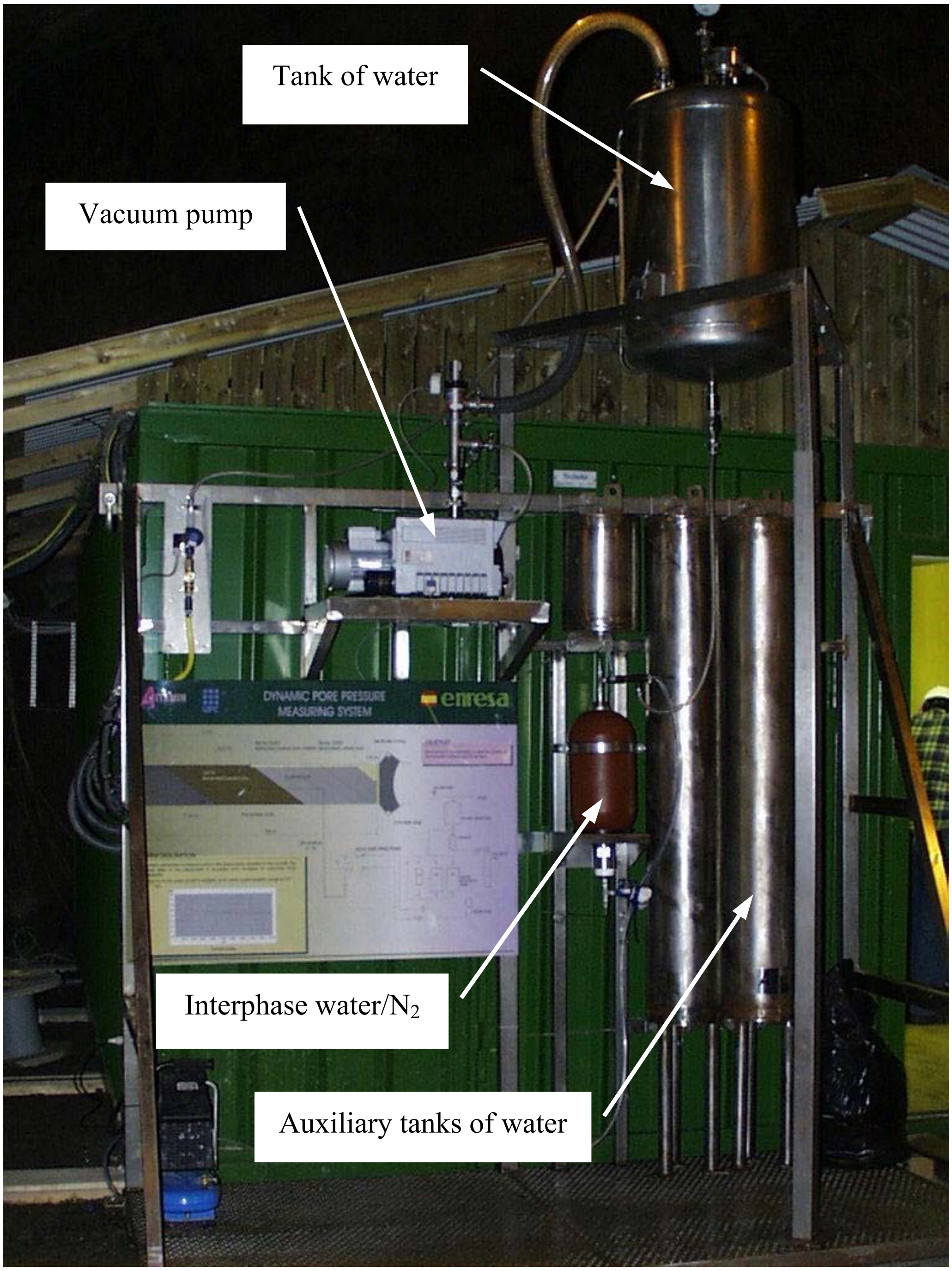

Figure 4.43: External part of the control system of the mini-piezometers (AITEMIN, 1999).

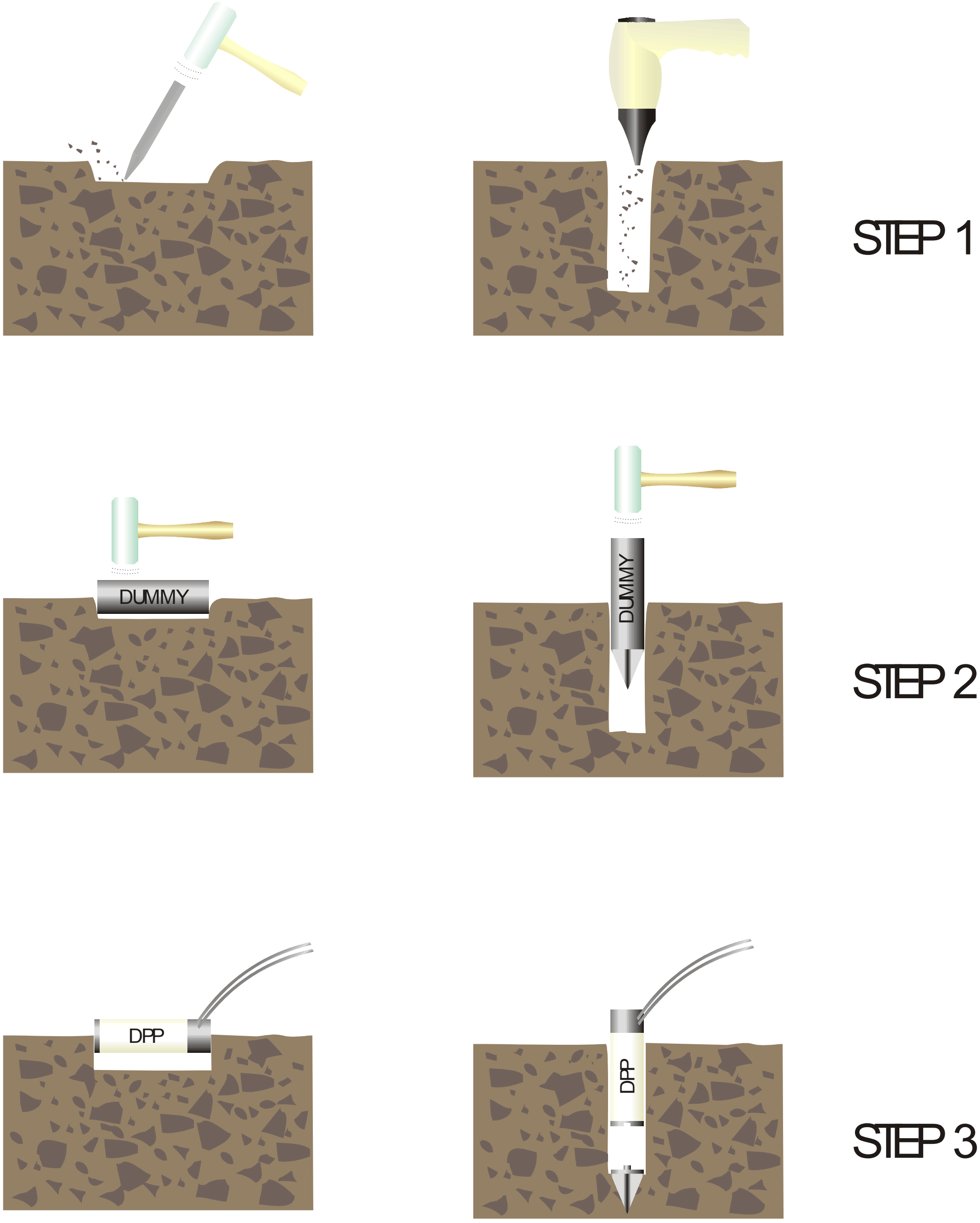

Figure 4.44: Detail of the process of DPPS installation in the backfill. A dummy was used to create the hole for the DPPS when backfill was compacted (AITEMIN, 1999).

Figure 4.45: Detail of a DPPS placed perpendicularly to the layer (AITEMIN, 1999).

Figure 4.46: Detail of a DPPS placed in parallel with the layer (AITEMIN, 1999).

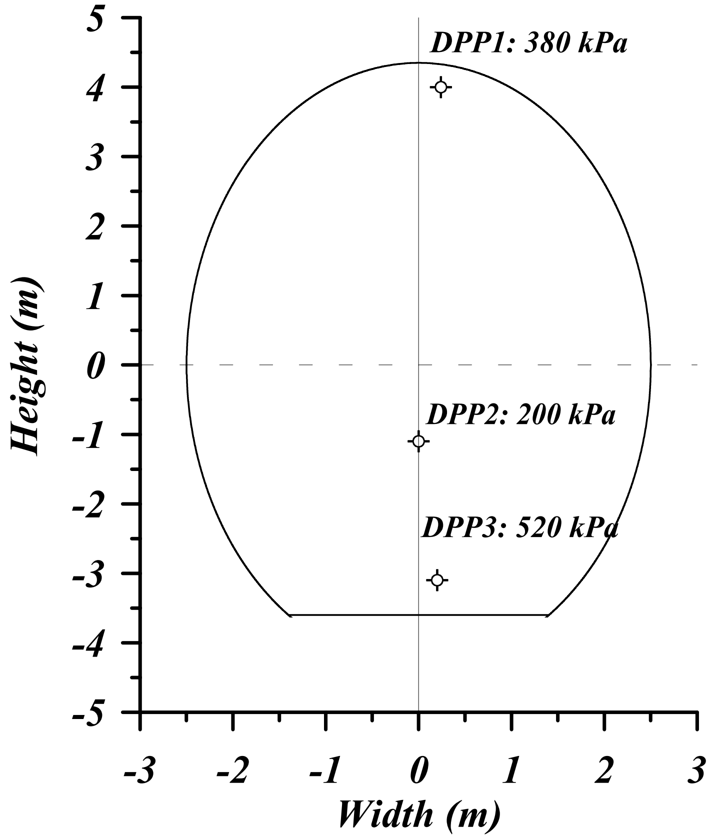

Figure 4.47 Distribution of relative water pressure at DPPS placed at layer 2 section A4. The measurements were performed in a pressure transducer located in the valve panel in the acquisition and control system (late March 2003).

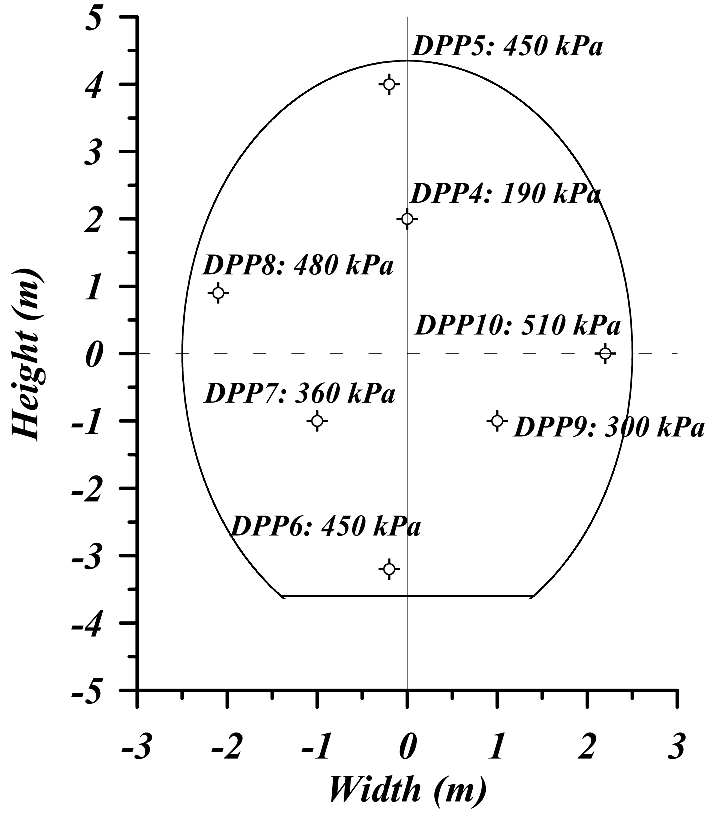

Figure 4.48: Distribution of relative water pressure at DPPS placed at layer 3 section A4. The measurements were performed in a pressure transducer located in the valve panel in the acquisition and control system (late March 2003).

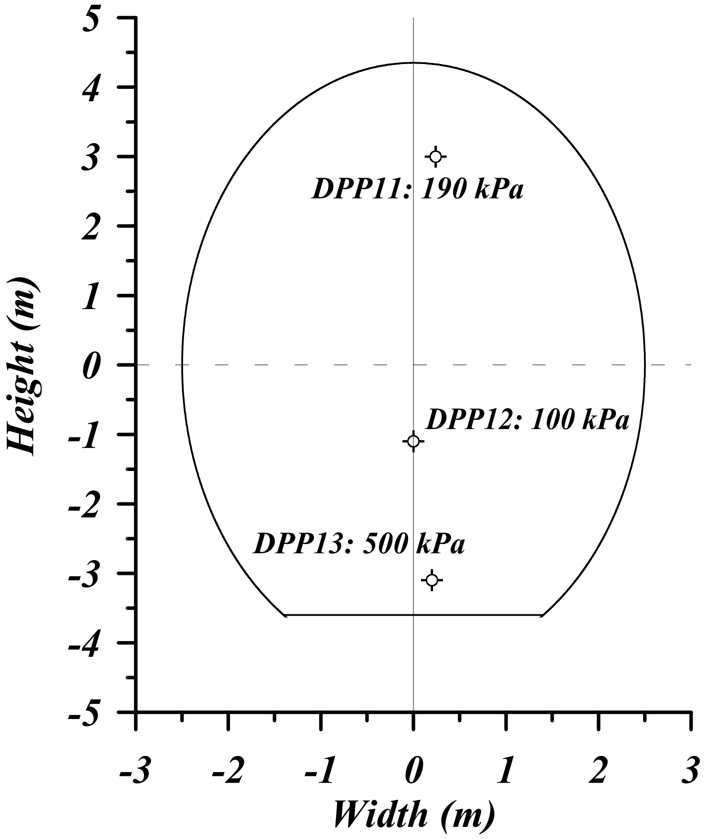

Figure 4.49: Distribution of relative water pressure at DPPS placed at layer 4 section A4. The measurements were performed in a pressure transducer located in the valve panel in the acquisition and control system (late March 2003).

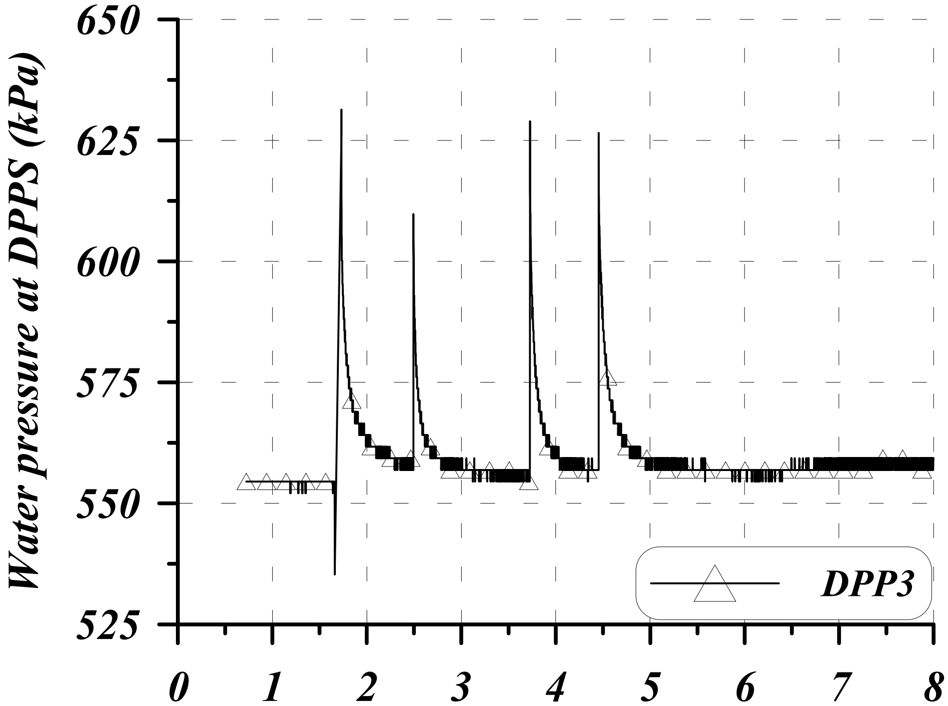

Figure 4.50: Evolution of water pressure at DPP3 during the campaign of pulse tests at late March. Four pulse tests were carried out in this sensor. The pulse simulated was the fourth one, which was carried out the 29th.

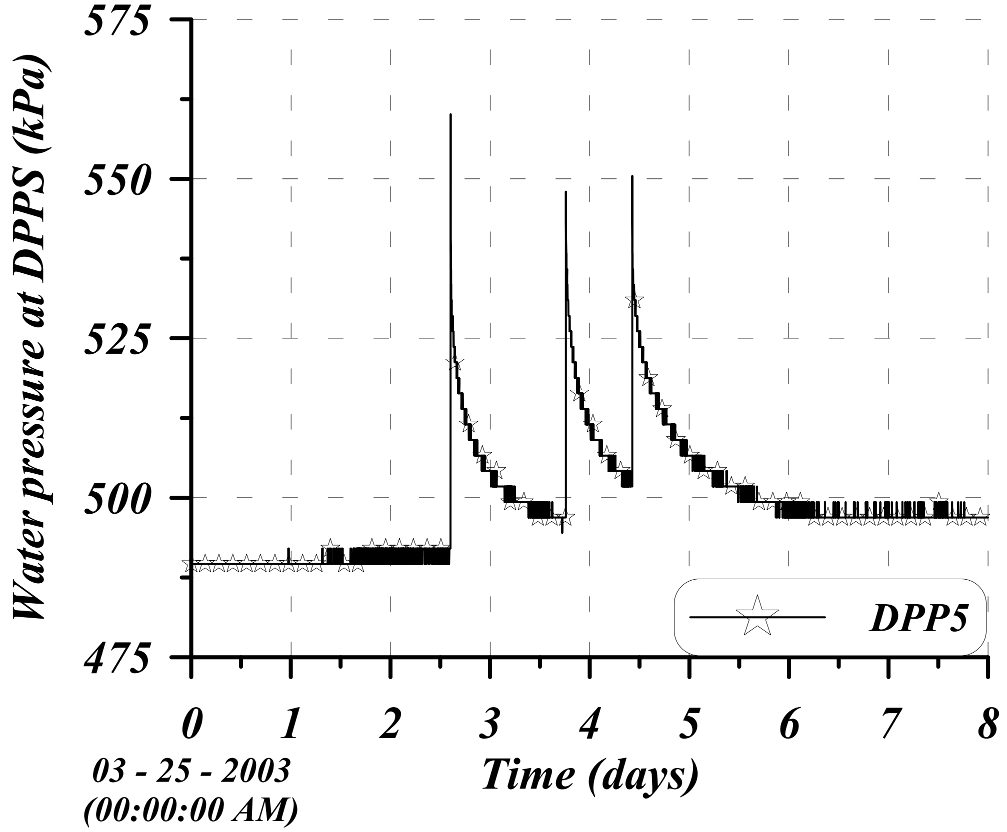

Figure 4.51: Evolution of water pressure at DPP5 during the campaign of pulse tests at late March. Three pulse tests were carried out, and the simulated one was the first one.

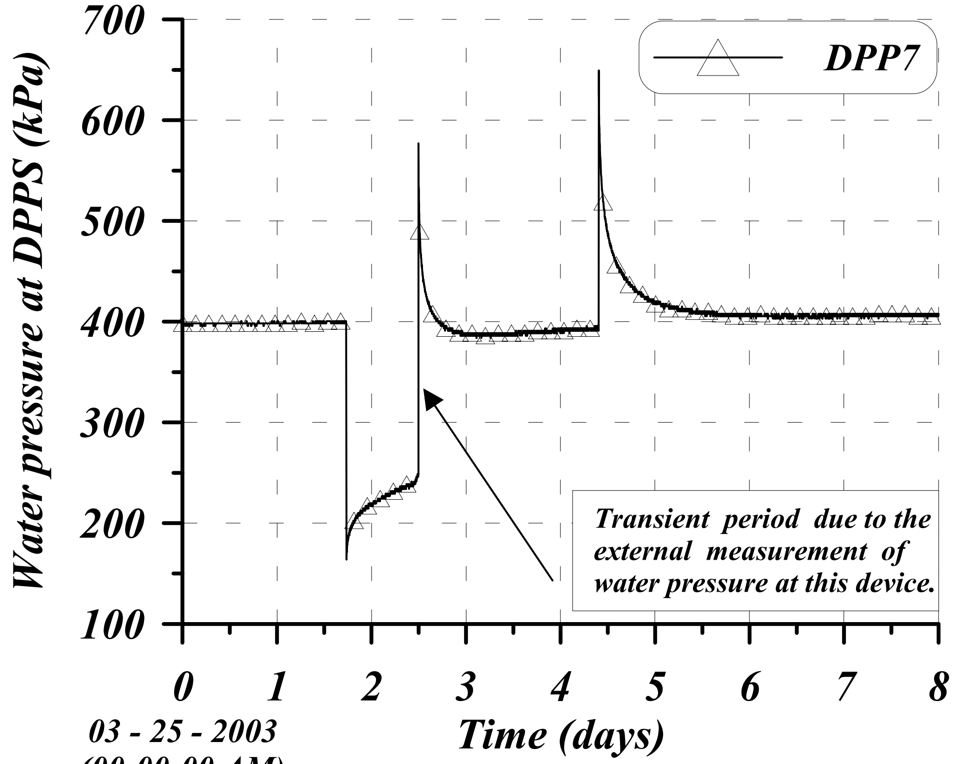

Figure 4.52: Evolution of water pressure at DPP7 during the campaign of pulse tests at late March. Two pulse tests were performed and the second pulse test was simulated as it started from steady conditions. The transient in the first pulse test makes difficult its numerical analysis.

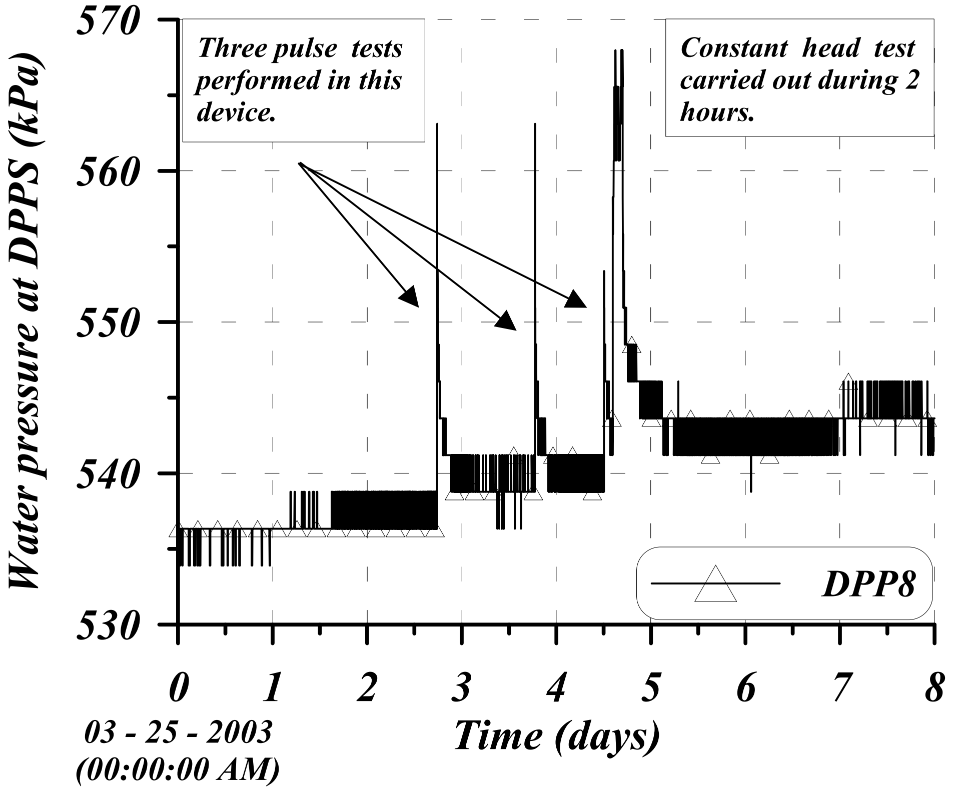

Figure 4.53: Evolution of water pressure at DPP8 during the campaign of pulse tests at late March. Three pulse tests were carried out in this sensor. It is clear that the accuracy of the transducer is around 5 kPa. The third pulse test is hard to notice. After three pulse tests in this device, a constant head test was performed. The first pulse test was numerically simulated.

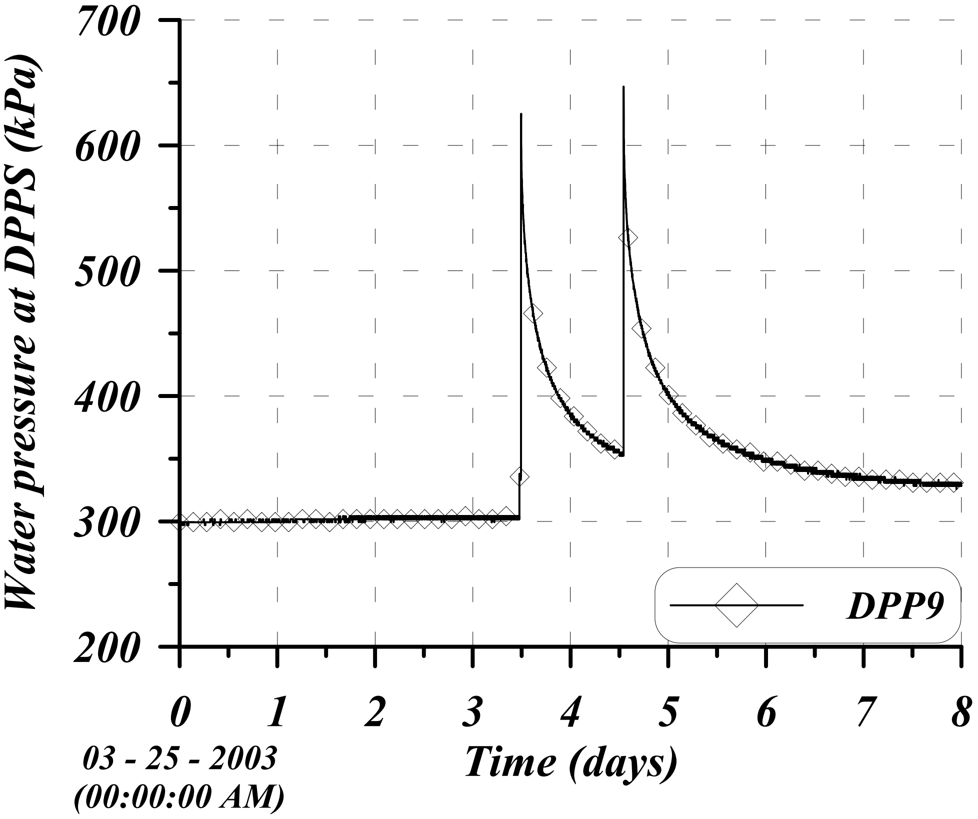

Figure 4.54: Evolution of water pressure at DPP9 during the campaign of pulse tests at late March. Two pulse tests were carried out in this sensor.

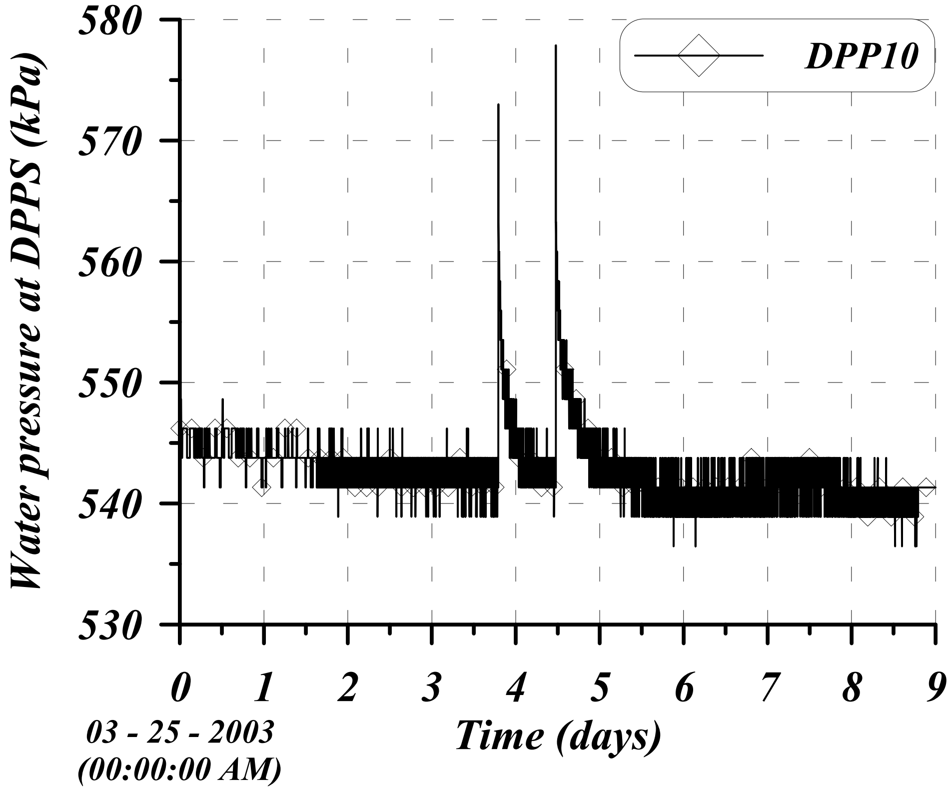

Figure 4.55: Evolution of water pressure at DPP10 during the campaign of pulse tests at late March. Two pulse tests were carried out in this sensor. The first one was numerically simulated.

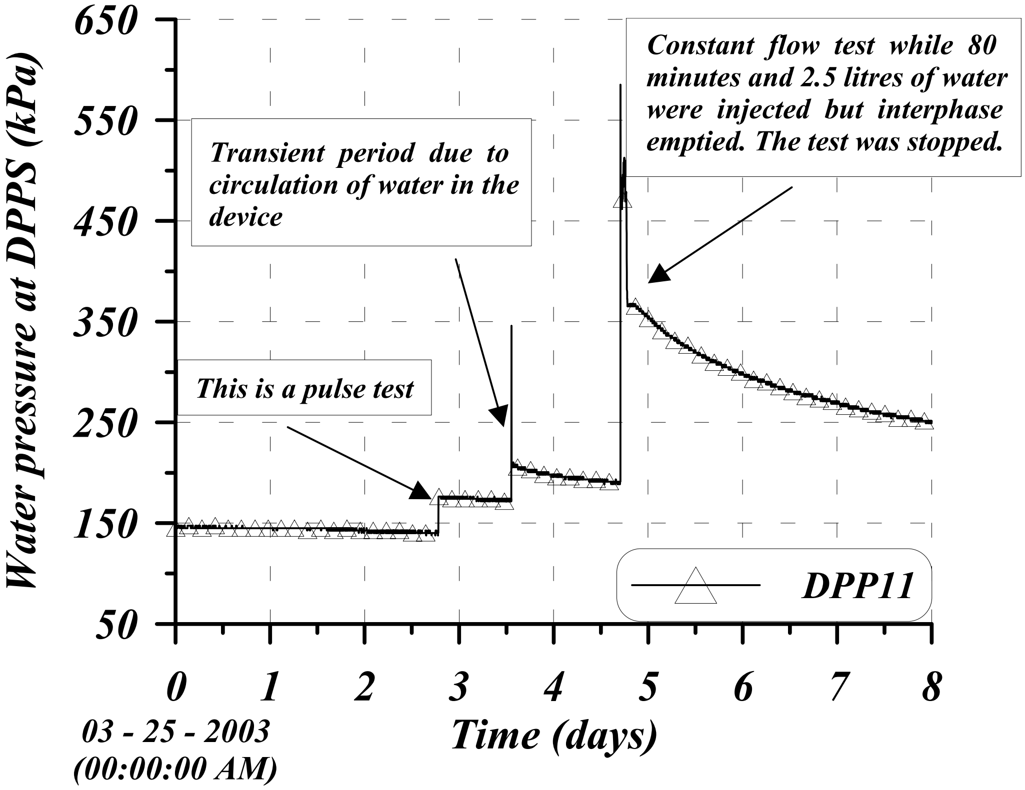

Figure 4.56: Evolution of water pressure at DPP11 during the campaign of pulse tests at late March. The pulse test performed on day 2.7 was not simulated.

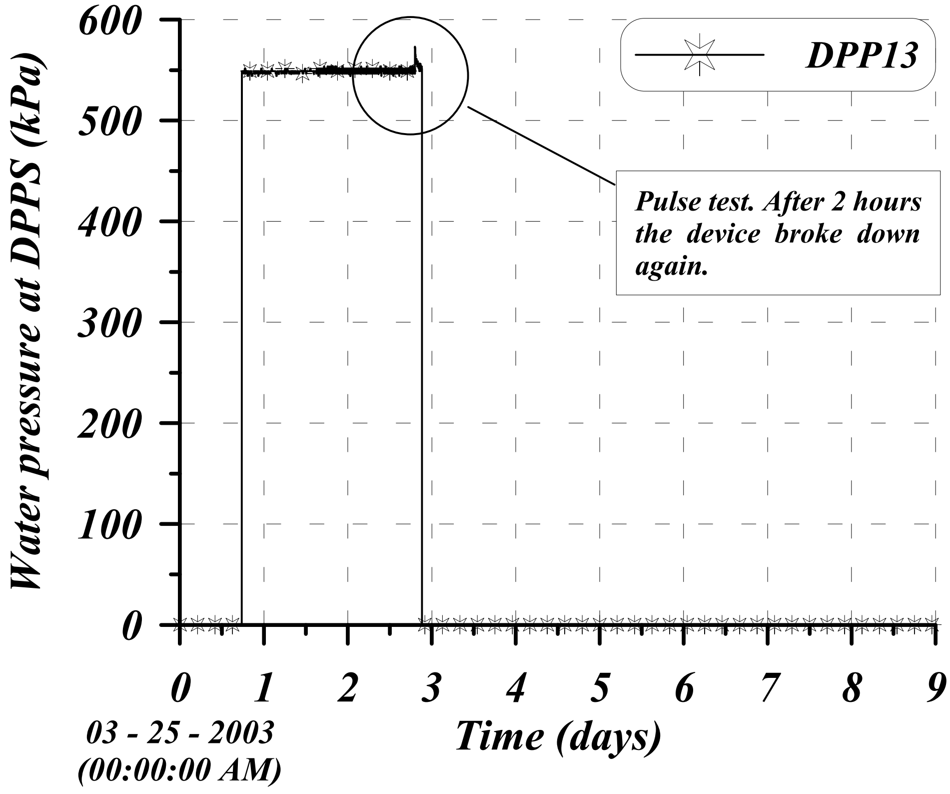

Figure 4.57: Evolution of water pressure at DPP11 during the campaign of pulse tests at late March. The pressure transducer broke down after two hours of the beginning of the pulse test on 27th.

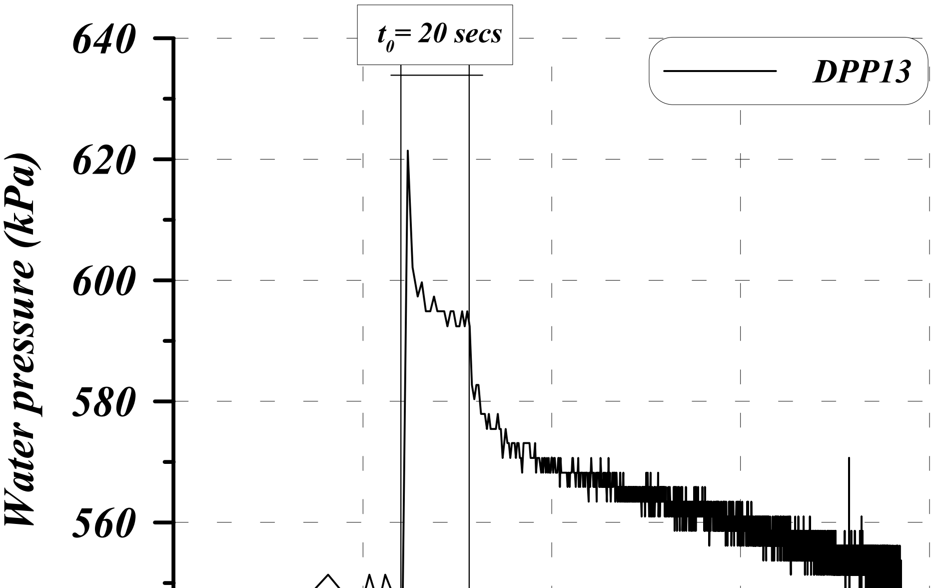

Figure 4.58: Zoom of the pulse test performed at DPP13. Water pressure increment within the mini-piezometer was very fast and water pressure was almost constant during the injection period (t_0 = 20”). After closing the valve, the dissipation process started. After 7000 seconds from the beginning of the pulse test the pressure transducer broke down.

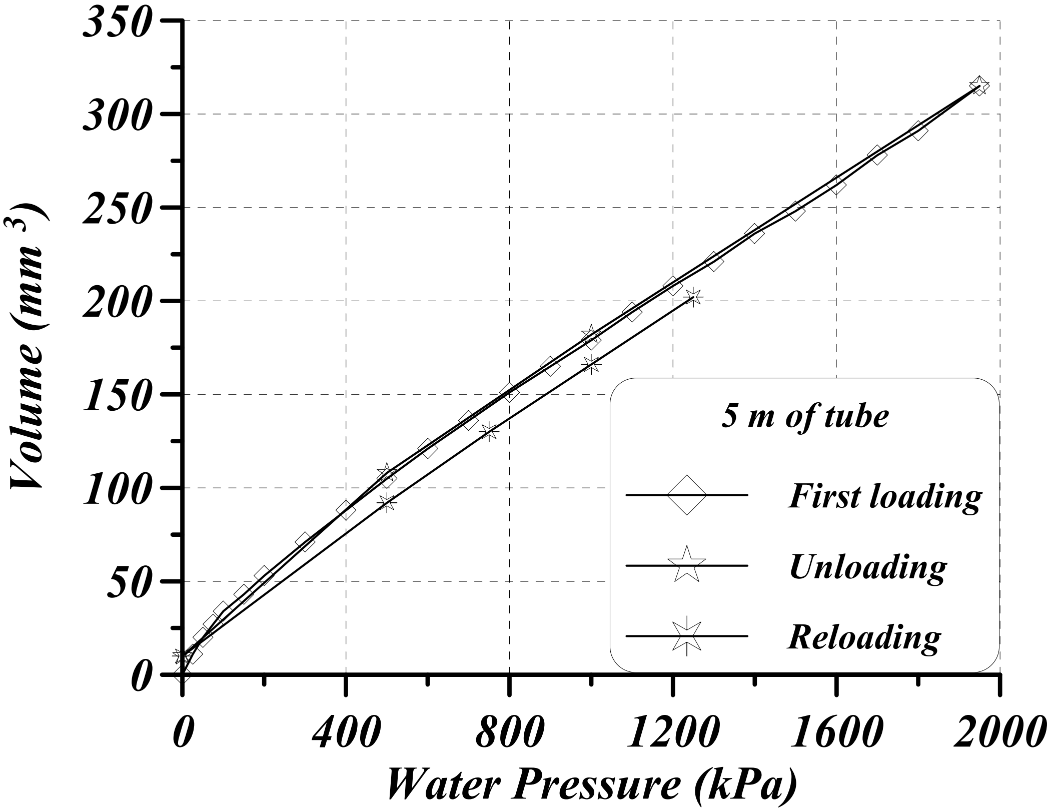

Figure 4.59: Experimental measurement of the flexibility of 5 meters of stainless steel. A first loading, unloading and a reloading were performed. The calibration was performed with a GDS system pressure. Deformation of GDS system and water within the GDS were subtracted from the measurements.

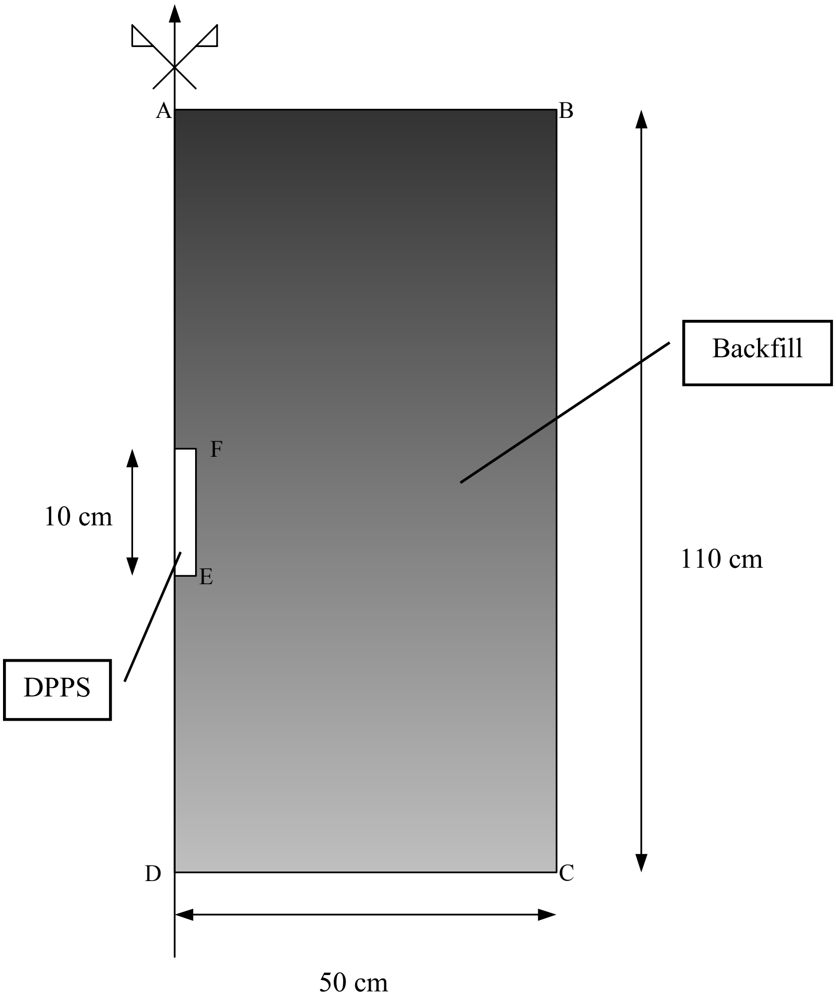

Mechanical boundary conditions (t > 0)

$$u_r\big|_D = u_z\big|_D = 0$$

$$u_r\big|_{AD} = 0$$

$$\sigma_z\big|_{AB} = -1MPa$$

$$\sigma_z\big|_{CD} = -1MPa$$

$$\sigma_r\big|_{BC} = -1MPa$$

Flow boundary conditions (t > 0)

$$\left.\frac{\partial p}{\partial n}\right|_{EF} = \frac{\Delta V_r}{t_0} \qquad 0 \le t \le t_0$$

$$\left.\frac{\partial p}{\partial n}\right|_{EF} = 0 \qquad t > t_0$$

$$p\big|_{AB} = p\big|_{BC} = p\big|_{CD} = p_0$$

Initial conditions (t = 0)

$$p\big|_{ABCDA} = p_0$$

$$u\big|_{ABCDA} = 0$$

$$\sigma = -\mathrm{Id} = \begin{bmatrix} -1 & 0 & 0 \\ 0 & -1 & 0 \\ 0 & 0 & -1 \end{bmatrix}$$

Figure 4.60: Geometry, boundary and initial conditions (both mechanical and flow) used in the numerical simulation of the in situ pulse tests by means of CODE_BRIGHT.

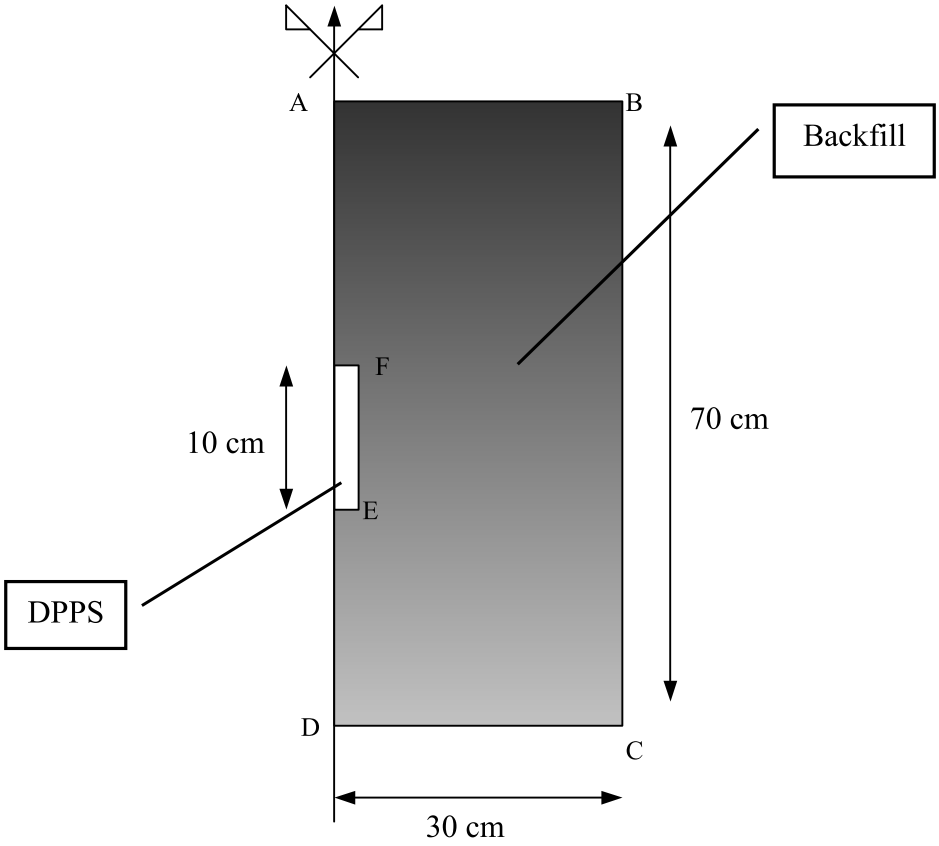

Figure 4.61: Geometry used in the simulation of in situ pulse tests of devices close to the rock. Mechanical and flow boundary conditions were the same as those presented in figure 4.60.

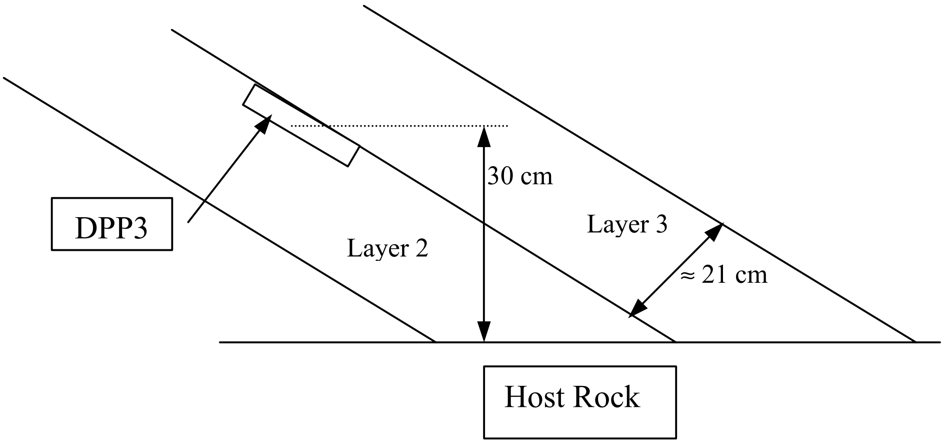

Figure 4.62: Location of DPP3 in layer 2 of section A4. It is relatively close to the host rock and its position is parallel to the face of the compacted layer.

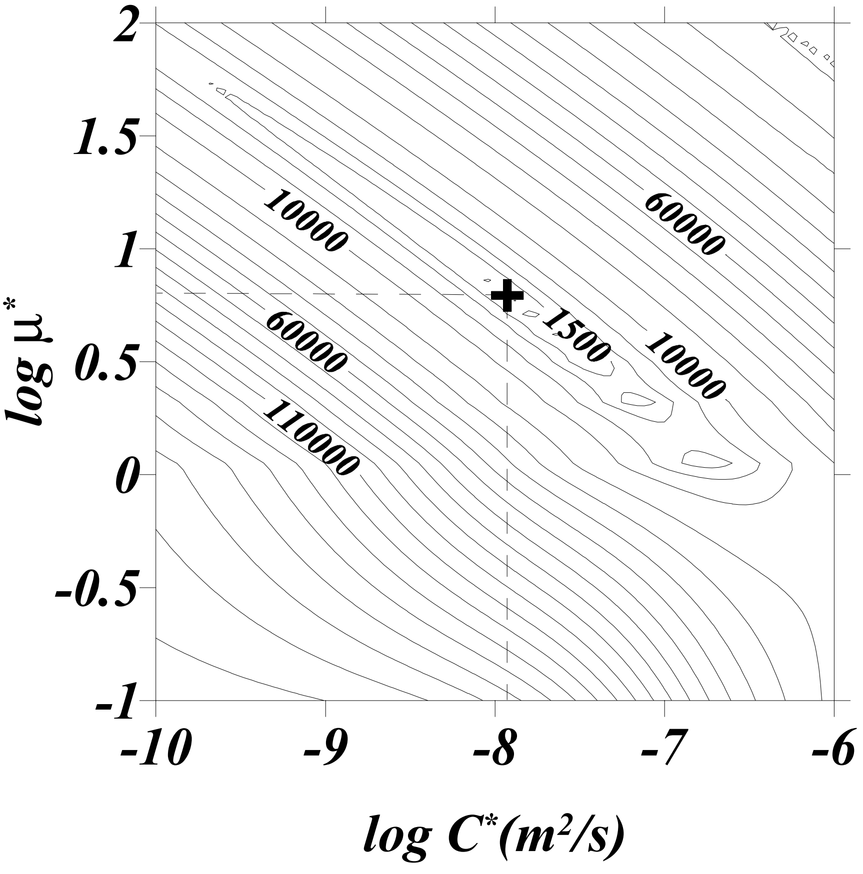

Figure 4.63: Contour map of the objective function, J, of pulse test performed in DPP3 by using the Gibson's model.

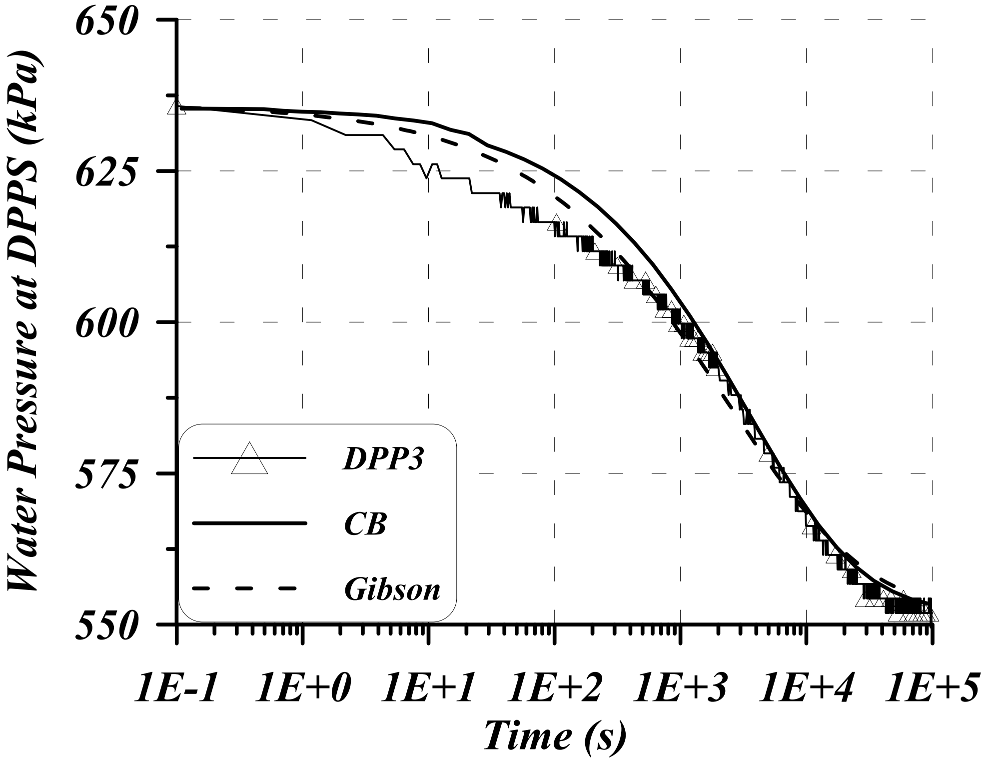

Figure 4.64: Pulse test performed in DPP3 and its comparison with the analytical solution by Gibson's model and the finite element simulation. Similarity between both solutions is evident, however, the parameters were slightly different among them.

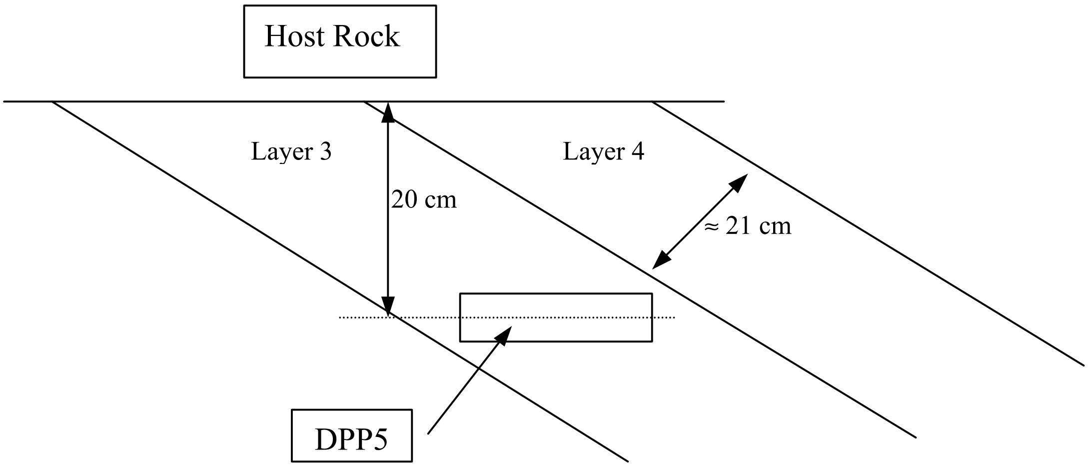

Figure 4.65: Location and position of sensor DPP5 close to the roof of layer 3 in section A4.

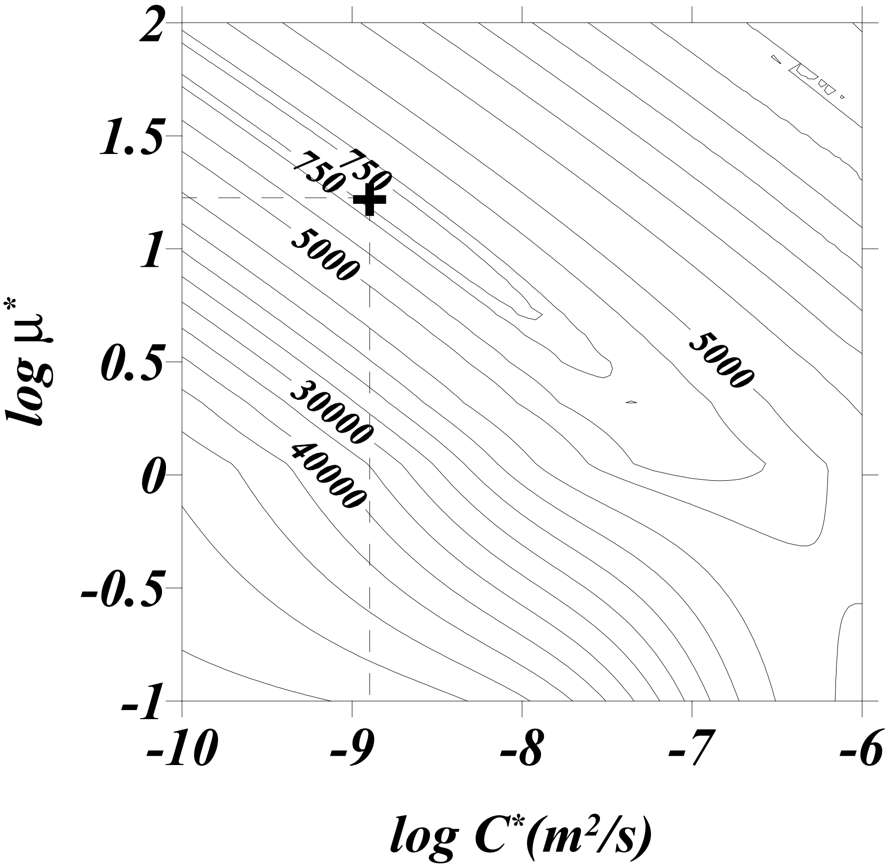

Figure 4.66: Contour map of the objective function, J, of pulse test performed in DPP5 by using the Gibson's model.

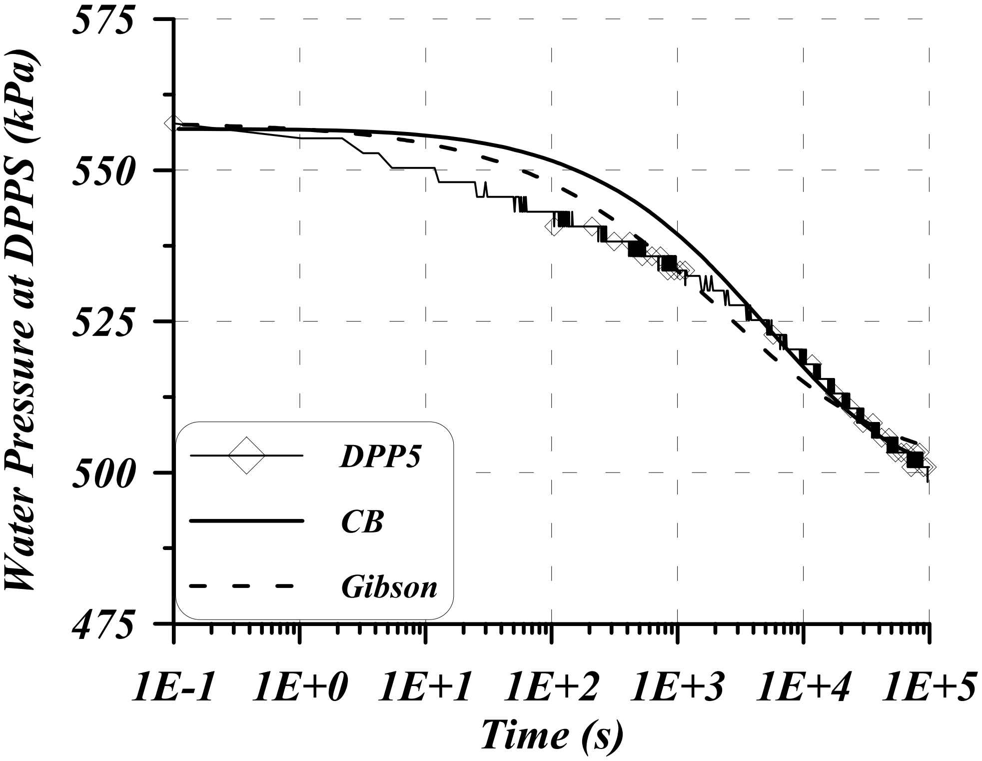

Figure 4.67: Pulse test performed in DPP5 and its comparison with the analytical solution by Gibson's model and the finite element simulation.

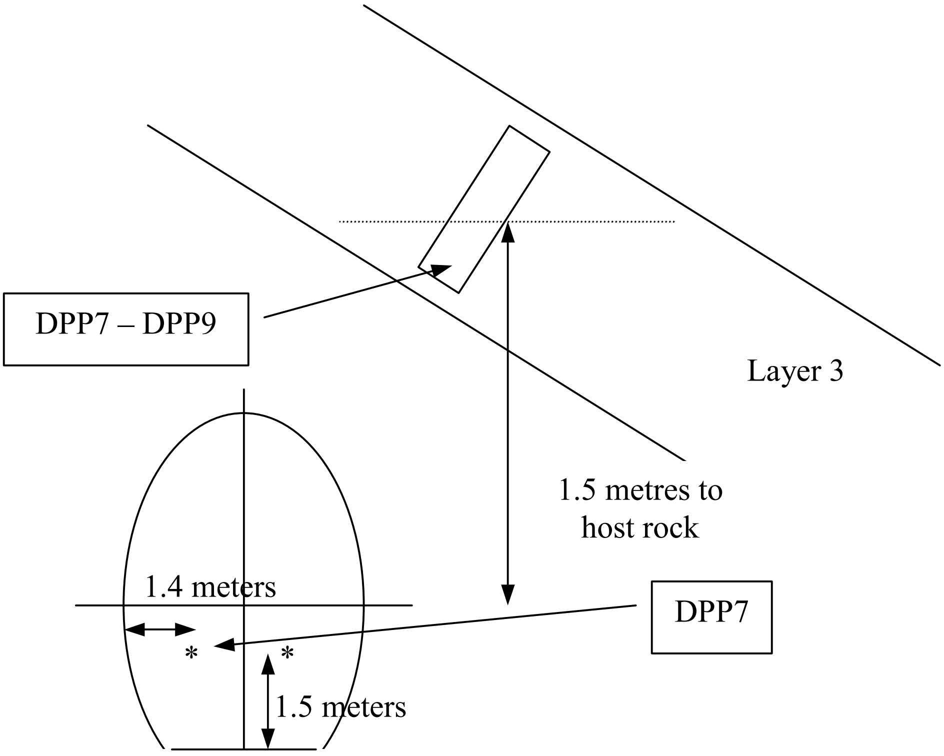

Figure 4.68: Location and position of sensors DPP7 and DPP9 close to the center of layer 3 in section A4.

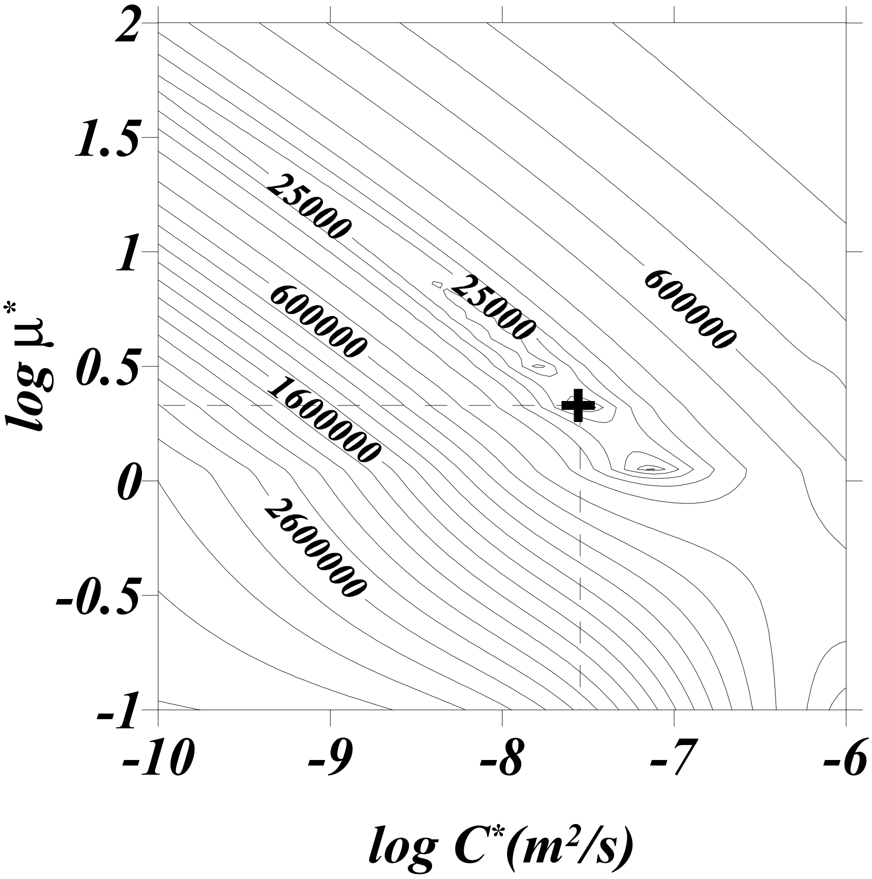

Figure 4.69: Contour map of the objective function, J, of pulse test performed in DPP7 by using the Gibson's model.

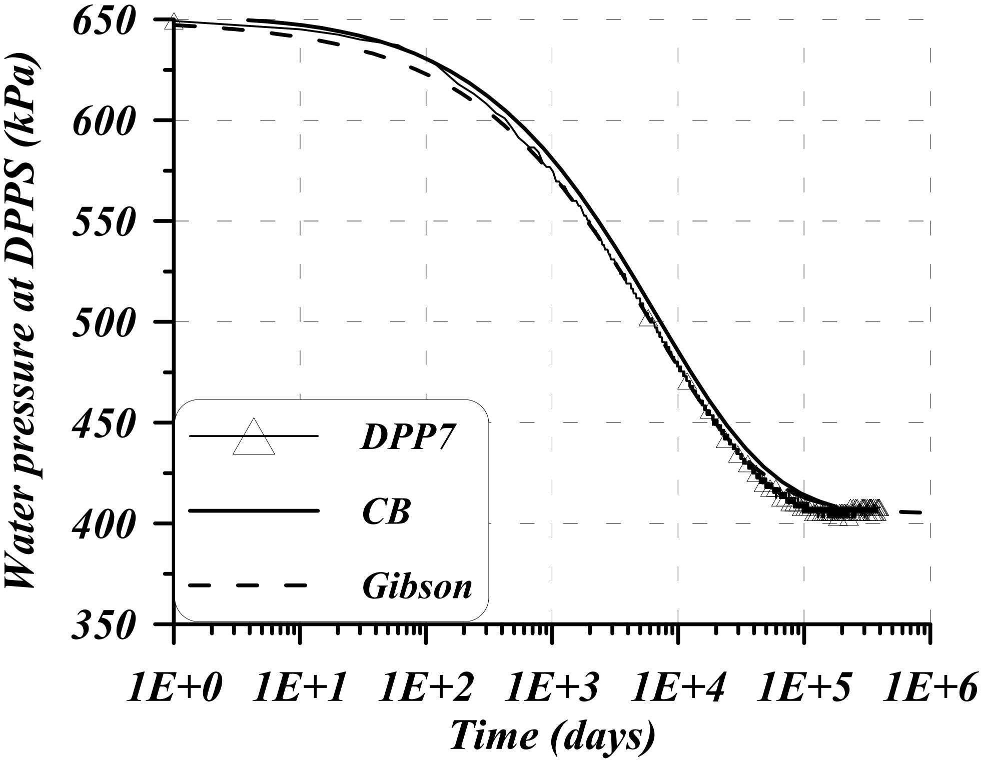

Figure 4.70: Pulse test performed in DPP7 and its comparison with the analytical solution by Gibson's model and the finite element simulation. Similarity between both solutions is good, obtained using similar parameters.

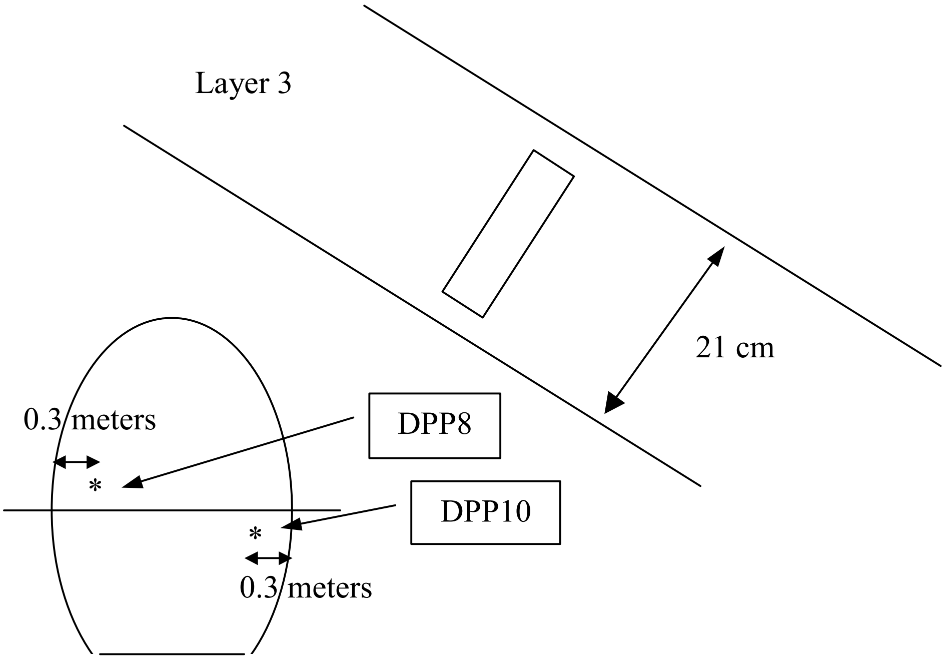

Figure 4.71: Location and position of sensors DPP8 and DPP10 close to the host rock at layer 3 in section A4.

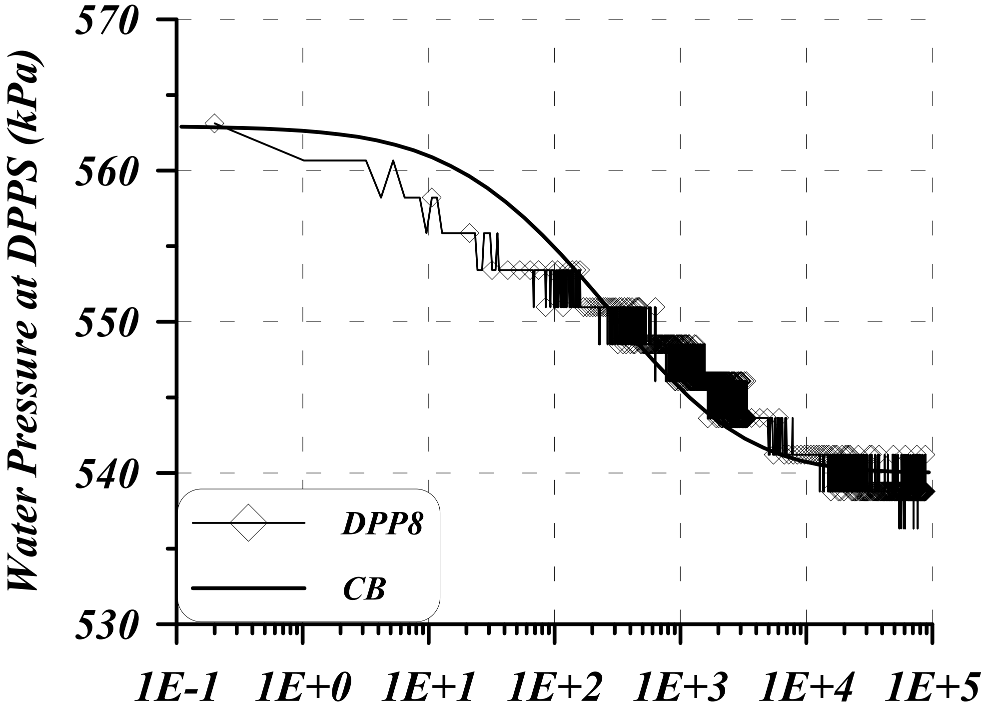

Figure 4.72: Comparison between the calculated dissipation process by means of the finite element code and the measured water pressure at sensor DPP8.

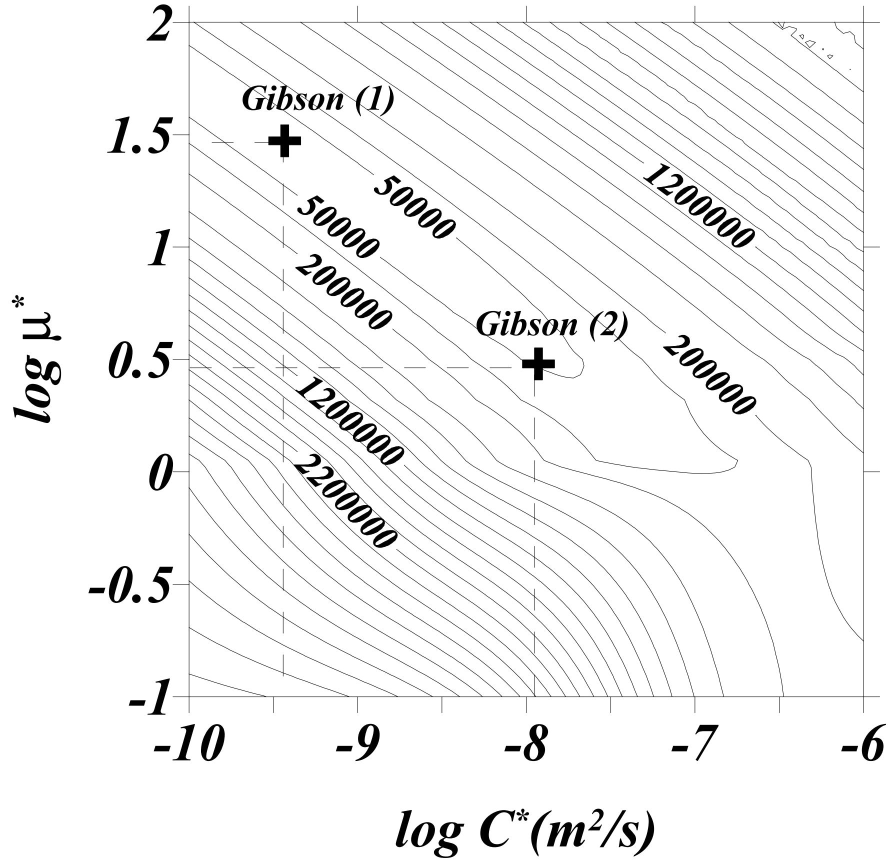

Figure 4.73: Contour map of the objective function, J, of pulse test performed in DPP9 by using the Gibson's model.

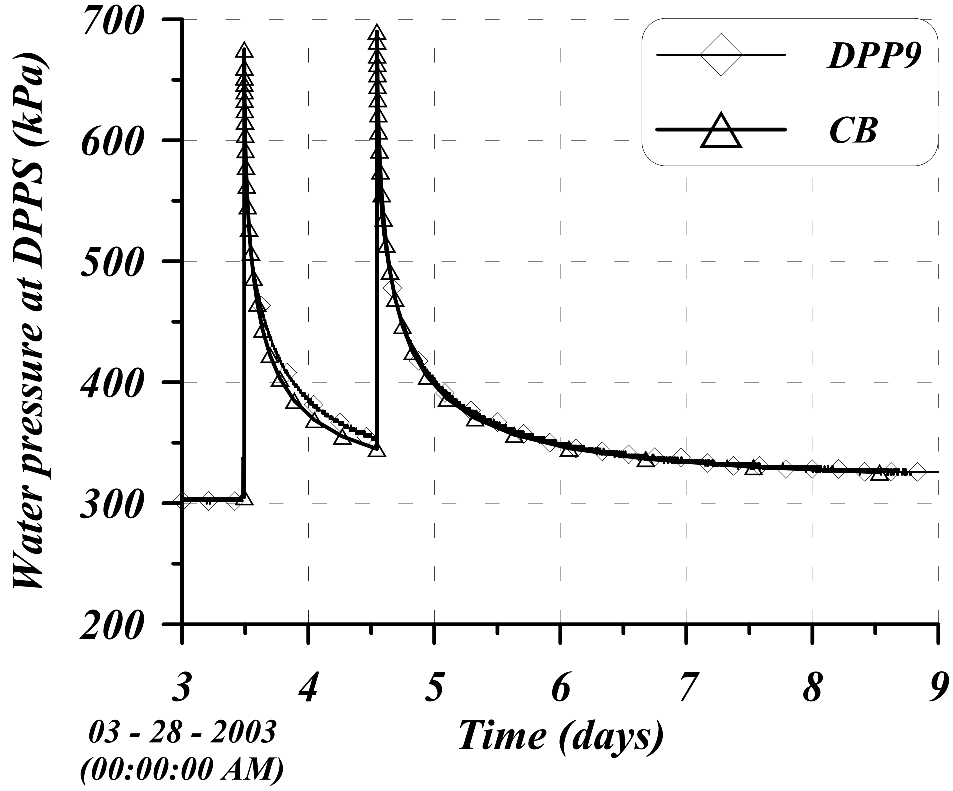

Figure 4.74: Comparison between the calculated dissipation process by means of the finite element code and the measured water pressure at sensor DPP9.

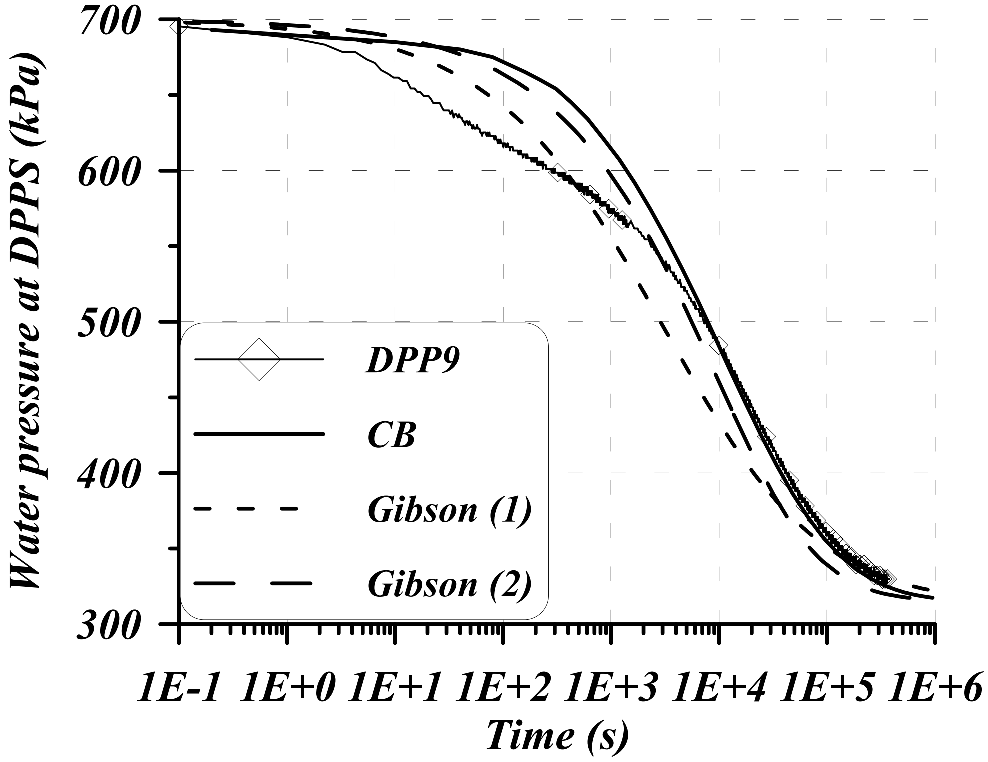

Figure 4.75: Detail of the second pulse test performed at sensor DPP9. It is clear that both models are not able to reproduce the beginning of the dissipation process.

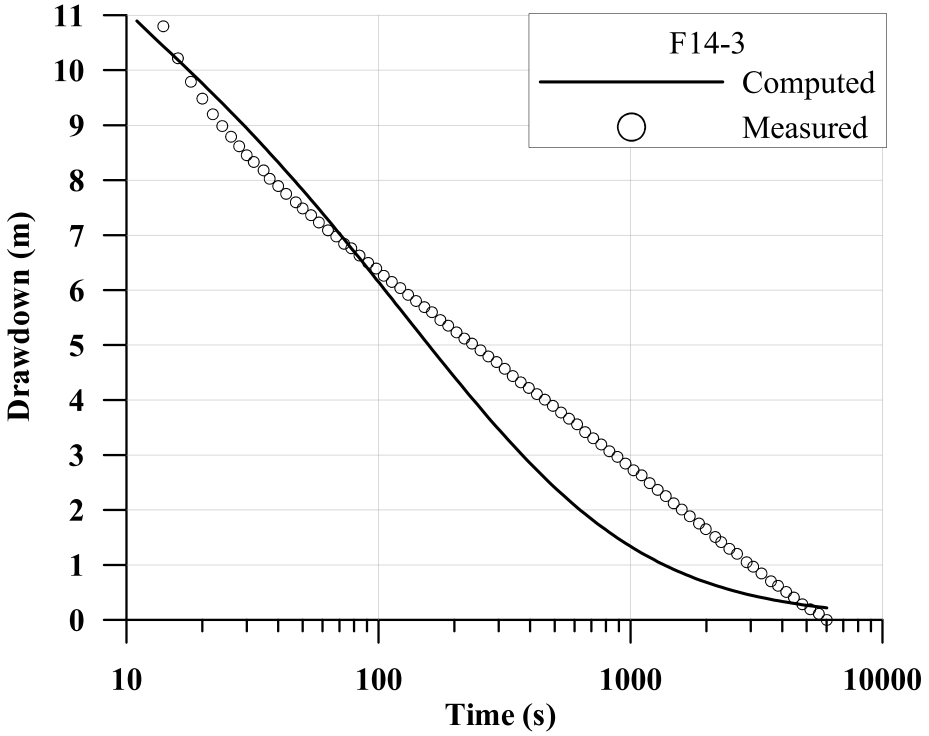

Figure 4.76: Results of a withdrawal pulse test performed in Grimsel (Switzerland) in the granitic host formation (Martínez-Landa et al. 2003). The measurements were compared with the analytical solution by Bredehoeft and Papadopulos (1980). It is clear that the evolution of the recovery of water pressure in the borehole does not follow the pattern of the model.

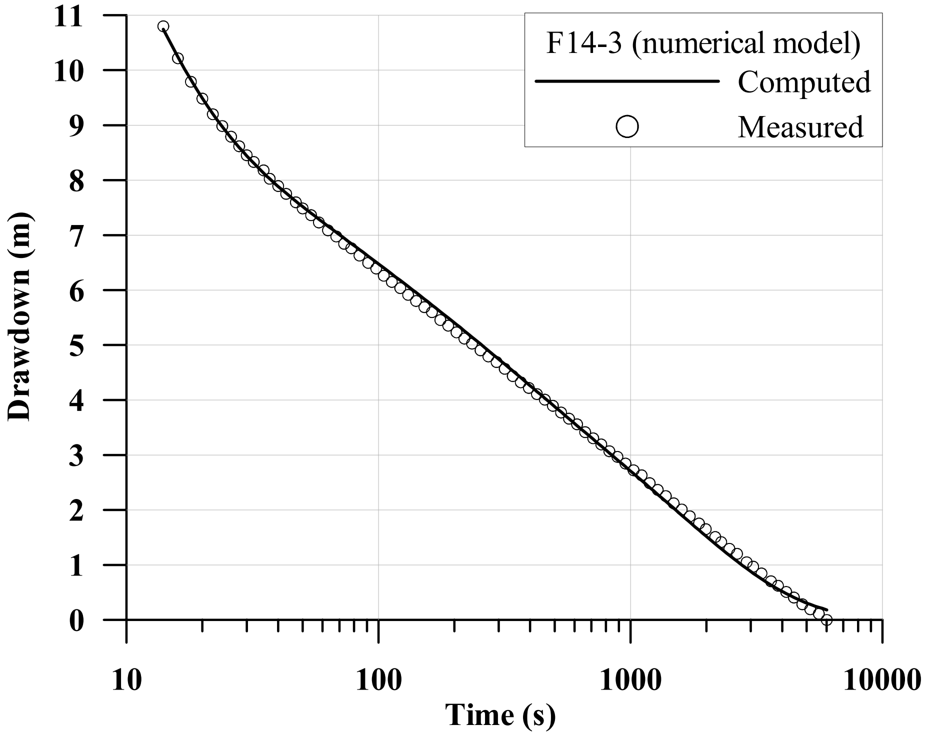

Figure 4.77: Comparison of the measurements of the withdrawal pulse test performed in Grimsel and a numerical flow model, which introduces the effect of a fracture (Martínez-Landa et al. 2003). By considering flow in fractured media, the dissipation process was properly reproduced.

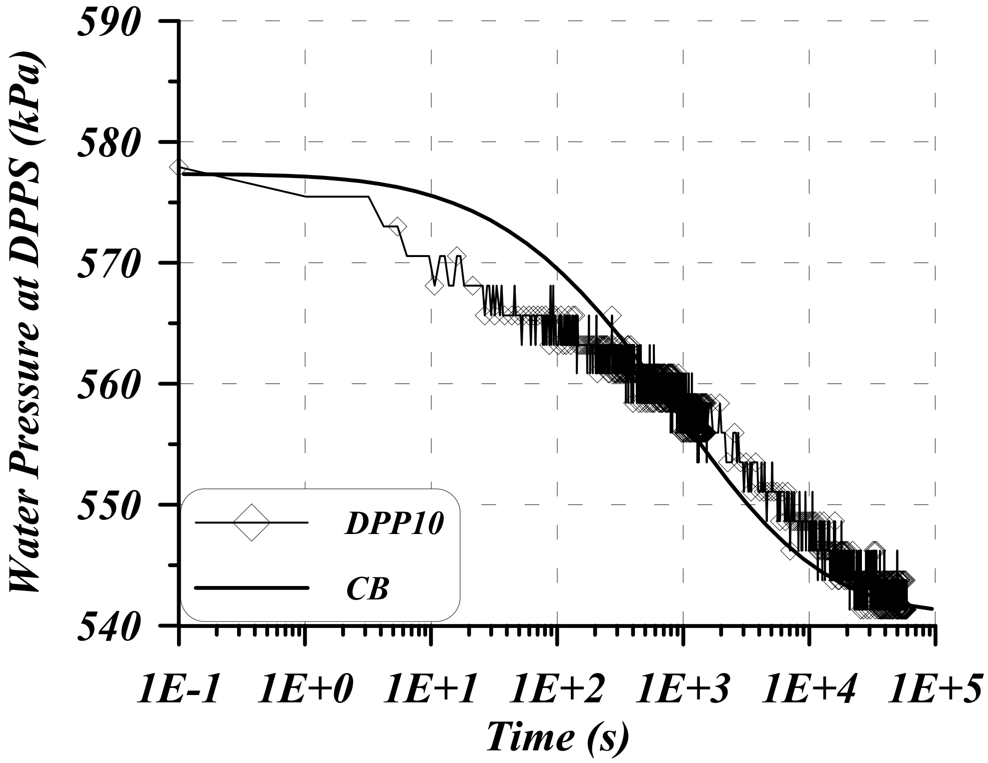

Figure 4.78: Comparison between the calculated dissipation process by means of the finite element code and the measured water pressure at sensor DPP10. Gibson's model was not applied to this pulse test due to the big error of the measurements.

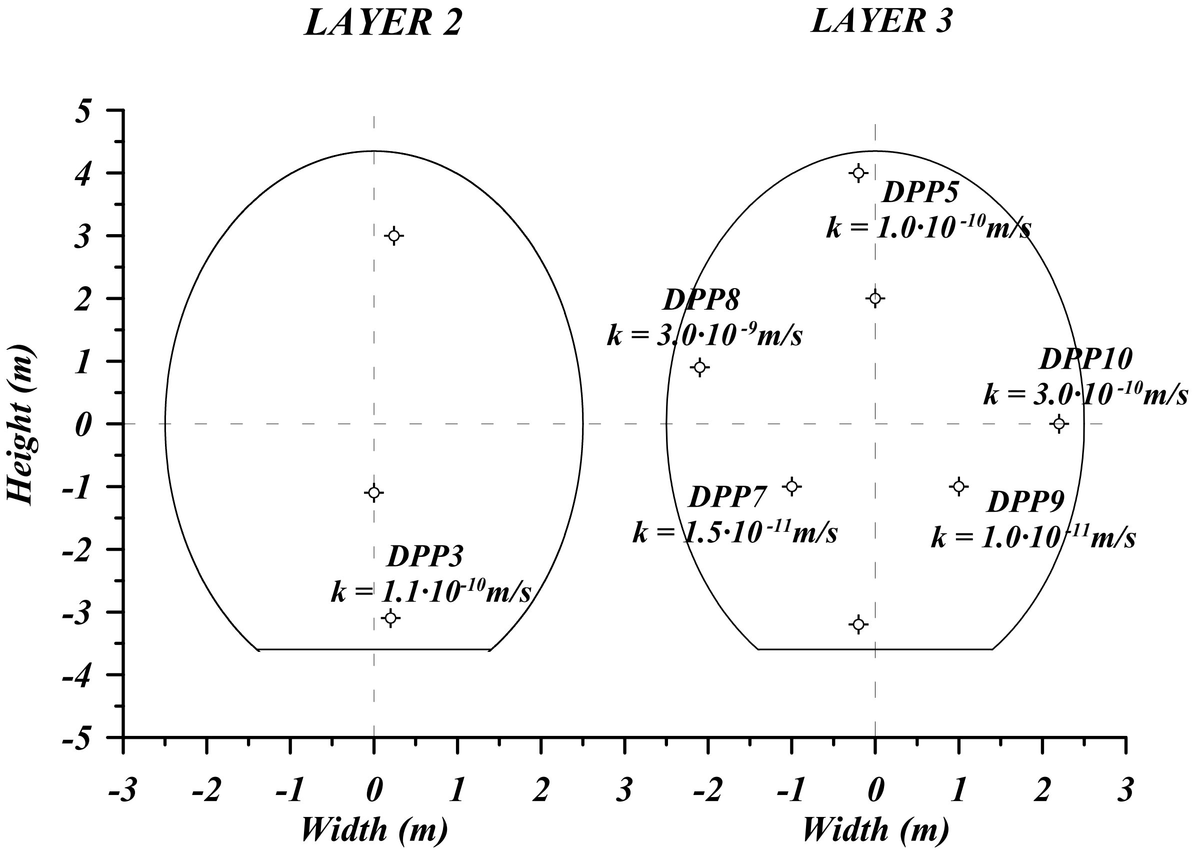

Figure 4.79: Map of backfill local permeability after the analysis of the in situ pulse tests by using the finite element code.

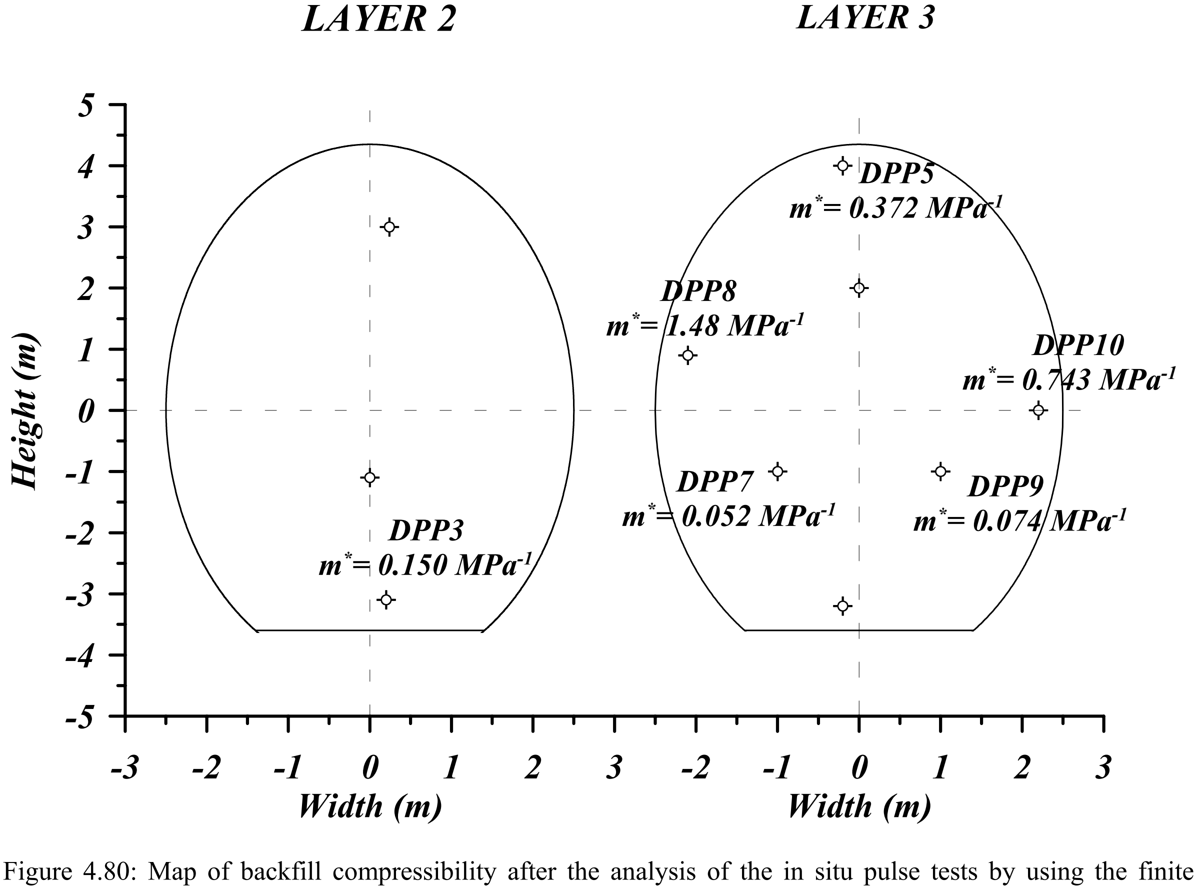

Figure 4.80: Map of backfill compressibility after the analysis of the in situ pulse tests by using the finite element code.